



DIPLOMARBEIT

Analysis of the Cluster Functions in the Human Cochlea

Ausgeführt am Institut für
Analysis und Scientific Computing
der Technischen Universität Wien

unter der Anleitung von
Ao.Univ.Prof. Dipl.-Ing. DDDr. Frank Rattay

durch
Cornelia Wenger
Wallensteinstraße 40/40
1200 Wien

Wien, im September 2008

Acknowledgments

First of all I want to thank my advisor Prof. Rattay, who helped and motivated me very much during the whole working process of my thesis. I really appreciate his patience and kindness in guiding me through one of my first experimental simulation projects which raised the interest and eagerness for scientific projects.

Of course I want to express gratitude to my whole family, especially my father who not only sponsored me and therefore enabled my studies but also comforted me particularly in the last few months. I really feel obliged to my brother as well, who shared a flat with me for the last five years, balanced me in an amazing way with his contrary and completing ideas and interests.

Special thanks go to all my friends who took me out to celebrate or helped me to get some rest whenever I needed to. I am really grateful for every single inspiration I got from all of them. Every single one enthuses me in a different way which as a whole makes a truly great picture. Moreover I really want to thank my longtime friends and study colleagues Sigrun Goluch and Gerhard Kitzler who joined, motivated and encouraged me during our whole studies from the very beginning. Without them it would have been terrible to finish my studies.

Generally I appreciate all the people I've met during my life who assisted me find my way and influenced me to comprehend my interests.

Cornelia Wenger

Abstract

Although the somatic region of afferent human cochlear neurons is quite unique, our contemporary knowledge on the neural coding principles in mammalian cochlear neurons is primarily based on animal experiments. Firstly many of the cochlear neurons are gathered to clusters with 2-4 (Tylstedt et al. 1997) neurons having a common insulation by myelin. Secondly 94% of human spiral ganglion cells are mostly surrounded by only one to several layers of satellite cells (Ota and Kimura 1980), whereas in cats 95% of spiral ganglion cells are firmly myelinated (Spoendlin 1971), which represents almost a reverse proportion between man and cat.

Both human particularities are expected to affect essentially the neural pattern resulting in a specific human physiologic hearing performance. For example, Tylstedt and Rask-Andersen (2001) speculate whether unique formations between human spiral ganglion cells, which have not been observed in other species, may constitute interactive electrotonic or ephaptic transmission pathways.

Two mathematical models are presented to account for the morphological differences which are of major relevance for the propagation of an action potential. The first model was used to simulate the nonmyelinated soma region of human cochlear neurons. The results revealed a strong effect on the excitation pattern of the neuron after small changes in certain sensitive geometrical and electrical parameters. Furthermore an extended mathematical model including the human neuron cluster was developed. With this initial approach, the performed computer simulations for the theoretical case of a single neuron in addition to multiple neuron clusters demonstrated the influence of the cluster on the spiking behavior of the enclosed cochlear neurons.

Zusammenfassung

Obwohl die Somaregion der menschlichen afferenten Cochlear Neuronen einzigartig ist, basiert unser gegenwärtiges Wissen über das neuronale Codierungsprinzip in Säugetier-Nervenzellen der Cochlea auf tierexperimentelle Untersuchungen. Erstens sammeln sich viele der Cochlear Neuronen zu Clusters, wobei 2-4 (Tylstedt et al. 1997) Neuronen von einer gemeinsamen Myelinschicht isoliert sind. Zweitens sind 94% der menschlichen Zellkörper der Neuronen des Ganglion spirale nur von einer oder wenigen Schichten von Satellitenzellen umgeben (Ota and Kimura 1980), obwohl 95% dieser Zellkörper der Katze fest myelinisiert sind.

Man vermutet, dass beide menschlichen Besonderheiten für die physiologisch spezifische Hörleistung verantwortlich sind, da diese das neuronale Muster wesentlich beeinflussen. Tylstedt and Rask-Andersen (2001) spekulierten zum Beispiel, dass einzigartige Anordnungen zwischen menschlichen Ganglienzellen des Ganglion spirale, die nicht bei anderen Spezies gefunden wurden, interaktive elektronische und ephaptische Erregungsleitungen fördern.

Auf Grund des relevanten Einflusses der morphologischen Unterschiede auf die Fortpflanzung eines Aktionspotentials, werden zwei mathematische Modelle präsentiert. Das erste Modell dient zur Simulation der nichtmyelinisierten Somaregion der menschlichen Cochlear Neuronen. Die Resultate zeigten, dass geringe Änderungen von bestimmten sensitiven elektrischen und geometrischen Parametern einen starken Effekt auf die Erregung der Neuronen bewirken. Darüber hinaus wurde ein erweitertes mathematisches Modell für das menschliche Neuronencluster entwickelt. Dieser erste Ansatz für die Computersimulation des theoretischer Fall eines einzigen Clusterumhüllten Neurons und die eines multiplen Neuronenclusters konnte den Einfluss des Clusters auf das Feuerungsprinzip der eingeschlossenen Neuronen nachweisen.

Contents

Acknowledgments	i
Abstract	ii
Zusammenfassung	iii
Contents	iv
List of Tables	vi
List of Figures	vii
List of Abbreviations	ix
1 Introduction	1
2 Nervous System	4
2.1 Anatomy of Human Neurons	4
2.1.1 Cell Membrane	5
2.1.2 Soma	5
2.1.3 Dendrites	6
2.1.4 Axon	6
2.1.5 Synapse	7
2.2 Types of Neurons	8
2.2.1 Structural Classification	8
2.2.2 Functional Classification	9
2.2.3 Nervous System	9
2.3 Passive Electrical Behavior	10
2.3.1 Structure of the Biological Membrane	10
2.3.2 Passive State - Equilibrium	11
2.3.3 Nernst and Goldman Equation	12
2.4 Active Electrical Behavior	14
2.4.1 Action Potential	14
2.4.2 HH - Model	16
3 The Human Ear	23
3.1 Anatomy	23
3.1.1 Cochlea, Organ of Corti	24
3.1.2 Inner Hair Cell	25
3.1.3 Outer Hair Cell	27

CONTENTS

3.2	Afferent Cochlear Neurons	28
3.2.1	Anatomy and Classification	28
3.2.2	Human Specialties	30
3.2.3	Detailed Structure	32
4	Computer Simulation	34
4.1	Compartment Model	34
4.2	Nonmyelinated Soma - Sensitive Parameters	39
4.2.1	RHOI	39
4.2.2	nmsoma	40
4.2.3	lsoma_p	41
4.2.4	d(1)	42
4.2.5	li(6)	43
4.3	Cluster - First Results and Consequences	44
4.3.1	Mathematical Model	44
4.3.2	Single Neuron Cluster	47
4.4	Multiple Neuron Cluster - New Approach	58
4.4.1	2 Neuron Cluster	58
4.4.2	3 Neuron Cluster	61
4.4.3	4 Neuron Cluster	64
5	Conclusion and Further Work	71
A	ACSL Code	75
A.1	Soma Code	75
A.2	Cluster Code	79
	Bibliography	87

List of Tables

2.1	Ion concentration of ICS and ECS.	12
2.2	HH model with temperature constant	21
4.1	Geometrical model parameters of the human cochlear neuron.	38
4.2	Electrical model parameters of the human cochlear neuron.	38
4.3	Standard case of the sensitive parameters of the human cochlear neuron.	39
4.4	Electrical parameters of the cluster.	44
4.5	Diameters of the neuron and its surrounding cluster with varying size.	49
4.6	Maximum values of the membrane potential at the soma.	56
4.7	Maximum values of the membrane potential of the cluster.	58
4.8	Geometry of the human cluster for two cochlear neurons.	59
4.9	Geometry of the human cluster for three cochlear neurons.	62
4.10	Geometry of the human cluster for four cochlear neurons.	65
4.11	Maximum values of the membrane potential at the soma for different stimuli strengths.	67

List of Figures

2.1	Structure of a nerve cell	5
2.2	Types of conduction in the axons of nerve cells	6
2.3	The chemical synapse	7
2.4	Types of neurons concerning the structural differences	8
2.5	The cell membrane	11
2.6	Action potential and subthreshold response	15
2.7	Voltage Clamp Method and transmembrane currents	17
2.8	Sodium and potassium conductances obtained by the voltage clamp experiment	18
2.9	Summary of the HH model	21
3.1	The human ear	23
3.2	The human cochlea and OC	24
3.3	Tip links of hair cells	25
3.4	IHC and OHC	26
3.5	Afferent Innervation of IHC and OHC	27
3.6	Type I and Type II cochlear neurons	29
3.7	Cluster of cochlear neurons	31
3.8	Detailed Structure of cochlear neurons	32
4.1	The equivalent circuit model	35
4.2	Variation of RHOI	40
4.3	Variation of nmsoma	41
4.4	Variation of LSOMA_P	41
4.5	Variation of D(1)	42
4.6	Variation of LI(6)	43
4.7	The equivalent circuit model for the cluster	45
4.8	Geometry of the Cluster	48
4.9	Membrane Potential for $nm^{Cl}=1$ and $nm_{soma}=1$	50
4.10	Membrane Potential for $nm^{Cl}=1$ and $nm_{soma}=2$	51
4.11	Membrane Potential for $nm^{Cl}=1$ and $nm_{soma}=3$	52
4.12	Membrane Potential for $nm^{Cl}=2$ and $nm_{soma}=1$	53
4.13	Membrane Potential for $nm^{Cl}=3$ and $nm_{soma}=1$	54

LIST OF FIGURES

4.14	Membrane Potential for $nm^{Cl}=2$ and $nm_{soma}=2$	55
4.15	Membrane potential of the single neuron cluster	57
4.16	Geometry and spatial arrangement of the two neuron cluster.	59
4.17	Membrane potentials of the two neuron cluster with varying stimuli onsets and strengths.	60
4.18	Membrane potentials under subthreshold condition for a single and a two neuron cluster.	62
4.19	Membrane potentials of the three neuron cluster with varying stimuli onsets and strengths.	63
4.20	Membrane potentials under subthreshold condition for a single, a two and three neuron cluster.	64
4.21	Membrane potentials of the three neuron cluster with varying stimuli onsets and strengths (2).	65
4.22	Geometry and spatial arrangement of the four neuron cluster.	66
4.23	Membrane potentials of the four neuron cluster with varying stimuli onsets and strengths.	68
4.24	Membrane potentials under subthreshold condition for a two, three and four neuron clusters.	68
4.25	Membrane potentials of the four neuron cluster with varying stimuli onsets and strengths (2).	69

List of Abbreviations and Symbols

$\alpha_m, \alpha_n, \alpha_h$ transfer rates from closed to open state [1/ms]

$\beta_m, \beta_n, \beta_h$ transfer rates open form to closed state [1/ms]

ρ_e extracellular resistivity [$k\Omega cm$]

ρ_i intracellular resistivity [$k\Omega cm$]

$[Cl]_e$ extracellular concentration of chloride ions [mol/l]

$[Cl]_i$ intracellular concentration of chloride ions [mol/l]

$[K]_e$ extracellular concentration of potassium ions [mol/l]

$[K]_i$ intracellular concentration of potassium ions [mol/l]

$[Na]_e$ extracellular concentration of sodium ions [mol/l]

$[Na]_i$ intracellular concentration of sodium ions [mol/l]

A surface

ACSL Advanced Continuous Simulation Language

AP Action Potential

BM basilar membrane

C_m membrane capacitance [$\mu F/cm^2$]

Ca^{2+} calcium ion

Cl^- chloride ion

CNS central nervous system

CRRSS Chiu, Ritchie, Rogert, Stagg and Sweeney

d diameter

LIST OF ABBREVIATIONS AND SYMBOLS

ECS	extracellular space
F	Faraday Constant, $F = 9.64845 \cdot 10^4$ [C/mol]
FH	Frankenhaeuser and Huxley
$G_{Cluster}$	cluster conductance of one layer of myelin [mS/cm^2]
G_{intern}	internode conductance of one layer of myelin [mS/cm^2]
$G_{K,max}$	maximum value of potassium conductance [mS/cm^2]
G_K	potassium conductance [mS/cm^2]
G_L	leakage conductance [mS/cm^2]
$G_{Na,max}$	maximum value of sodium conductance [mS/cm^2]
G_{Na}	sodium conductance [mS/cm^2]
GAUSS	Gaussian noise current term
HH	Alan Lloyd Hodgkin and Andrew Huxley
$I_{capacitive}$	capacitive current [$\mu A/cm^2$]
I_{inj}	stimulation current, injected current [$\mu A/cm^2$]
I_{ion}	ionic current [$\mu A/cm^2$]
I_K	potassium current [$\mu A/cm^2$]
I_L	current of other ions, leakage current [$\mu A/cm^2$]
I_m	membrane current [$\mu A/cm^2$]
I_{Na}	sodium current [$\mu A/cm^2$]
I_{noise}	current fluctuation [$\mu A/cm^2$]
I_{ohm}	ohmic current [$\mu A/cm^2$]
ICS	intracellular space
IHC	inner hair cells
k	temperature coefficient, acceleration factor
K^+	potassium ion
k_{noise}	noise factor [$\mu AmS^{-1/2}$]

LIST OF ABBREVIATIONS AND SYMBOLS

l	length
li	length of internodes
m, n, h	gating variables, probability for a membrane gating process
Na ⁺	sodium ion
nm	number of myelin layers
OC	Organ of Corti
OHC	outer hair cells
P_{Cl}	permeability of chloride ions [cm/s]
P_K	permeability of potassium ions [cm/s]
P_{Na}	permeability of sodium ions [cm/s]
PNS	peripheral nervous system
Q	charge
R	Gas Constant, R=8.31441 [J/mol.K]
R_K	resistance of membrane for potassium
R_L	resistance of membrane for other ions
R_{Na}	resistance of membrane for sodium
SEM	Scanning Electron Microscope
SM	scala media
ST	scala tympani
SV	scala vestibuli
T	absolute Temperature
TC	Tunnel of Corti
TEM	Transmission Electron Microscope
TM	tectoral membrane
TMa	tympanic membrane
V^{Cl}	membrane potential of the cluster [mV]

LIST OF ABBREVIATIONS AND SYMBOLS

V_e	extracellular potential [mV]
V_i	intracellular potential [mV]
V_K	Nernst potential of potassium [mV]
V_L	Nernst potential of other ions, leakage voltage [mV]
V_m	transmembrane potential [mV]
V_{Na}	Nernst potential of sodium [mV]
V_{rest}	resting membrane potential [mV]

Chapter 1

Introduction

Our knowledge on the neural coding principles in mammalian cochlear neurons is primarily based on animal experiments. Single fiber recordings enlightened our understanding how an acoustical signal is represented in the spiking pattern of the auditory nerve (Kiang 1966, Brugge et al. 1969, Sachs and Abbas 1974, Shamma 1985, Javel 1994, Rattay and Lutter 1997). As the main elements of mammalian cochleae are quite similar and because of the restrictions for gathering human data, it is generally assumed that the same firing behavior can be expected in man. However in the somatic region afferent human cochlear neurons are quite unique. Firstly most cell bodies of type I neurons are unmyelinated and secondly many of them are gathered to clusters with 2-4 (Tylstedt et al. 1997) neurons having a common insulation by myelin.

The cell bodies differ not only in size, i.e., 25-30 μm in man (Spoendlin and Schrott 1989) and about 20 μm in cat (Liberman and Oliver 1984), but also in the number of myelin layers surrounding them. According to Ota and Kimura (1980) 94% of human spiral ganglion cells are unmyelinated and mostly surrounded by one to several layers of satellite cells. The pre- and postsomatic areas, the lengths of which vary a lot, are not shielded by myelin, either. On the other hand, in all mammals studied so far 90-95% of the spiral ganglion cells are large in size and myelinated. In cats 95% of spiral ganglion cells are firmly myelinated (Spoendlin 1971). It is almost a reverse proportion between man and cat. This morphological difference is of major relevance for the propagation of an action potential.

Both human particularities are expected to affect essentially the neural pattern resulting in a specific human physiologic hearing performance. Analyzing the electrical features of a non- or poorly myelinated somatic region one can conclude that the human afferent cochlear neuron is essentially lesser robust in spike conduction as in the preferred experimental animals cat and guinea pig (Rattay et al. 2001a). This is mainly a consequence of the large capacitance of the soma which consumes most of the current provided by the active peripheral axon and so it is questionable if enough intracellular current is available to prepare excitation in the central axon in order to

conduct the spike. The danger of losing most of the spikes could be reduced by the myelin sheets of the clusters or by a proper combination of geometric and electrical parameters in the presomatic region. Loading the somatic capacitance causes a larger delay: Comparing the reactions of a human and cat cochlear neuron, it has been found that peripherally and centrally evoked spikes arrive with a time difference of about 400 μs in man and 200 μs in cat (Rattay et al. 2001a), a result that was supported by neural response telemetry recording with cochlear implants (Dillier et al. 2002, Cohen et al. 2004).

Is the loss of myelin in the somatic region a human imperfection caused perhaps by a genetic defect? A larger delay and a reduction in sensory information seem to result in disadvantages only. What about monkeys and primates? (Kimura et al. 1987) found in macaque monkeys four types of cochlear neurons, one with unmyelinated perikaryon and myelinated axons. (Tylstedt and Rask-Andersen 2001) speculate whether unique formations between human spiral ganglion cells, which have not been observed in other species, may constitute interactive electrotonic or ephaptic transmission pathways. These may be in the low-frequency region and may increase plasticity and signal acuity related to the coding of speech. Clusters could also work as filters in order to suppress spontaneous spikes without signal information. For example, Rattay et al. (1998) and Svrcek-Seiler et al. (1998) have shown that, e.g., Brownian motion of inner hair cell stereocilia enhances weak auditory signals resulting in spontaneous spikes with and without signal information.

The goal of the thesis is a better understanding of the functions related with the exceptional human cochlear nerve anatomy. This is also of importance for developing better hearing aids, especially for the development of the next generation of cochlear implants. The theory of human hearing should not be based exclusively on cat's single fiber recordings, because experiments with cochlear implants in cats have shown that cathodic current flows are more effective than anodic ones in eliciting neural responses, and this finding has motivated the development of novel speech-processing algorithms. In a recent study (Macherey et al. 2008), it was shown electrophysiologically and psychophysically that the human auditory system exhibits the opposite pattern, being more sensitive to anodic stimulation. These findings are explained by the computational model of the human auditory nerve (Rattay 1999, Rattay et al. 2001a, Rattay et al. 2001b). As nerve fiber model analysis and computer simulations can be valuable tools to enlighten the functional relevance of morphometric data, this thesis provides simulations concerning the nonmyelinated soma and gives a first approach to derive a mathematical model of the neuron clusters to study their influence on the spiking behavior of the surrounded neurons.

The anatomy of the human neurons including their electrical behavior are provided in Section 2. Furthermore an introduction to the mathematical model of Hodgkin

and Huxley (Hodgkin and Huxley 1952) is also included which is used in this thesis to describe the ion flow during the excitation process(Section 2.4.2).

In Section 3 a short overview of the anatomy of the human ear is presented with special interest on the cochlear neurons which show two outstanding specialties as mentioned above. The detailed structure of those neurons which is used for modeling the electrical active behavior is as well provided (Section 3.2.3).

The performed computer simulations are presented in Section 4 including experiments concerning the sensitive parameters of the soma region (Section 4.2) as well as simulations of the human neuron clusters (Sections 4.3 and 4.4). The derivation of the underlying mathematical models are also found in this Section.

A summary and conclusion of the computer simulations including the limitations of the mathematical models and ideas for further experiments are provided in Section 5.

The computer simulations have been performed with the Advanced Continuous Simulation Language. Two example codes are printed in the appendix A to give an idea of the implementation of the mathematical model. One was used to calculate the excitation behavior of cochlear neurons without a surrounding cluster to study the sensitive parameters whereas the other code was used for simulations of a three neuron cluster.

Chapter 2

Nervous System

For the subsequent simulations of human cochlear neurons a brief overview of the nervous system especially its anatomy and function as well as the underlying mathematical models should be presented.

Nerve cells, also called neurons, are cells in the nervous system which enable the processing and transmission of information. Neurons consist of the same principal elements as all the other cells in the human body, but together with muscle cells they are the only electrically excitable cells. They also show specialties concerning the cell form, cell membrane and usually the lack of segmentation.

This section provides a short overview of the anatomy and different types of neurons in Section 2.1 and points out the passive and active electrical properties of the biological membrane in Section 2.3 and 2.4. The differences among neurons concerning structural and functional specialties are presented in Section 2.2 and a brief overview of the organization of the nervous system is outlined in Section 2.2.3. The mathematical background required for the simulation of cochlear neurons in this thesis is also presented.

2.1 Anatomy of Human Neurons

Nerve cells are surrounded by the cell membrane (Section 2.1.1) and they consist of the cell body (Section 2.1.2), also called the soma or perikaryon, the axon (Section 2.1.4) and the dendritic tree (Section 2.1.3) as can be seen in Fig. 2.1. Neurons communicate with other neurons via certain junctions called synapses, which are presented in Section 2.1.5.

A neuron receives information represented by an electrical neuronal impulse mostly at the dendrites and also at the soma. One nerve cell is connected via synapses with up to 7000 other neurons. The nerve impulse of the neuron is only transmitted by one distinct output region, the axon, to other target neurons.

2.1.1 Cell Membrane

The biological membrane surrounds all cells and is often referred to as the unit membrane, because its structure is the same for every enclosed complex. The neuronal cell membrane disunites the intracellular and the extracellular space. It signifies a semipermeable bilayer of phospholipids.

The electrical properties of the membrane enable the generation and transmission of information coded in a nerve impulse, which is also called action potential.

For detailed information about the structure and electrical properties of the cell membrane see Section 2.3.1.

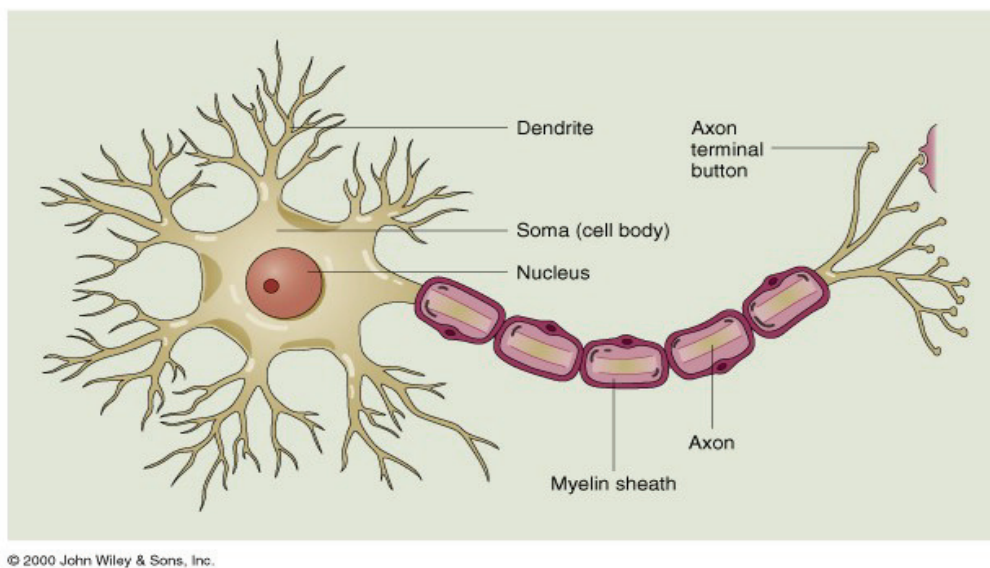


Figure 2.1: The human neuron consists of the soma, the dendrites and the axon with its myelin layer and the interrupting nodes of Ranvier. [Seed Media Group (2008)]

2.1.2 Soma

The soma, also called cell body or perikaryon, is the main part of every cell. It is filled with cytoplasm and contains many organelles which ensure the cellular metabolism, like the nucleus (Fig. 2.1), where the genetic information is stored in form of chromosomes. Inside the nucleus a sub-organelle, the nucleolus, is situated where the ribosomes are produced. These organelles enable the translation of genetic information into proteins.

Another form of membrane enclosed organelles are the vesicles which store or transport cellular substances. The vesicles are often found interconnecting with the endoplasmic reticulum which is a system of tubes important for protein translation

and production and storage of other molecules. We distinguish rough endoplasmic reticulum which has ribosomes and smooth endoplasmic reticulum without ribosomes.

The Golgi apparatus is needed for packaging peptides and proteins into vesicles and for secretion. The energy needed for all these activities, provided by ATP, is produced in the mitochondria.

2.1.3 Dendrites

Dendrites are cellular processes of the soma, often with many branches and a rough surface. They are the most significant input region of every neuron. Dendrites receive nerve impulses from other cells through synaptic connections and transport it to the soma, thus a backflow of information is prevented. The dendritic tree may have up to 200.000 branches.

2.1.4 Axon

The axon is a long, distinct projection away from the soma, starting with the axon hillock to its terminal region, where it branches to its synaptic ends and connects with target neurons. The axon transports nerve impulses away from the soma and represents the only output region.

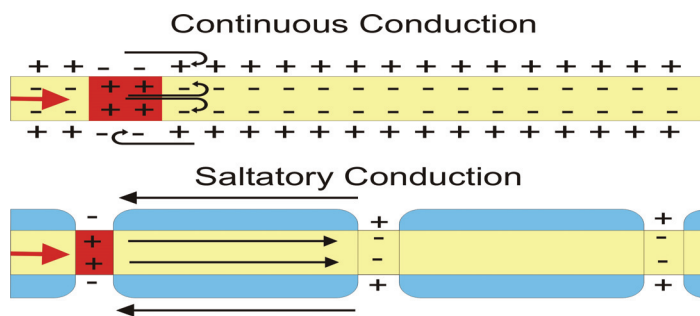


Figure 2.2: Two types of conduction exist in the nerve cells. On the top the continuous conduction of nonmyelinated neurons is presented, the fast saltatory conduction is shown at the bottom where the nerve impulse jumps from one node of Ranvier to the next which is present for myelinated (drawn in blue) axons.

The axon has a length from a few μm to $1m$ and a varying diameter from 0.5 to $20 \mu m$ depending on the presence of several ensheathing satellite cells forming the myelin layer. This layer consists of either one of two types of Glia cells, where Schwann cells supply peripheral neurons and oligodendrocytes ensheathing those of the central nervous system. Therefore axons can be classified into the so called non-myelinated axons which are only supported by one single layer of satellite cells

and the larger myelinated axons which may have up to 300 sheets of myelin as reported by Ritchie (1995). The axon with its myelin layers is called nerve fiber.

The main difference between myelinated and nonmyelinated axons is their velocity of signal conduction. Nonmyelinated axons which are found in vegetative nervous system show a continuous propagation (Fig. 2.2) with a velocity in the range of $v = 1 - 3 \text{ m/sec}$ depending on the fiber diameter.

Myelinated nerve fibers are found in the peripheral nervous system, their myelin layers are intermitted by so called nodes of Ranvier, where the interaction with the extracellular fluid is possible. These nodes are periodically organized along the axon (every 1-2 mm) and enable the fast saltatory conduction velocity of up to $v = 120 \text{ m/sec}$, i.e., the electrical impulse might jump from one node directly to the next one (Fig. 2.2).

The relation between velocity and diameter is linear within myelinated nerve fibers and quadratic for nonmyelinated nerve fibers. (for detailed information about the velocity see, e.g., [Malmivuo and Plonsey \(1995\)](#)).

Although the myelin sheet is often assumed to be an electrically insulating layer, [Ritchie \(1995\)](#) reported that it has become increasingly clear that myelin itself is not a very good insulator, but its crucial role is to reduce dramatically the capacitive load of internodal axolemma on the nodes of Ranvier which is going to be discussed later on. This new insights play an important role in the excitation process and information conduction in the nervous system.

Bundles of axons make up so called nerves.

2.1.5 Synapse

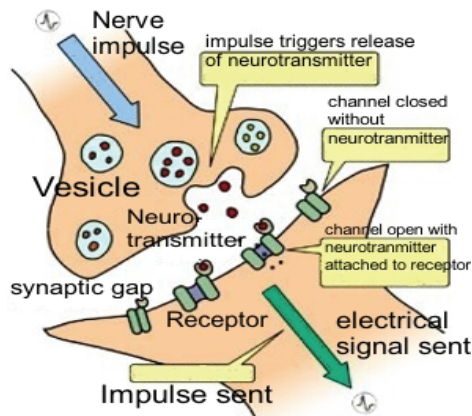


Figure 2.3: The chemical synapse with the pre- and postsynaptic neuron, neurotransmitter containing vesicles and also postsynaptic receptors. [\[Review \(2008\)\]](#)

A variety of synapses are present in the human body with an amount of 10^{15} in a human child decreasing with age. While electrical synapse are faster and more reliable, chemical synapses are more frequent and therefore discussed in this section.

The chemical synapse is the junction between two cells. Nerve impulses are always transmitted in the same direction, that is from the presynaptic to the postsynaptic cell.

The presynaptic area of the synapse is the end of the axon, the synaptic bouton, which contains neurotransmitter enclosed in synaptic vesicles. The postsynaptic region, normally situated at the dendrites or even at the soma of a neuron, consists of a receptor packed area of the target neuron. The synaptic cleft between the pre- and postsynaptic cell is only 20 nm wide.

When a nerve impulse which traveled away from the soma to the axon terminal reaches the synaptic end, calcium ions flow into the cell which enables the neurotransmitter containing vesicles to merge with the postsynaptic membrane and therefore the neurotransmitter are released into the synaptic cleft (Fig. 2.3). This mechanism is called exocytosis. The receptors bind these neurotransmitters what causes ions to flow into the cell through certain ion channels in the membrane and therefore the transmembrane voltage of the postsynaptic cell is changed. The nerve impulse is received at the target neuron and than continues to travel along this neuron.

Generally excitatory synapses, which increase the action of the target neuron and are provided by a depolarization of the postsynaptic cell, are distinguished from the inhibitory synapses which decrease the potential of the target neuron.

2.2 Types of Neurons

As mentioned before there are many types of neurons considering their morphometric features. Neurons can be distinguished concerning their structural and functional differences which are listed in the following sections.

2.2.1 Structural Classification

A first anatomical distinction concerns the geometric polarity of neurons. Fig. 2.4 illustrates those different types which show typical features and have different functions.

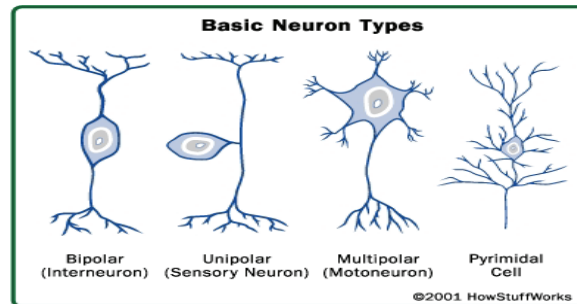


Figure 2.4: Different types of neurons concerning the structural classification. [Freudenrich (2001)]

- unipolar neurons: These neurons have only a single short process considered to be the axon. Unipolar neurons are present in the retina and generally important for sensory perception.
- pseudounipolar neurons: These cells have a dendrite and an axon emerging from the same process and are found in the spinal nerve.

- bipolar neurons: These cells have an axon and a single dendrite symmetric to each side of the soma and are found in the retina and the cochlea and therefore are of special interest for the topic of this thesis.
- multipolar neurons: These neurons, e.g., motorneurons have an axon and more than two dendrites.

2.2.2 Functional Classification

Concerning their function neurons can be divided concerning their differences of either their direction, i.e., the path of the transmission of information, or their action on their target neurons.

Three different types of neurons concern their direction:

- afferent neurons: They are also called sensory nerve cells and transmit information from the periphery including the tissue and organs to the brain.
- efferent neurons: They are also called motorneuronen and transfer signals from the brain and the spinal cord to the periphery.
- interneurons: These form the greatest amount of neurons and connect to other neurons.

Concerning the action two types of neurons can be distinguished:

- excitatory neurons: They excite their target neurons through excitatory neurotransmitters. (Section 2.1.5)
- inhibitory neurons: These neurons are often interneurons which inhibit their target neurons. (Section 2.1.5)

2.2.3 Nervous System

The nervous system, i.e., the total amount of neurons in the human body, can be divided into two major parts, namely the *central nervous system* (CNS) and the *peripheral nervous system* (PNS) .

The CNS consists of the brain (with the majority of nerve cells of about 100 billion neurons and trillions of support cells called glia) and the spinal cord. The CNS is protected by bones, i.e. the skull and the vertebrae. Just to give a brief overview the brain is organized in the forebrain which consists of the Telencephalon, the Diencephalon and the Mesencephalon, the midbrain composed of the Metencephalon and the hindbrain which consists of the Myelencephalon. Most of the neurons in the CNS are unmyelinated and the basic function of the CNS is processing the information which was received by the PNS.

Therefore the PNS connects the brain and the spinal cord to the rest of the body via cranial and spinal nerves and consists of a few million neurons. Furthermore the PNS can be subdivided into the somatic nervous system and the unconscious autonomic nervous system.

The somatic nervous system consists of the sensory cells which receive external input and transmits it to the CNS and the muscle cells which are effectors, i.e., the information is passed from the brain to the body.

The autonomic nervous system consists of the sympathetic nervous system, the parasympathetic nervous system and the enteric nervous system which controls smooth muscles of the internal organs and glands. The main difference to the somatic nervous system is that these neurons connect directly to their targets whereas only one secondary motor neuron is reached by a neuron of the autonomic nervous system which then transmits the information to the organs.

2.3 Passive Electrical Behavior

As mentioned before the biological membrane is responsible for the signal processing in human nerve cells, i.e., the electrical excitability. Due to its certain structure the membrane has passive and active electrical properties.

The special structure of the cell membrane is presented in Section 2.3.1. The passive properties which enable the propagation of an equilibrium state of the transmembrane voltage are discussed in Section 2.3.2. The derivation of the Nernst and Goldman equations for this equilibrium potential of the membrane is as well presented in the following (Section 2.3.3). The active properties, responsible for the development and previous transmission of a nerve impulse along the nerve fiber, are discussed in Section 2.4.

2.3.1 Structure of the Biological Membrane

The membrane is a semipermeable bilayer of different phospholipids, mainly phosphatidylcholine, phosphatidylethanolamine, phosphatidylinositol, phosphatidylserine. These phospholipids are molecules composed of a hydrophobic lipid tail and a hydrophilic phosphate head. Due to the aqueous fluids inside and outside the cell the phospholipids arrange spontaneously to the stable floating equilibrium of a bilayer, i.e., the lipid tails face each other and the phosphate heads confront the intra- and extracellular space (Fig. 2.5).

The membrane also contains different proteins which differ in their location (Fig. 2.5). There are proteins attached to the membrane inside and outside the cell, proteins which are embedded in one lipid layer and the channel proteins which pass the whole membrane connecting the *intracellular space* (ICS) and the *extracellular space* (ECS). Some types of ions are able to pass these channels if they are open.

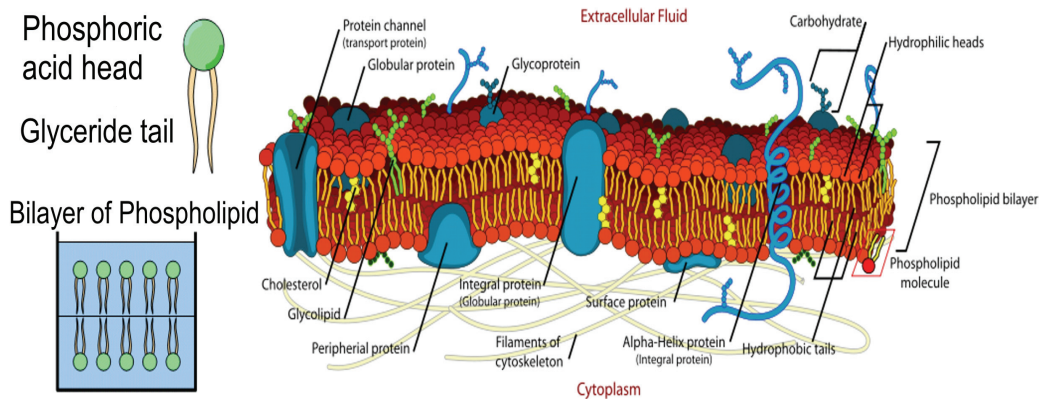


Figure 2.5: One phospholipid and the arrangement of some in aqueous solution to a bilayer at the left. [Malmivuo and Plonsey (1995)] Schematic picture of the cell membrane with an included transmembrane protein at the right. [Hill (2008)]

These membrane channels are specific for certain ions, i.e., only one type of ion is able to pass one specific channel. They have distinct distribution along the neuron and also differ in their permeabilities. In the resting state the membrane is mostly permeable to (K^+) and (Cl^-) and nearly not permeable to (Na^+) and (Ca^{2+}). The opening process of these channels are of complex chemical nature, however ions are only able to diffuse through the channel from the ICS to the ECS or in the other direction if the voltage-dependent activation and inactivation gates are open. 10^6 ions per second are able to pass through one open channel.

A single lipid molecule has a length of 3 nm and consequently the membrane is about 7 nm thick. By taking the attached proteins into account some authors report a membrane thickness of $8\text{-}10\text{ nm}$.

2.3.2 Passive State - Equilibrium

The ICS and ECS contain many types of dissolved ions with different concentrations on each side. Among others the most important ions concerning the electrical properties are sodium (Na^+) which is numerous especially in the ECS, potassium (K^+) with a greater amount in the ICS, chloride (Cl^-) predominant in the ECS and large anions (A^-) only present in the ICS. Table 2.1 provides an overview of the typical ion concentrations in different types of cells.

These ions move freely in the aqueous fluids and are able to cross the membrane from the ICS to the ECS or in the other direction with exception of the immobile, impermeable (A^-) which are important for the electro neutrality. Due to the movement the electrically charged ions tend to concentrate on the inner and outer surface of the membrane resulting in an electrical field. It is predicted that the ions are endeavored to reach an equilibrium by influx of (Na^+) and efflux of (K^+). Thus the electrical

2.3 Passive Electrical Behavior

	extracellular concentration			intracellular concentration			ratio of concentration	direction of diffusion
	M	N	S	M	N	S	for N	
$[Na^+]$	120	150	460	9	15	50	10:1	\Rightarrow
$[K^+]$	2.5	5.5	10	140	150	400	1:27	\Leftarrow
$[Cl^-]$	120	125	540	4	9	50	14:1	\Rightarrow

Table 2.1: Ion concentration of ICS and ECS in M(muscle), N(motoneuron) and S (squid axon). The ratio is given for N, the influx is symbolized by an arrow pointing to the right and the efflux arrow points to the left (values in mMol/l).[Pfützner (2003)]

forces effecting the ions must equal the osmotic forces which also affect them (Section 2.3.3).

This steady state where no signal is applied, i.e., no action potential is present is not truly a passive state, but more of a stable active state. Because of the selective membrane channels and the existing concentration gradients of the ions an equilibrium potential may develop.

In the resting state the concentration gradient of (K^+) is of special interest, because of the permeable channels. Due to the sparsely permeable channels of (Na^+) and (Ca^{2+}) and the high concentration gradients across the membrane, (Na^+) leakage influx needs to be also considered while deriving the equilibrium.

In order to prevent these leakage flux and to maintain the equilibrium potential an enzyme, the sodium-potassium pump (Na^+/K^+ -ATPase), is located in the membrane. This pump corresponds to an active transport which consumes energy in form of ATP. For each ATP molecule three (Na^+) ions are transported back to the ECS and two (K^+) ions to the ICS.

2.3.3 Nernst and Goldman Equation

A first approach to derive the equilibrium potential is the Nernst Equation which describes the voltage across the membrane for one ion caused by its different concentrations in the ICS and ECS. Therefore the electric work to cause the transmission of n mol ($1 \text{ mol} = 6.0225 \cdot 10^{23}$) of an ion from concentration c_1 to c_2 must equal the osmotic work to compress those ions from volume V_1 to V_2 .

According to the laws of gas dynamics the osmotic energy dW to compress a volume dV is given by $dW = p \cdot dV$ with the pressure p leading to the total work of

$$W_{osmotic} = - \int_{V_1}^{V_2} p dV. \quad (2.1)$$

Introducing the gas constant $R = 8.31441 \text{ J/mol.K}$ and the absolute Temperature T

2.3 Passive Electrical Behavior

and considering $pV = nRT$, the total work is given as

$$W_{osmotic} = - \int_{V_1}^{V_2} \frac{nRT}{V} dV = -nRT \ln \frac{V_2}{V_1}. \quad (2.2)$$

With the relations $c_1 = \frac{n}{V_1}$, $c_2 = \frac{n}{V_2}$, the osmotic work results in

$$W_{osmotic} = n \cdot R \cdot T \ln \frac{c_2}{c_1}. \quad (2.3)$$

The electric work to move the charge Q against the voltage V is given as

$$W_{electric} = Q \cdot V. \quad (2.4)$$

With the Faraday constant $F = 9.64845 \cdot 10^4 C/mol$ and the relation $Q = n \cdot z \cdot F$, the electrical work follows as

$$W_{electric} = n \cdot z \cdot F \cdot V. \quad (2.5)$$

Setting $W_{osmotic} = W_{electric}$ leads to the Nernst Equation

$$V_m = \frac{R \cdot T}{z \cdot F} \ln \frac{c_2}{c_1}. \quad (2.6)$$

As mentioned above the ion concentrations $[K^+]$, $[Na^+]$ and $[Cl^-]$ of potassium, sodium and chloride play the most important part concerning electrical properties, thus for the equilibrium potential as well.

Therefore an extension of the Nernst Equation for one ionic type is given by the Goldman Equation for calculating the resting membrane potential, defined as the difference between the intra- and extracellular potential, i.e., $V_m = \phi_i - \phi_e$, which is given as

$$V_m = \frac{R \cdot T}{F} \ln \frac{P_K[K]_e + P_{Na}[Na]_e + P_{Cl}[Cl]_i}{P_K[K]_i + P_{Na}[Na]_i + P_{Cl}[Cl]_e} \quad (2.7)$$

The suffix i stands for intracellular, e corresponds to the extracellular. The ECS concentrations of (Na^+) and (K^+) appear in the numerator, because they both are anions in contrast to the cathodic (Cl^-) .

P_i stands for the permeability of either (Na^+) , (K^+) or (Cl^-) (induced by the suffix i) and is measured in cm/s . By denoting u_i as the mobility for $i = Na, K, Cl$; α as the thickness of the membrane and β as partitions coefficient between the membrane and the aqueous solution the permeability is given as

$$P_i = \frac{u_i \cdot \beta \cdot R \cdot T}{\alpha \cdot F}. \quad (2.8)$$

Using equation 2.7 and the know measured value of $-70 mV$ for the resting potential of the giant squid axon, the ratio of the permeabilities can be derived. With the values

obtained by Table 2.1 of the ion concentrations of the ICS and ECS from the squid axon we can conclude that the membrane potential at the resting state is given as

$$V_m = 58 \log \frac{10 + 0.03 \cdot 460 + 0.1 \cdot 40}{400 + 0.03 \cdot 50 + 0.1 \cdot 540} = -70 \text{ mV}. \quad (2.9)$$

Therefore the ratio of the permeabilities of the squid axon are concluded to be $P_K : P_{Na} : P_{Cl} = 1 : 0.03 : 0.1$ what also represents the main goal of the Goldman equation.

Note that this ratio only corresponds to the resting state. For example, Ritchie (1995) reported a ratio of $P_K : P_{Na} : P_{Cl} = 1 : 0.04 : 0.45$ for a different type of neuron at rest and a quite differing ratio of $P_K : P_{Na} : P_{Cl} = 1 : 20 : 0.45$ at the peak of a nerve impulse.

2.4 Active Electrical Behavior

As noted at the beginning neurons are electrically excitable cells and therefore able to transmit information through the body. All information is coded in an electrical (binary) signal resulting in a change of the membrane potential V_m . The ability of nerve cells to generate and transport these signals, so called *Action Potentials* (APs), results from the active mechanism of the membrane.

The appearance and underlying mechanisms for an AP is discussed in Section 2.4.1. A model for calculating these APs theoretically and analyzing the underlying mechanisms is also provided in Section 2.4.2.

2.4.1 Action Potential

When a neuron receives a signal from another nerve cells, i.e., is stimulated, the transmembrane potential V_m certainly changes from the measured resting value of about -70 mV . If an excitatory stimulus is applied the potential is depolarized, in case of an inhibitory signal the magnitude of the membrane voltage increases, i.e., the cell is hyperpolarized (Fig. 2.6). This change of potential is caused by the opening of voltage-dependent ion channels.

If the stimulus remains below a certain threshold, i.e., it is not strong enough, the membrane is not activated. Under this subthreshold condition the potential will recover with the help of the Na^+/K^+ -ATPase.

The neuron is activated if an excitatory stimulus reaches the threshold of about 20 mV , i.e., a membrane potential of -50 mV . This change of potential, irrespective of the strength of the transthreshold stimulus, leads to a sequence of opening an closing of the different channels resulting in ion flow. Therefore every AP is said to follow the all-or-nothing principle and has a uniform appearance and form.

2.4 Active Electrical Behavior

During the initiation phase the membrane is depolarized and the threshold for the voltage dependent sodium channels is reached.

At a voltage of about -60 mV the first sodium channels open leading to the following rising phase and subsequent overshoot. The resulting (Na^+) influx depolarizes the membrane and therefore more sodium channels are activated because of the rapid increase in sodium permeability. As a consequence an overshoot, i.e., a positive inside potential of about 20 mV is observed.

Before the maximum potential is reached, the sodium channels begin to inactivate spontaneously and the potassium channels slowly increase their permeability. During the repolarization phase the (Na^+) influx stops and the (K^+) ions flow from the ICS to the ECS decreasing the membrane potential.

Often a hyperpolarization is also present resulting from the still increased potassium permeability and pump rate of the Na^+/K^+ -ATPase. After stimulation the membrane potential returns to its resting state as can be observed in Fig. 2.6.

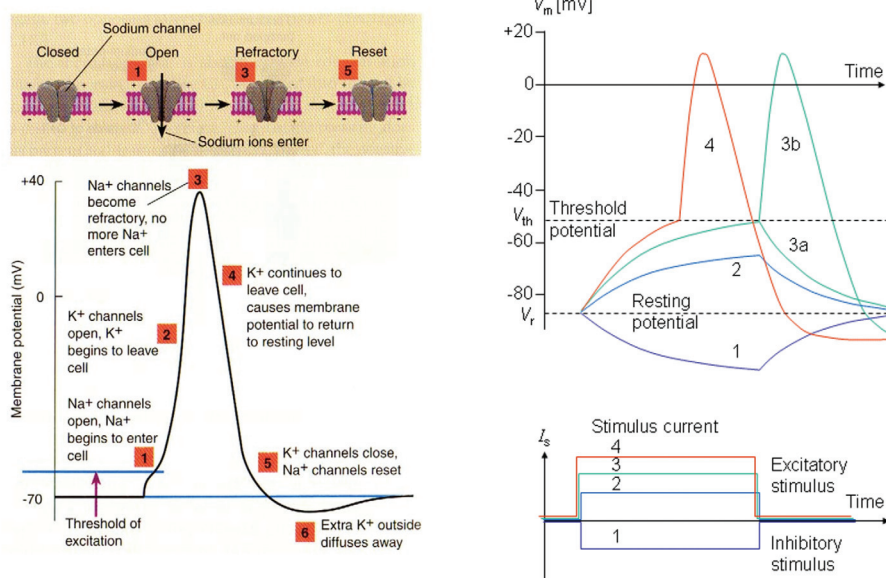


Figure 2.6: At the left the typical form of an AP according to the all-or-nothing principle is shown with the corresponding states of the ion channels on top. [Hummel and Taylor (2007)] At the right the changes in the membrane potentials are shown for an inhibitory stimulation (1), a subthreshold stimuli (2), a transthreshold one (4) and one stimulus which is at the threshold and therefore either leads to an AP (3b) or fails to excite the neuron (3a). [Malmivuo and Plonsey (1995)]

Activation of a neuron is triggered with a strong short stimulus and also follows an adequate longer weaker current, i.e., excitation is strength-duration dependent, which can be illustrated with the strength-duration curve.

The weakest pulse amplitude which would need theoretically infinite duration to initiate activation is called the rheobase. The chronaxy is defined as the minimum pulse duration needed to excite the cell with twice rheobase current.

When repetitive stimuli are applied the neuron shows refractory behavior, characterized by a rise in the excitation threshold (Fig. 2.6). The absolute refractory period is denoted as the time when the neuron is activated and therefore unable to trigger a following impulse caused by inactive, closed sodium channels. When these channels return to active, open state in the onwardly repolarization phase the neuron is able to be activated by a much stronger current with a resulting smaller depolarization and is said to be relatively refractory.

The duration of the whole AP in neurons is about 1 *ms*.

2.4.2 HH - Model

The aims of the mathematical Model of *Alan Lloyd Hodgkin and Andrew Huxley* (HH), developed in 1952, are to describe membrane properties, theoretically calculate APs and thus illustrate their characteristics and to analyze the mechanisms involved in the excitation process of a neuron, especially the present membrane currents including the ion flow.

The work of *Hodgkin and Huxley (1952)* was based on the findings of the voltage clamp experiment to describe the gating processes of voltage-dependent ion channels, which are affected by the nonlinear conducting behavior of the membrane during stimulation. This means that the conductances appear as a function of time and transmembrane voltage. In order to derive appropriate equations, electric current flow needs to be considered in detail with equivalent circuit models of the transmembrane current which consists of a capacitive and ionic component (Fig. 2.7). Additionally the results are combined with curve fitting techniques for describing the probabilities of opening and closing of the decisive ion channels during excitation.

In 1949 the voltage clamp method was developed separately by *Cole (1949)* and *Marmont (1949)* to measure the individual ion flow during the excitation process of a neuron, i.e., when the specific transmembrane resistances are not constant (Fig. 2.7). HH used the method for recording data about sodium and potassium flow in the giant squid axon (with a diameter up to 0.5 *mm*), by inserting a stimulating electrode along the axis of the axon and a recording electrode of the same length outside the axon. During stimulation the voltage is kept constant (i.e., there is a voltage step at $t = t_0$ away from the resting potential $V_{rest} = -65 \text{ mV}$) so that no capacitive effects occur since the potential does not change, i.e., $\frac{dV}{dt} = 0$. The transmembrane current is measured which composes therefore only of the ionic current.

To describe APs properly, HH focused on the two basic currents of (Na^+) and (K^+) and an additional leakage current which represents mainly (Cl^-) and other ions peripherally involved in the excitation process. By either using a voltage clamp step matching the sodium Nernst Potential to eliminate sodium flow or by blocking chan-

2.4 Active Electrical Behavior

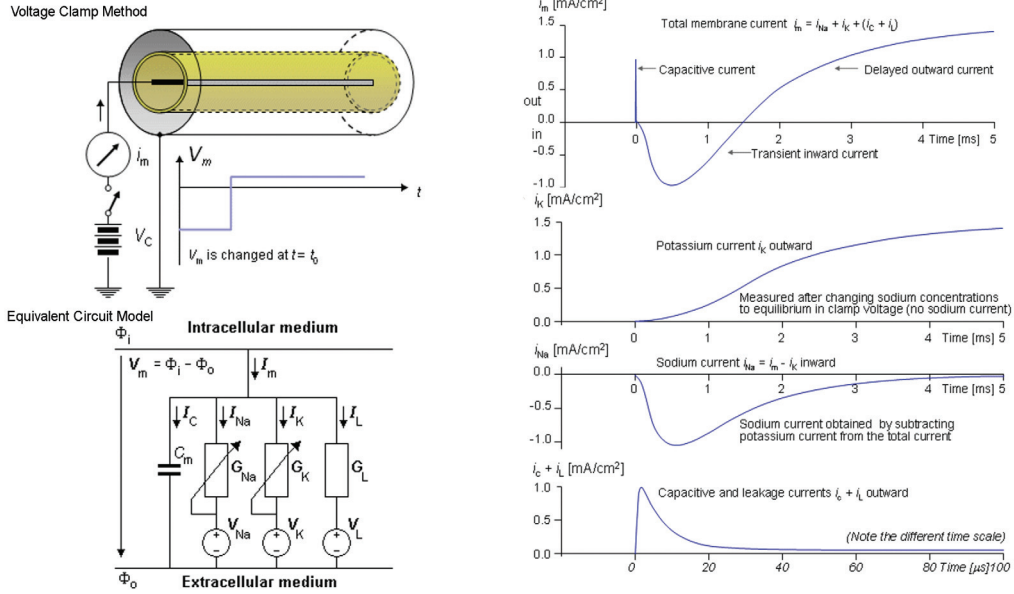


Figure 2.7: At the left top the simplified principle of the voltage clamp experiment is shown, the equivalent circuit model used in the following is presented at the left bottom. At the right the total transmembrane current is drawn at the top and the individual ionic current below. [Malmivuo and Plonsey (1995)]

nels with pharmacological agents, separate results for the ion flow of (Na^+) and (K^+) can be observed as visualized in Fig. 2.7 at the right.

HH modeled the basic electrical components of the membrane as shown in the electrical circuit model of Fig. 2.7. They concluded that the transmembrane current consists of the sodium and potassium current I_{Na} , I_K , a leakage current I_L and a capacitive current. The usual restriction for the transmembrane potential $V_m = \phi_i - \phi_e$ assures the positive flow direction from the inside of the axon to the outside. In the active state the resistances of the membrane per unit area for the ions R_{Na} , R_K , R_L are not constant. Therefore the conductances per unit area for sodium, potassium and other ions, represented as the leakage conductance, are introduced:

$$G_{Na} = \frac{1}{R_{Na}}, G_K = \frac{1}{R_K}, G_L = \frac{1}{R_L} [mS/cm^2]. \quad (2.10)$$

HH determined in their experiments that the conductances for sodium and potassium are functions of time and transmembrane-voltage while the leakage conductance remains constant like in the passive state.

No sodium current is present, if the transmembrane voltage V_m equals the Nernst Potential of sodium V_{Na} , concluding that the driving voltage for the sodium flow is given as $(V_m - V_{Na}) [mV]$. According to Ohm's law the conductances can be written

2.4 Active Electrical Behavior

as

$$G_{Na} = \frac{I_{Na}}{V_m - V_{Na}}, \quad G_K = \frac{I_K}{V_m - V_K}, \quad G_L = \frac{I_L}{V_m - V_L} \quad (2.11)$$

where I_{Na}, I_K, I_L are the previously defined electric currents per unit area [$\mu A/cm^2$]. The total transmembrane current I_m is the sum of the capacitive and the ionic current, i.e., is given as

$$I_m = I_{capacitive} + I_{ionic} = C_m \frac{dV_m}{dt} + I_{Na} + I_K + I_L, \quad (2.12)$$

where C_m denotes the membrane capacitance per unit area [$\mu F/cm^2$] and I_m represents the membrane current per unit area [$\mu A/cm^2$].

Therefore the HH-equation for the transmembrane current is given as

$$I_m = C_m \frac{dV_m}{dt} + G_{Na}(V_m - V_{Na}) + G_K(V_m - V_K) + G_L(V_m - V_L). \quad (2.13)$$

The next step is to find equations for the conductances which relate to the results from the voltage-clamp experiment. The results of the potassium and sodium conductances are presented in Fig. 2.8.

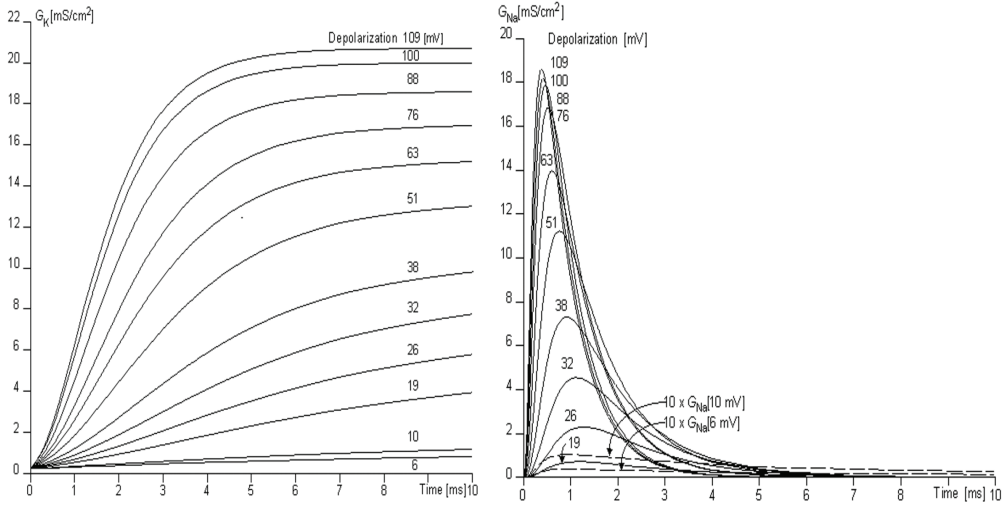


Figure 2.8: At the left the potassium conductances for different voltage steps are shown. The corresponding results for the sodium conductances are presented at the right. [Malmivuo and Plonsey (1995)]

Starting with the potassium conductance, HH introduced a physical basis for their mathematical description. They presented n-gates which are responsible for opening and closing the selective potassium channels, i.e., an n-gate may be in the open state with the probability n and change to the closed state with the probability $(1-n)$,

where $0 \leq n \leq 1$. HH assumed that a channel is open if there exist four open n-gates, so that the probability for an open channel is proportional to n^4 since the gates are assumed to be independent. The changes in the parameter n describes the alteration of the state of the n-gates. These changes from n to $(1-n)$ are explained with voltage-dependent transfer rates, i.e., α_n [1/ms] which states the transfer from $(1-n)$ to n and β_n [1/ms] from n to $(1-n)$. These assumptions lead to a differential equation for the fraction of the gates in the open state n :

$$\frac{dn}{dt} = \alpha_n(1 - n) - \beta_n n. \quad (2.14)$$

By defining $G_{K,max}$ as the maximum value of potassium conductance per unit area [mS/cm^2] and n solves equation 2.14, i.e., is a fraction of open n-gates, the conductance is given as

$$G_K = G_{K,max} n^4. \quad (2.15)$$

The sodium conductance increases ten times faster than the potassium conductance as can be seen in Fig. 2.8. To account for this behavior HH introduced m-gates, comparable to the activation gates of a selective sodium channel, that are open with a probability of m and closed with the probability $(1-m)$. The fraction of gates in the open state m follow the same differential equation like the n-gates,

$$\frac{dm}{dt} = \alpha_m(1 - m) - \beta_m m, \quad (2.16)$$

with the transfer rate α_m , which describes a change from closed to open in [1/ms], and β_m for the opposite direction.

Additionally they supposed h-gates, equivalent to the inactivation gates, where h is the probability for the fraction of h-gates to be in the non-inactivating state, i.e., they are open, and $(1-h)$ the probability to be in the inactivating state. The voltage-dependent transfer rate α_h corresponds to a change from the inactivating to the non-inactivating state, β_h the other way round, so that the differential equation for the fraction of h-gates in the non-inactivating state is given as

$$\frac{dh}{dt} = \alpha_h(1 - h) - \beta_h h. \quad (2.17)$$

HH supposed that a selective sodium channel is open if there are three open m-gates and one non-inactivating h-gate, therefore the probability of an open channel is proportional to $m^3 h$ if m, h obey the equations 2.16 and 2.17. Introducing the maximum value of sodium conductance per unit area $G_{Na,max}$ [mS/cm^2], the conductance follows as

$$G_{Na} = G_{Na,max} m^3 h. \quad (2.18)$$

The leakage conductance is assumed to stay constant as mentioned before

$$G_L = \text{constant}. \quad (2.19)$$

By fitting the experimental data and introducing the reduced membrane voltage $\bar{V} = \phi_i - \phi_e - V_{rest}$ HH assumed that the voltage-dependent transfer rates for the dimension $[1/ms]$ can be calculated as follows:

$$\alpha_n = \frac{0.1 - 0.01\bar{V}}{\exp^{1-0.1\bar{V}} - 1}, \quad \alpha_m = \frac{2.5 - 0.1\bar{V}}{\exp^{2.5-0.1\bar{V}} - 1}, \quad \alpha_h = \frac{0.07}{\exp^{0.07\bar{V}}}, \quad (2.20)$$

$$\beta_n = \frac{0.125}{\exp^{0.0125\bar{V}}}, \quad \beta_m = \frac{4}{\exp^{\bar{V}/18}}, \quad \beta_h = \frac{1}{\exp^{3-0.1\bar{V}} + 1}. \quad (2.21)$$

The following constants complete the model:

$$C_m = 1\mu F/cm^2 \quad (2.22)$$

$$V_{rest} - V_{Na} = -115 mV, \quad G_{Na,max} = 120 ms/cm^2 \quad (2.23)$$

$$V_{rest} - V_K = 12 mV, \quad G_{K,max} = 36 ms/cm^2 \quad (2.24)$$

$$V_{rest} - V_L = -10.613 mV, \quad G_L = 0.3 ms/cm^2. \quad (2.25)$$

To sum up these results and get a better visualization of the alteration of the gating variables during excitation Fig. 2.9 demonstrates the observations of the potassium ions on the left and those of the sodium ions and the leakage current at the right.

The top level, characterized by A, illustrates the change of the transfer rates during the voltage clamp experiment. Additionally the m (yellow), n (blue), and h (red) gates which are responsible for the activation and inactivation of the certain channels and described above are also provided.

The frames in middle, i.e., the B level indicate the voltage step and ongoing depolarized phase of the membrane potential with the simultaneous and corresponding change of the transfer rates.

At the bottom, the C level, the graphs for m, n and h are provided which together represent graphs which are proportional to the conductances of potassium G_K in green and that of sodium G_{Na} in orange.

The HH-equations were based on experiments with a squid axon at a temperature of $T = 6.3^\circ C$, so that an acceleration factor k for the gating variables m, n, h was introduced. To sum up these results, the four nonlinear HH-equations including dependence on temperature and initial conditions for the transmembrane potential V_m and the gating variables m, n, h are presented in a closed form in Table 2.2.

The HH-model was the first to describe the electrical properties of the membrane during excitation process and at rest in a quantitatively correct and desirable way. Due to the absence of propagation of an AP at a temperature higher than $T = 31^\circ C$ without further modification of the HH-model and the developing selection techniques for nerve fibers and technologically advanced electrodes, further models have been created.

To name just a few, in 1964 [Frankenhaeuser and Huxley \(1964\)](#) (FH) developed a model of a myelinated frog axon at a temperature of $T = 20^\circ C$. [Chiu et al. \(1979\)](#)

2.4 Active Electrical Behavior

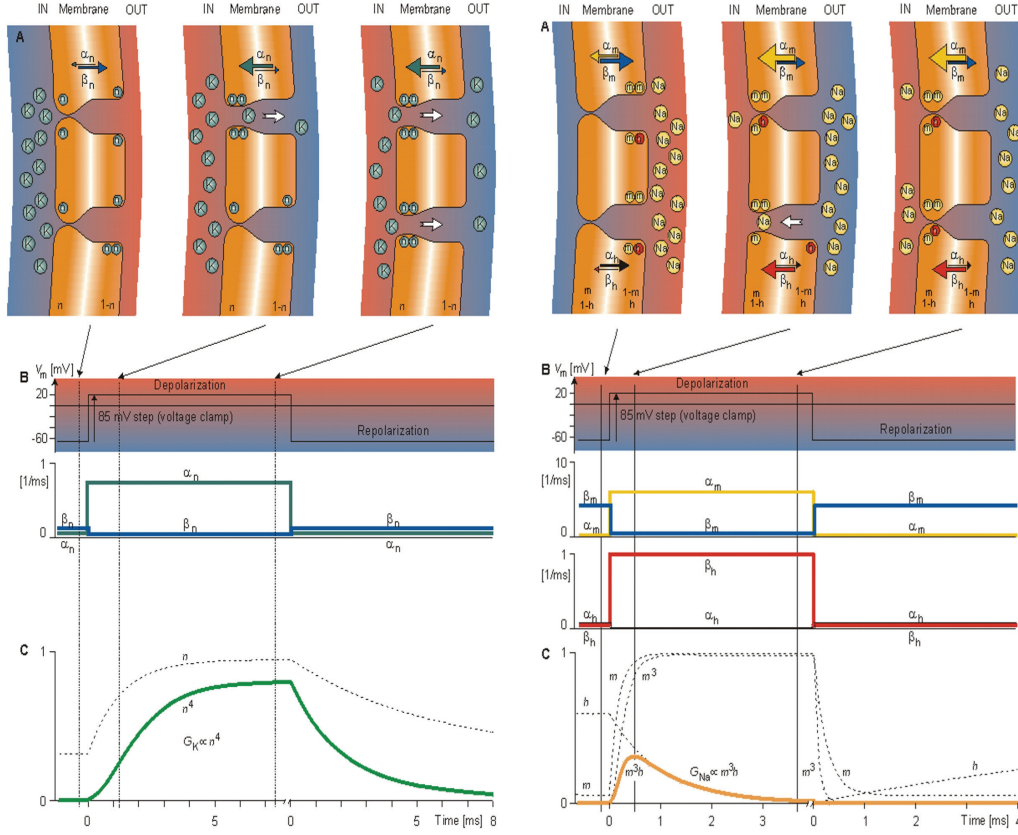


Figure 2.9: Summary of the HH model. Explanation in the text. [Malmivuo and Plonsey (1995)]

TRANSMEMBRANE CURRENT		
$\frac{V_m}{dt} = [I_m - G_{Na,max} m^3 h (V_m - V_{Na}) - G_{K,max} n^4 (V_m - V_K) - G_L (V_m - V_L)] / C_m$		
$V_m(0) = 0$		
TRANSFER RATES		
$\frac{dm}{dt} = [\alpha_m(1 - m) - \beta_m m] k$	$m(0) = 0.05$	$k = 3^{0.1T - 0.63}$
$\frac{dn}{dt} = [\alpha_n(1 - n) - \beta_n n] k$	$n(0) = 0.32$	
$\frac{dh}{dt} = [\alpha_h(1 - h) - \beta_h h] k$	$h(0) = 0.6$	

Table 2.2: Equations of the HH model with temperature constant. I_m denotes the transmembrane current. Used parameters and constants are similar to the above.

modeled a myelinated rabbit nerve at $T = 14^\circ\text{C}$ that was completed by Sweeney et al. (1987) for $T = 37^\circ\text{C}$ to the Chiu, Ritchie, Rogert, Stagg and Sweeney (CRRSS) model. Schwarz and Eikhof (1987) published their expanded FH model for a myelinated rat

2.4 Active Electrical Behavior

nerve at $T = 20^{\circ}\text{C}$ and $T = 37^{\circ}\text{C}$. Schwarz et al. (1995) were the first to develop a model of the human nerve fiber including the nodes of Ranvier also for a temperature of $T = 37^{\circ}\text{C}$.

In this thesis a modified HH-model is presented in the following which fits the specific characteristics for modeling human cochlear neurons. For detailed information see Section 4.1.

Chapter 3

The Human Ear

A basic overview of the anatomy of the human ear and its functionality is presented in the following. Note that only the important information needed for the computer simulations in Chapter 4 is outlined. For more detailed facts several text books are on disposal and [Montpellier \(2007\)](#) offers a very good summary of the human ear.

This chapter provides an introduction of the anatomy of the human ear, especially the inner ear including the sensory cells responsible for hearing in Section 3.1. Further information about human afferent neurons in the cochlea is given in Section 3.2.

3.1 Anatomy

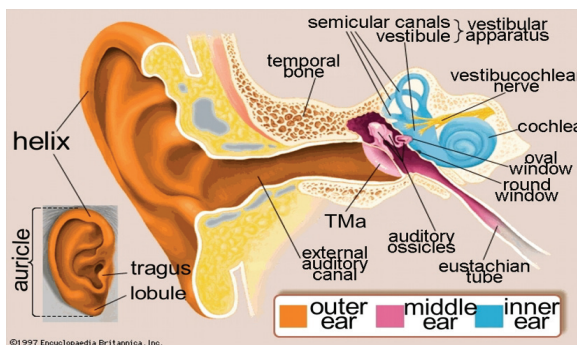


Figure 3.1: Schematic drawing of the human ear which is divided into outer, middle and inner ear with its components. [[Britannica \(2008\)](#)]

The human ear is divided in the outer, middle and inner ear. The outer ear, responsible for collecting sound, consists of the pinna and the ear canal and ends at the surface of the ear drum, also called *tympanic membrane* (TMa). The sound is then amplified in the middle ear, which is an air-filled cavity with the three containing ear bones, called the malleus (or hammer), incus (or anvil) and stapes (or stirrup). The inner ear consists of the cochlea, where the sound is converted into nerve signals, also referred to as the organ of hearing and of the labyrinth which represents the vestibular system. Both are fluid-filled and contain sensory cells, which transmit the motion of the flu-

3.1 Anatomy

ids into electrical nerve signals.

In Section 3.1.1 the basic anatomy and function of the cochlea with its containing organ of Corti are described. The sensory cells, which enable sound perception, are situated in the organ of Corti and also presented in this section. These so called hair cells are distinguished into inner hair cells, which are discussed in Section 3.1.2, and outer hair cells, presented in Section 3.1.3.

3.1.1 Cochlea, Organ of Corti

The cochlea is a spiraled hollow, with 2 1/2 coils in humans and a length of about 35 mm, which is embedded in the temporal bone. It consists of three fluid filled chambers (scalae) separated through certain membranes. The stapes of the middle ear connect the outside of the cochlea at the oval window, adjacent to the *scala vestibuli* (SV) which is the upper chamber of the cochlea. The SV is filled with perilymph, a solution of electrolytes and proteins, which starts to move in waves away from the oval window through the turns of the cochlea when it is stimulated by the stapes.

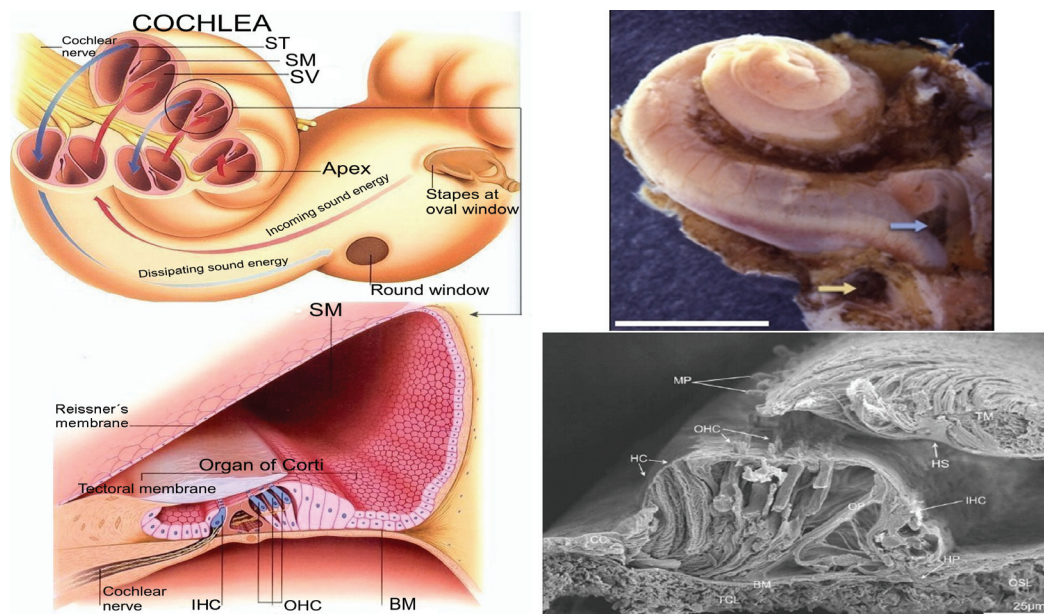


Figure 3.2: Schematic drawing of the whole cochlea and the cross section of one single turn are shown at the left. [Review (2008)] The corresponding microscopy pictures are provided on the right. The top picture shows a human fetal cochlea with a scale bar of 0.5 mm, the blue arrow indicates the oval window the yellow one the round window. [Montpellier (2007)] The lower picture displays a scanning electron microscopy of a human cochlea at approx. 500 Hz. [Glueckert et al. (2005c)]

The lower cavity is called *scala tympani* (ST) and ends in the round window. The

ST is also filled with perilymph and is separated from the SV by the cochlea duct on the whole length of the coiled tube except at the communication area located at the end, the apex, of the cochlea, which is called the helicotrema. At the helicotrema the fluid waves traveling from the oval window through the SV continue in the perilymph of the ST ending at the round window.

The cochlea duct, also called *scala media* (SM) is the third scala which is filled with endolymph, a fluid similar to perilymph but with a higher concentration of potassium and less sodium. The SM is separated from the SV by the Reissner's membrane while the *basilar membrane* (BM), which contains the organ of Corti and decreases in stiffness from base to apex, disunites the SM from the ST.

The *Organ of Corti* (OC) carries the sensory or also called receptor cells, the hair cells, responsible for conducting motion of endolymph, resulting from motion of perilymph in SM and SV, into electrical signals. The OC contains about 15000 hair cells per human ear which are divided into *inner hair cells* (IHCs) and *outer hair cells* (OHCs). This distinction is based on differences in shape and function. The hair cells are organized in four rows along the whole length. There are three rows of OHC, which receive signals from the brain via the medial olivocochlear bundle, and one row of IHC, which transmit nerve impulses to the brain via the vestibulocochlear nerve with the cell body containing spiral ganglion what can also be seen in Fig. 3.2.

Furthermore there exist a tonotopic arrangement of the hair cells, i.e., the hair cells are tuned to certain frequencies and lined up from the oval window for high frequency (20000Hz) tones to the apex of the cochlea for low frequencies (20Hz).

3.1.2 Inner Hair Cell

The IHC is responsible for the transmission of the sound vibration in the peri- and endolymph to electrical signals and for the transport of the coded information to the brain. There exist about 3500 IHCs per human ear.

The IHCs as well as the OHCs are embedded in the epithelium of the OC and therefore in contact with endolymph. The IHC consist of a medial cell body and hairlike structures, called stereocilia, at the top end of the hair cell, which is surrounded by perilymph (Fig. 3.4). One IHC has about 50 of these stereocilia which are connected to each other via certain tip-links, which pair up two adjacent stere-

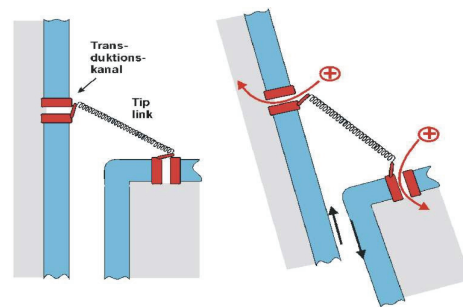


Figure 3.3: Schematic drawing of the tip links of hair cells in the closed state at the left and at the open state at the right. [Frings (2003)]

3.1 Anatomy

ocilia and control voltage dependent ion channels. The function of the tip links is visualized in Fig. 3.3. Furthermore [Glueckert et al. \(2005a\)](#) also observed side-link formation between adjacent stereocilia. The stereocilia of the IHC are aligned with increasing length in one direction, varying from 3.9 to 7.2 μm ([Glueckert et al. 2005c](#)). While the stereocilia at the top detect the stimulus, the area of excitation and synaptic contact with interneurons is found at the bottom of the IHC.

When a stimulus is applied the BM oscillates at a certain area what is referred to as tonotopic behavior. The corresponding stereocilia deflect to the longest stereocilia, ion channels are mechanically opened by stretching of tip links. Due to the more negative charged IHC compared to the endolymph with a high (K^+) concentration, (K^+) influx can be observed. The resulting depolarization causes further opening of the voltage dependent (Ca^{2+}) calcium ion channels in the whole membrane of the IHC what triggers the release of neurotransmitters into the synaptic cleft at the basal end. The adjacent neuron is stimulated, i.e., develops and propagates an AP. The IHCs show a specialty concerning their depolarization after activation. Due to the low concentration of (K^+) ions in the perilymph compared to the IHC after (K^+) influx (and a potential difference of -45mV which is away from the Nernst-Potential of -80mV), potassium ions flow to the perilymph resulting in hyperpolarization of the IHC.

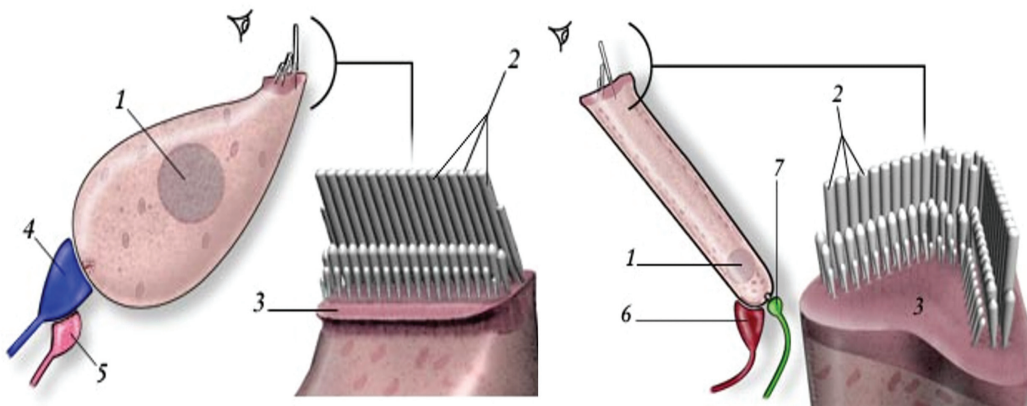


Figure 3.4: Schematic drawing of the IHC on the left and one of the OHC on the right. (1) denotes the nucleus, (2) the stereocilia and (3) the cuticular plate. The innervation is also indicated as described in the text, where (4) defines the radial afferent ending (dendrite of type I neuron) and (5) the lateral efferent ending which innervate the IHC. Concerning the OHC (6) the medial efferent ending and (7) the spiral afferent ending (dendrite of type II neuron) are shown. [[Montpellier \(2007\)](#)]

The IHCs are responsible for bringing information to the brain and therefore mainly afferently innervated. More than 90% of the afferent neurons are myelinated

and connected to IHC via synaptic junctions. These radial afferents are called type I ganglion cells and described in Section 3.2.1.

While one afferent fiber only innervates one single IHC (Fig. 3.5), one IHC forms in average eight synaptic complexes to send neural signals to the brain. A synaptic complex consists of the synapse with a dendrite of a type I cell and one lateral synaptic ending of an efferent fiber (Fig. 3.4), i.e., there is no direct contact to the IHC, acting as a feedback for the afferent fibers.

3.1.3 Outer Hair Cell

The function of the OHC with an amount of 12000 per human ear was uncertain for a long time. Studies showed that they receive signals from the brain, i.e., show mainly efferent innervation and act as an amplifier of low to medium-level sound with an up to hundredfold increase of perception. OHCs are only present in mammals.

OHCs consist also of a cell body, which is situated at the basal end of the hair cell in contrast to the medial perikaryon of the IHC (Fig. 3.4). [Glueckert et al. \(2005c\)](#) reported in man an apical length of OHC of 35-40 μm , while in the lower turn they are only 25-30 μm long. The main difference to the IHC is the cylindrical shape and that the stereocilia of the OHCs show the typically w-form ([Glueckert et al. 2005a](#), Fig. 3.4) with an increase in length namely from 0.4 μm at the innermost row to 5 μm at the outermost row at the 500 Hz region ([Glueckert et al. 2005c](#)). Further investigations showed that one OHC in the 500 Hz region can compromise 80 stereocilia. The stereocilia of the OHCs are not only connected via tip-links the long ones also touch the *tectoral membrane* (TM). In the third row of OHCs they are even connected to the TM, which is shifted against the BM when the area is stimulated.

The transmembranprotein prestin of the OHCs is the reason for their amplifying function. This prestin enables a change in shape of the OHC as a result of a certain voltage change. More precisely the OHC is either capable of shrinking or it might increase 5% in length. When a stimulus is applied the OHC depolarizes as a result of potassium influx which occurs due to stretching of the tip-links similar to the IHC. The voltage-dependent confirmation of the prestin changes and the OHCs contract. When the OHC is hyperpolarized it enlargens again. Therefore the OHCs cause the

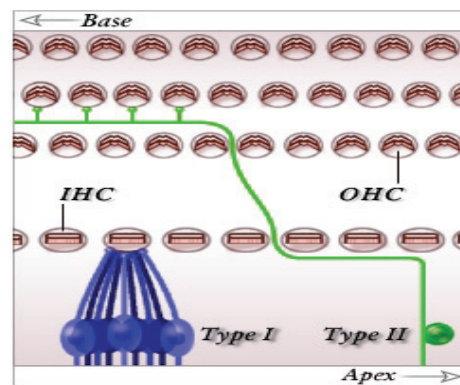


Figure 3.5: Typical afferent innervation pattern of IHC which are innervated by single afferents but more than 10 OHCs are connected to a single type II neuron. [[Montpellier \(2007\)](#)]

touching TM to vibrate with the frequency of the arriving tone. The prestin enables a very fast change in length with up to 20000 changes per second. Due to the moving TM the vibration of the BM is amplified which helps the IHC to detect sound (Zheng et al. 2000, Dallos et al. 2008).

Although the innervation pattern of OHC certainly changes along the cochlea turns from base to apex, the OHC are mainly innervated by medial efferents. These fibers need to cross the *Tunnel of Corti* (TC) to reach the synaptic ends of the OHCs. According to Glueckert et al. (2005a) the diameter of these efferents varied extensively from 0.2 to 1.5 μm . Their findings on the course of these fibers are a valuable extensions to the pioneering work of Spoendlin and Schrott (1989).

Nevertheless the OHC are also innervated by at least 5% of the afferent fibers with an increasing amount in apical regions. These spiral afferents are nonmyelinated and called type II spiral ganglion cells which are described in Section 3.2.1. In contrast to the IHC, one type II neuron innervates ten or more OHCs, sometimes also from different rows although the usually innervate the same row as presented in Fig. 3.5.

The typical synaptical arrangement consists of a large synapse with the medial efferent and a undersized one with the small afferent (Fig. 3.4). Increasing afferent innervation is only present in the very apical region of the cochlea.

3.2 Afferent Cochlear Neurons

A short overview of the anatomy and differences between cochlear neurons is provided in Section 3.2.1. Section 3.2.3 describes the typical detailed structure of an afferent cochlear neuron. Two outstanding differences in morphological features in man compared to mammals are presented in Section 3.2.2.

3.2.1 Anatomy and Classification

As mentioned before the electrically coded information from the cochlea is transmitted via the cochlear nerve to the brain. The cochlear nerve is part of the vestibulocochlear nerve, also called the VIII cranial nerve. The cochlear neurons are synaptically connected to the hair cells, then bundled together to form the cochlear nerve with its spiral ganglion, i.e., the packed cell bodies, to finally enter the brainstem and form synapses to the cochlear nucleus.

A human ear has 30000 to 35000 cochlear neurons, all are classified as bipolar nerve cells. Otte et al. (1978) reported 35000 afferents in young individuals and 29000 in adults and Spoendlin and Schrott (1989) found from 32000 to 31000 myelinated nerve fibers in the cochlear nerve of normal hearing individuals and a lower number in case of sensory neural deafness.

Due to their structural classification cochlear neuron consists of the soma and two distinct processes symmetric to the cell body. One is called the peripheral process or

3.2 Afferent Cochlear Neurons

peripheral axon and can also be defined as the dendrite, the other one is called axon, central axon or is referred to as the central process. Usually the central process has twice the diameter of the peripheral process and according to [Spendlin and Schrott \(1989\)](#) the average diameter of the central axons is $2.5 \mu\text{m}$ but range of calibers increase with age. There exist a wide variety of cochlear neurons concerning their lengths, diameters, myelination of the two processes and the soma. The typical arrangement which is also used for the following computer simulations are presented in Section 3.2.3.

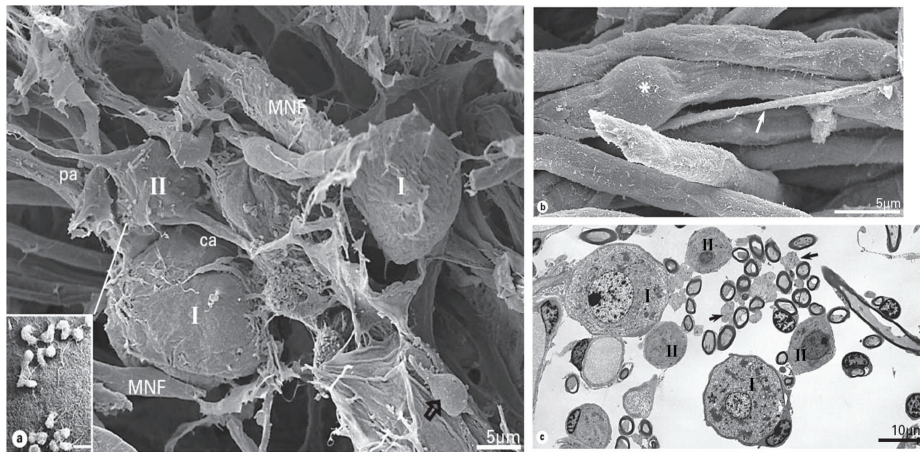


Figure 3.6: Left: *Scanning Electron Microscope* (SEM) picture with type I (I) and type II (II) cells in the upper basal turn of the cochlea. Central (ca) and peripheral (pa) axons of a type II cell are much thinner than myelinated nerve fibers (MNF) from type I cells. The insert shows a higher magnification of the surface coat of a Schwann cell covering a type II neuron; scale bar = 500 nm . Top right: SEM picture of myelinated nerve fibers and an unmyelinated (arrow) one. Asterisk shows bulging of a Schwann cell nucleus. Bottom right: *Transmission Electron Microscope* (TEM) showing both myelinated and unmyelinated (arrows) nerve fibers. Small type II SGCs (II) and large type I cells (I) can be seen. Lower type I cell is wrapped by a thin myelin sheath (star). [[Glueckert et al. \(2005b\)](#)]

Observing cochlear neurons mainly two types of cells can be distinguished. The majority of cells, with an amount of more than 90% are the type I cochlear neurons, which are large and myelinated as can be seen in Fig. 3.6. Therefore type I cells are ensheathed with glia cells with up to 30 layers. Due to the numerously contained mitochondria in the cell body and a diameter of about $30 \mu\text{m}$ ([Glueckert et al. 2005b](#)), type I cells are believed to be highly metabolic. As mentioned before the type I cells innervate single IHC of the organ of Corti.

The other 5-10% of cochlear neurons are called type II cochlear cells and are small in size compared to type I cells, e.g., the diameter of the perikarya is about $15 \mu\text{m}$ ([Glueckert et al. 2005b](#)). The main difference is that they are unmyelinated

and innervate as many as ten or more OHCs usually in one row at the same time by crossing the TC (Fig. 3.5 and 3.6). Furthermore [Hossain et al. \(2005\)](#) suggested that the lack of myelination of type II afferents cause a decay in OHC outputs compared to type I cells. Differences in (Na^+) channel distribution among type I and type II cells can also be observed ([Hossain et al. 2005](#)).

3.2.2 Human Specialties

Many authors reported distinct differences between the human cochleae and those of other mammals, e.g., [Tylstedt and Rask-Andersen \(2001\)](#), [Tylstedt et al. \(1997\)](#), [Glueckert et al. \(2005b\)](#). Although [Nadal \(1988\)](#) reports major differences among species concerning the length and width of the BM, the number and length of IHCs and OHCs as well as the number of nerve terminals per hair cell, the two outstanding human specialties are the nonmyelinated soma of cochlear neurons and the appearance of the so called clusters. These morphometric specialties are speculated to be related to the speech processing and coding mechanism in the human cochlea ([Tylstedt and Rask-Andersen 2001](#)).

Among others [Tylstedt and Rask-Andersen \(2001\)](#) reported that whereas the cell bodies of the acoustic ganglion are myelinated in other animals, the spiral ganglion perikarya in humans are unmyelinated, indicating a slower conductance rate in man. According to [Glueckert et al. \(2005b\)](#) the majority of the population, with about 94% are nonmyelinated, with an increasing rate of myelination in aged individuals ([Ota and Kimura 1980](#)).

The performed computer simulations showed problems resulting from the human nonmyelinated soma, caused by the current loss at the soma region due to the large diameter of the soma in comparison with the presomatic region. Because N layers of myelin act as N capacitors in series, most of the current is needed to load the capacitor of the soma. [Rattay et al. \(2001a\)](#) reported a larger time delay of the traveling AP from the peripheral to the central axon compared to the cat or other mammals with myelinated soma, e.g., $330 \mu s$ in man and $118 \mu s$ in the cat. According to [Rattay et al. \(2001a\)](#) the safety factor for the generation of an AP is small, i.e., small changes in certain sensitive parameters cause the absence of AP propagation.

Further investigations concerning these sensitive parameters around this critical nonmyelinated area are presented in Chapter 4.

Another specialty of human cochlear neurons was investigated by [Tylstedt et al. \(1997\)](#). With their TEM studies they described unit-like structures of neurons in the regions where ganglion cells lay close to each other, i.e., in the middle and upper turn of the cochlea. In the apical turn, e.g., [Pamulova et al. \(2006\)](#) found 3694 myelinated fibers representing 10% of the total number of fibers innervating the cochlea. At this sites adjacent neurons often faced each other and were ensheathed by the same Schwann cells at the soma region. This structural or metabolic unit is called neuronal cluster

3.2 Afferent Cochlear Neurons

(Fig. 3.7). [Tylstedt et al. \(1997\)](#) reported that as many as four neurons could share one cluster and that up to 20% of the type I neurons make direct physical contact with neighbouring nerve cells, with an intercellular cleft of approximately 15 to 20 *nm* ([Tylstedt and Rask-Andersen 2001](#)). It remains unknown if the neurons in one cluster innervate the same group of hair cells. At these contact sites electric transmission is believed to occur between nerve elements with a resulting ephaptic neural interaction between enclosed neurons, as suggested by [Tylstedt and Rask-Andersen \(2001\)](#).

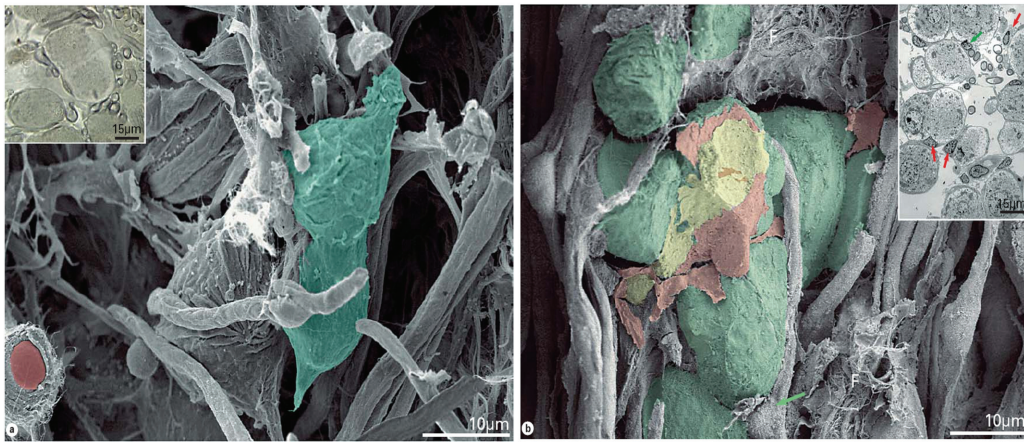


Figure 3.7: Left: (SEM) view of type I cells in the upper basal turn at approximately 2kHz region. Two cells are enwrapped by the same Schwann cells forming a structural unit (colored green). The inset shows also neurons enwrapped by common Schwann cells (arrow). Right: Type I human spiral ganglion cells, colored green in the middle turn at approximately 500Hz to 1kHz region. Neurons are arranged in dense clusters. Spaces between are filled with cell bodies from surrounding satellite cells (selected Schwann cells are colored yellow and red). The inset shows a TEM section of an undecalcified human cochlea. Cells between spiral ganglion neurons may belong to Schwann cells surrounding perikarya of neurons (red arrows) or Schwann cells surrounding nerve fibers (green arrows). [[Glueckert et al. \(2005b\)](#)]

Due to the findings of [Tylstedt et al. \(1997\)](#) a complex neuronal interaction, i.e., a more complex processing of signals, is suggested, which remains to be investigated with computer simulation. [Tylstedt and Rask-Andersen \(2001\)](#) also indicated the relevance of the cell cluster concerning nerve cell survival after hair cell loss, thus also explaining the slow rate of retrograde degeneration of human cochlear neurons. For detailed information on degeneration see [Felder et al. \(1997\)](#).

A first approach for describing the physical properties of a cluster and simulating its interaction with the included neurons is presented in Chapter 4.

3.2.3 Detailed Structure

In order to model a human cochlear neuron and simulate its spiking behavior, the electrical properties as well as the detailed structure of cochlear neurons needs to be investigated. As mentioned before neurons, including type I and type II neurons, differ in shape and size. Nevertheless a typical arrangement of a human cochlear neuron which is also used in this thesis and in comparison one of a cat are presented in the following (Fig. 3.8).

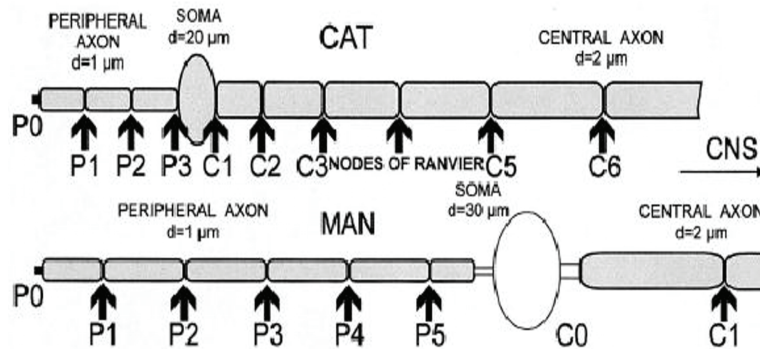


Figure 3.8: The ultrastructure of the cat and human cochlear neurons. [Rattay et al. (2001a)]

Most parts of the neurons are myelinated except the synaptic ending of the peripheral process (P0 in Fig. 3.8), with a length of $10\ \mu\text{m}$, and in men the pre- and postsomatic region and the soma itself.

The diameter of the peripheral and central processes change significantly among different neurons and especially vary in different regions of the cochlea. Nevertheless the contrast between man and cat diameters are rather small with slightly higher values for humans. Liberman and Oliver (1984) reported for cats central diameters between 2.31 and $2.54\ \mu\text{m}$ and 1.19 to $1.44\ \mu\text{m}$ for the peripheral processes respectively.

The diameter of cell bodies of cochlear neurons and also their positions show similar variations. The measured values of human perikarya of type I neurons are between 25 to $30\ \mu\text{m}$ (Spendlin and Schrott 1989) and for the cat about $20\ \mu\text{m}$ (Liberman and Oliver 1984). The position of the human soma depends on the number and lengths of soma preceding internodes, i.e., the myelinated region between two nodes of Ranvier.

These internodes vary in length which has not been well investigated till present time nevertheless it is assumed that the last presomatic internode needs to have reduced length to ensure the propagation of the AP over the soma region as reported by Rattay et al. (2001a). Even the number of peripheral internodes vary, but for this thesis six are supposed to precede the soma resulting in a length of $2.3\ \text{mm}$ for the distance from the terminal P0 to the soma.

3.2 Afferent Cochlear Neurons

In comparison to those variations the three presomatic internodes in the cat are generally present as reported by [Liberman and Oliver \(1984\)](#). Anatomical and morphometric differences of cochlear neurons in man and cat result in different spiking behavior. As most experimental investigations are done with cats, generalization to the human case can be misleading.

The standard values of all these geometrical properties used for the computer simulations in this thesis are summarized in [Table 4.1](#).

Chapter 4

Computer Simulation

Due to the first mathematical model proposed by HH for the ionic currents in neurons and other models which followed, e.g., for the ion channel gating in the nodes of Ranvier as mentioned in Section 2.4.2, computer simulations have been performed to examine the excitability of nerve cells including also cochlear neurons. Since single compartment models which first were implemented cannot explain many phenomena concerning the excitation, spatial models were developed using also finite element methods.

Nevertheless most of the models used for computer simulation of the human cochlear neurons were based on the geometry of animals and since men show outstanding specialties concerning these parameters (Section 3.2.2) the performed simulations might not predict the spiking behavior in a desirable way. This chapter provides computer simulations particularly for the human geometry of cochlear nerve cells.

In Section 4.1 the mathematical model for simulating the excitation of neurons is presented. Simulations concerning the sensitive parameters of the nonmyelinated soma in humans are provided in Section 4.2. A first approach to model the influence of a soma surrounding cluster of the theoretical case of a single cochlear neuron with the predicted mathematical model is introduced in Section 4.3, whereas the initial results for multiple neuron cluster are given in Section 4.4.

4.1 Compartment Model

First of all a proper model needs to be derived for describing the electrical properties involved in the excitation process of a neuron in an applicable way. Furthermore an equation for the membrane potential V_m as a function of time needs to be obtained to observe the changes during stimulation across the whole neuron.

To describe complex systems and the interaction of its components, compartment modeling is a popular way to derive a mathematical model. This method can be applied to pharmacokinetics as well as epidemiology and is of use for simulations in

disciplines like biomedicine or physics. The basic idea is to divide the whole system into subunits, defined as homogeneous entities called compartments resulting in increased transparency of the complex system. These compartments interact with their neighbors, e.g., the axonal resistivity current from one compartment to its adjacent in the model of this thesis, which is described in the following.

The cochlear neuron is divided into compartments (Fig. 3.8), namely the terminal region P0, i.e., postsynaptic region, the peripheral and central nodes of Ranvier and internodes, the pre- and postsomatic region and the soma itself. The presomatic region is subdivided in three compartments for computational reasons (Rattay et al. 2001a). All these compartments show different membrane composition and parameters, e.g., the axonal resistivity or the amount of myelin sheets (Tables 4.1 and 4.2). The electrical circuits of the compartments around the soma and their interfaces are shown in Fig. 4.1.

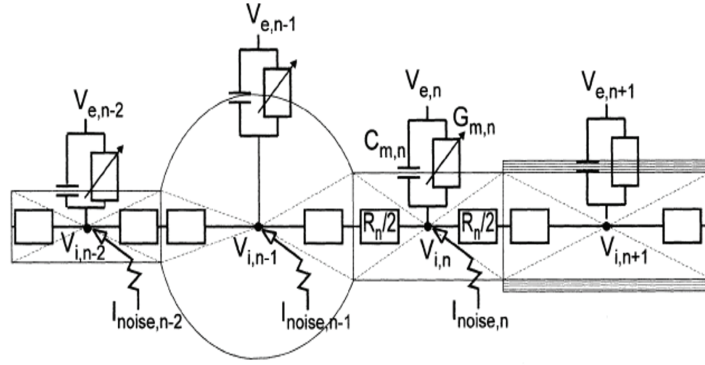


Figure 4.1: Schematic drawing of the equivalent circuit model around the soma region. Note the myelin sheet at the first postsomatic internode and the resulting constant resistance. [Rattay et al. (2001a)]

The equivalent circuit diagram of the soma region is illustrated which is used to derive a mathematical model based on physical laws concerning electrical circuits.

Investigating the current to the central point of the n -th compartment in Fig. 4.1 shows that the total current consists of the capacitive current $I_{capacitive,n}$, the ionic transmembrane current $I_{ion,n}$ and the ohmic currents $I_{ohm,n}$ to the adjacent compartments. Therefore and by applying Kirchhoff's law, which states that the sum of the total current must equal zero, it follows

$$I_{capacitive,n} + I_{ion,n} + I_{ohm,n} = 0. \quad (4.1)$$

According to Ohm's Law, which states that $V = IR$, the axial current I_{ax} , where R is the axial resistivity and V the voltage between two central points of neighboring

4.1 Compartment Model

compartments, is given as

$$I_{ohm} = I_{ax} = \frac{V}{R}. \quad (4.2)$$

The capacitance is given as $C = \frac{Q}{V}$ and the current can be expressed by means of the charge Q as $I = \frac{dQ}{dt}$. Therefore the general capacitive current is given as

$$I_{capacitive} = C \frac{dV}{dt}. \quad (4.3)$$

There are two types of assumptions for the ionic currents of a compartment depending on its electrical behavior. The internodes are myelinated and therefore considered to be of the passive type. The ionic current for these compartments where the constant conductance acts as a resistor results from Ohm's law and is therefore given as

$$I_{ion,n} = G_{intern} V_n A_n / nm_n, \quad (4.4)$$

where G_{intern} denotes the conductance of one layer of membrane of the internodes and is reverse proportional to the resistivity (Table 4.2). nm_n is defined as the number of myelin layers ensheathing the internode. For the surface A_n of all compartments except the soma $A_n = \pi d_n l_n$ holds (d, diameter; l, length), i.e., they are cylindrically approximated whereas the soma is spherically represented which are calculated differently (Rattay et al. 2003).

For all the other compartments which are nonmyelinated (terminal, nodes, pre- and postsynaptic compartment, soma) and have direct contact to the ECS through gating channels the HH equations are used to compute the sodium and potassium ionic current and the leakage current. Therefore the ionic current of the n-th active compartment is given as

$$I_{ion,n} = A_n i_{ion,n} + I_{noise,n} = A_n (i_{Na,n} + i_{K,n} + i_{L,n}) + I_{noise,n}. \quad (4.5)$$

$I_{noise,n}$ denotes the ion channel fluctuations which can be calculated by $I_{noise,n} = GAUSSk_{noise} \sqrt{A_n G_{Na,max}}$ in μA . Although these fluctuations play an important role in modeling the excitation behavior of neurons this calculation has been omitted in this thesis (Chapter 5).

Due to the effect of temperature on the HH model described in Section 2.4.2 and the fact that human neurons operate at 37°C two modifications have to be applied. On the one hand the gating processes are accelerated by the common factor 12. Due to the 10-fold density of channels at the nodes of Ranvier all conductances, i.e., the sodium, potassium and leakage conductance at the nodes have to be multiplied by the factor 10 on the other hand (Table 4.2).

$C_{m,n}$ is defined as the membrane capacitance of the n-th compartment and is evaluated by $C_{m,n} = A_n c_{m,n}$, where $c_{m,n}$ denotes the specific membrane capacitance which is reverse proportional to the numbers of myelin layers of the compartment. R_n describes the axoplasmatic resistance to its neighbors and is calculated by $R_n/2 =$

4.1 Compartment Model

$(2\rho_i l_n)/(d_n^2 \pi)$ with the exception of the soma (Rattay et al. 2003). Summing up these results and denoting $V_{i,n}$ as the intracellular potential at the n-th compartment and $V_{e,n}$ respectively as the extracellular potential it follows that

$$C_{m,n} \frac{d(V_{i,n} - V_{e,n})}{dt} + I_{ion,n} + \frac{V_{i,n} - V_{i,n-1}}{R_n/2 + R_{n-1}/2} + \frac{V_{i,n} - V_{i,n+1}}{R_n/2 + R_{n+1}/2} = 0. \quad (4.6)$$

By introducing the reduced membrane potential for the n-th compartment $V_n = V_{i,n} - V_{e,n} - V_{rest,n}$ the derived differential equation for this membrane potential can be written as

$$\begin{aligned} \frac{dV_n}{dt} = & \left[-I_{ion,n} + \frac{V_{n+1} - V_n}{R_{n+1}/2 + R_n/2} + \frac{V_{n-1} - V_n}{R_{n-1}/2 + R_n/2} \right. \\ & \left. + \frac{V_{e,n+1} - V_{e,n}}{R_{n+1}/2 + R_n/2} + \frac{V_{e,n-1} - V_{e,n}}{R_{n-1}/2 + R_n/2} \right] / C_n. \end{aligned} \quad (4.7)$$

If no stimulating electrode and surrounding cluster is present in the ESC it is assumed that $V_e = 0$ holds and therefore the equation reduces to

$$\frac{dV_n}{dt} = \left[-I_{ion,n} + \frac{V_{n+1} - V_n}{R_{n+1}/2 + R_n/2} + \frac{V_{n-1} - V_n}{R_{n-1}/2 + R_n/2} \right] / C_n. \quad (4.8)$$

For simulating the spiking behavior of a cochlear neuron a stimulus current needs to be applied to initialize the excitation process. In this thesis two cases are implemented in the program code to perform the different simulations. There is the possibility to inject a current at the postsynaptic terminal or directly at the soma. To account for this injection this current is subtracted from the ionic current, therefore it holds

$$I_{ion,n} = I_{ion,n} - I_{inj,n} \quad (4.9)$$

for n equals 1 or represents the soma compartment. $I_{inj,n}$ is about $0.0005 \mu A$ for a stimulation of the terminal compartment and approximately $0.005 \mu A$ for the soma stimulation.

The following simulations have been done with the software called *Advanced Continuous Simulation Language* (ACSL), which was designed for modeling continuous systems described by time-dependent, nonlinear differential equations. Typical applications of ACSL include among others control system design, chemical process dynamics, power plant dynamics, toxicology models and robotics. ACSL basically consists of two parts, on the one hand the program which defines the mathematical model and on the other hand the Runtime commands which execute the simulation and control the parameters.

ACSL provides several integration algorithm. For this thesis the Runge Kutta Algorithm of fourth order with fixed stepsize was used.

4.1 Compartment Model

Geometrical Parameter		
lengths of nonmyelinated regions	terminal	$10 \times 10^{-4} \text{ cm}$
	nodes	$2.5 \times 10^{-4} \text{ cm}$
	presomatic	$100 \times 10^{-4} \text{ cm}$
	soma	$30 \times 10^{-4} \text{ cm}$
	postsomatic	$5 \times 10^{-4} \text{ cm}$
lengths of myelinated regions	li(1)	$210 \times 10^{-4} \text{ cm}$
	li(2)	$390 \times 10^{-4} \text{ cm}$
	li(3)	$440 \times 10^{-4} \text{ cm}$
	li(4)	$350 \times 10^{-4} \text{ cm}$
	li(5)	$440 \times 10^{-4} \text{ cm}$
	li(6)	$360 \times 10^{-4} \text{ cm}$
	central Internodes	$500 \times 10^{-4} \text{ cm}$
diameter	peripheral	$1 \times 10^{-4} \text{ cm}$
	soma	$30 \times 10^{-4} \text{ cm}$
	central	$2 \times 10^{-4} \text{ cm}$

Table 4.1: Geometrical model parameters of the human cochlear neuron used in this thesis.

Electrical Parameter		
Resistivity	intracellular	$0.05 \text{ k}\Omega \text{ cm}$
	extracellular	$0.3 \text{ k}\Omega \text{ cm}$
myelin layers	peripheral internode	40
	nonmyelinated compartments	1
	central internode	80
Capacitance of cell membrane	$1 \mu\text{F cm}^{-2}$	(for one myelin sheet)
Conductances nonmyelinated	terminal	HH model(10/k=12)
	nodes	HH model(10/k=12)
	presomatic	HH model(10/k=12)
	soma	HH model(k=12)
	postsomatic	HH model(10/k=12)
Conductance Internode	$G_{intern} = 1 \text{ mS cm}^{-2}$	

Table 4.2: Electrical model parameters of the human cochlear neuron used for the model of this thesis. HH model(10) indicates that the sodium, potassium and leakage conductances are multiplied by the factor 10 to account for the 10-fold channel densities. HH model(k=12) denotes the warmed HH model where the gating variables are sped up by the factor 12.

4.2 Nonmyelinated Soma - Sensitive Parameters

Due to the morphometric differences between human and animal, especially the human nonmyelinated soma of the cochlear neurons, this chapter enlightens the accountable parameters for this human specialty which is believed to enable direct physical and electrical contact between different cochlear neurons and therefore more complex coding of speech perception especially in low frequency tone areas (Tylstedt and Rask-Andersen 2001).

The ability of an AP to overcome the nonmyelinated soma region depends of very small changes in these distinct parameters. For this reason the variation of these sensitive parameters are discussed in the previous subsections. A standard case for the parameters as well as the results of varying the internal resistivity ρ_i is defined in Section 4.2.1. For the results of the altering amount of myelin ensheathing layers see Section 4.2.2. The differences of varying length of the presomatic compartment are enlightened in Section 4.2.3. In Section 4.2.4 the results for different diameter of the peripheral process are presented, the results for the length of the last peripheral internode are found in Section 4.2.5.

4.2.1 RHOI

To analyze the results of the changes in the sensitive parameters of a cochlear neuron a standard case for all these parameters is defined and listed in Table 4.3, where l_{soma_p} represents the length of the presomatic region which is divided into three compartments as noted previously. The diameter of the peripheral process is denoted by $d(1)$ and $d(soma)$ defines the diameter of the speric soma itself in the following. Note that this standard case represents an excitation with a strong safety factor for spike conduction due to the three layers of myelin at the soma abbreviated by nm_{soma} in the standard case.

Standard Case				
ρ_i	nm_{soma}	l_{soma_p}	$d(1)$	$li(6)$
$0.05 \text{ k}\Omega \text{ cm}$	3	$100 \times 10^{-4} \text{ cm}$	$1 \times 10^{-4} \text{ cm}$	$360 \times 10^{-4} \text{ cm}$

Table 4.3: Standard case values of the sensitive parameters investigated in the following leading to thresholds for an AP to overcome the nonmyelinated soma region.

To predict the exact value of the variated parameter for which the propagation of an AP fails the stepsize is chosen as small as possible around the critical value. Three pictures are provided for each altering parameter with different sites around the soma region, i.e., the results for the last presomatic internode, the first presomatic compartment and the soma are shown, to provide an investigation of the whole cochlear neuron.

4.2 Nonmyelinated Soma - Sensitive Parameters

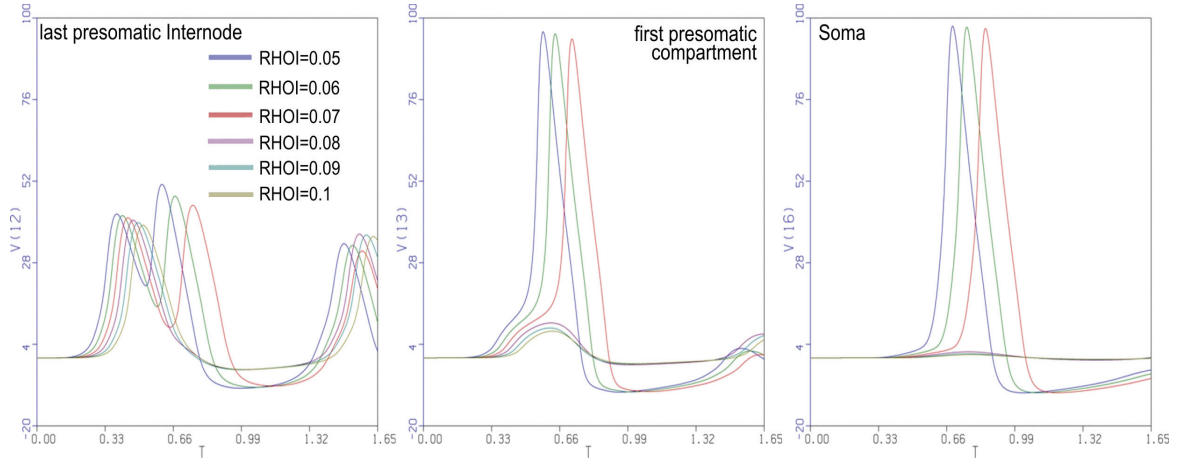


Figure 4.2: The neuronal signal at the soma region with varying ρ_i , starting from 0.05 to 0.1 $k\Omega cm$.

The standard value for the intracellular resistivity ρ_i is 0.05 $k\Omega cm$. The propagation of the AP fails with increasing ρ_i . In Fig. 4.2 six graphs are shown for different ρ_i values, starting from 0.05 to 0.1 $k\Omega cm$ with a stepsize of 0.01 $k\Omega cm$. The first three values up to a resistivity of 0.07 $k\Omega cm$, represented by the blue, green and red graphs, lead to an AP. The first one which fails is the purple graph which denotes a resistivity of 0.08 $k\Omega cm$.

Additionally it can be observed that the fastest propagation of an AP is provided by the standard value of 0.05 $k\Omega cm$. This blue graph also shows a slightly higher peak of the potential V_m , i.e., a stronger excitation of the neuron, especially before the soma with increasing adaption at the perikarya and following compartments.

4.2.2 nmsoma

For the examination of the influence of the number of myelin layers a simulation has been done for five different values starting from only one myelin layer to five insulating sheets covering the soma. The results are shown in Fig. 4.3 and they reflect the strong safety factor of the chosen standard values as mentioned before.

This safety factor means that the five graphs do not show great differences, i.e., the excitation behavior of the five values appears to be very similar as can be predicted from the results of the last internode and the first presomatic region. Therefore every value for myelin layers leads to an ongoing propagation of the AP if the other sensitive parameters are chosen according to Table 4.3.

Only at the soma the graphs differ in strength and velocity where it is obvious that the strongest and fastest excitation is provided by five layers of myelin, represented by the teal graph. In this case even one layer of myelin, represented by the blue graph,

4.2 Nonmyelinated Soma - Sensitive Parameters

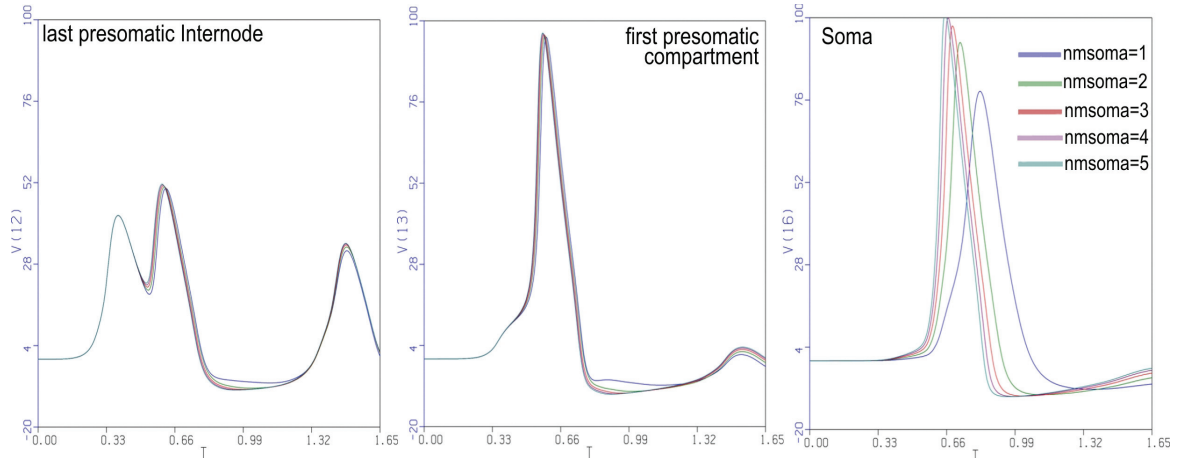


Figure 4.3: The neuronal signal at the soma region with varying nm_{soma} , from 1 to 5.

leads to an excitation of the soma but with a significant decrease in strength and a delay of about 0.15 ms compared to the teal and purple graphs.

4.2.3 $lsoma_p$

The changes in the excitation of a neuron concerning altering $lsoma_p$, the length of the presomatic compartment, are illustrated in Fig. 4.4. Six cases are shown starting with the failing value of $70 \times 10^{-4}\text{ cm}$ and using a stepsize of $5 \times 10^{-4}\text{ cm}$ leading finally to a length of $95 \times 10^{-4}\text{ cm}$ that is close to the standard case value.

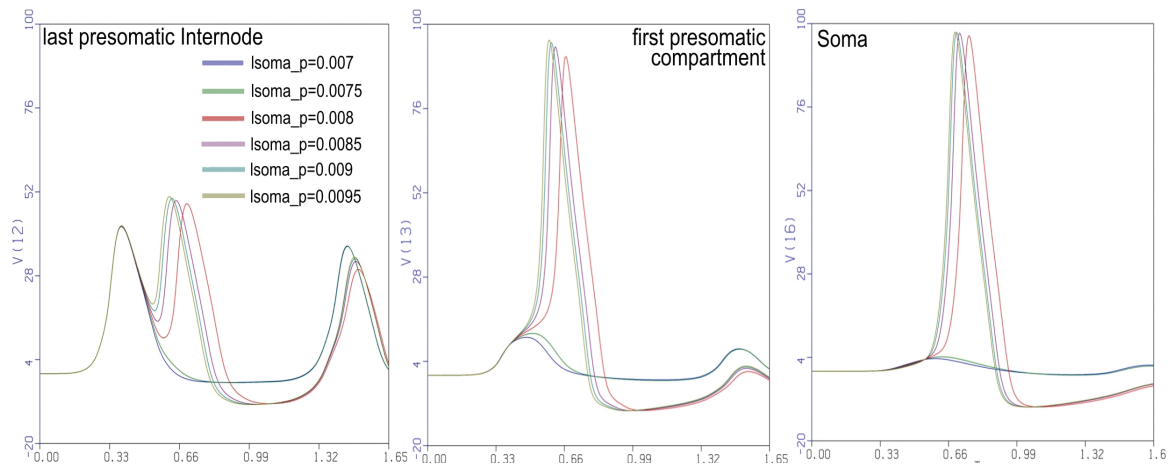


Figure 4.4: The neuronal signal at the soma region with varying $lsoma_p$, from 0.007 to 0.095 cm .

Already at the last presomatic internode it is obvious that the excitation fails for the values of $70 \times 10^{-4} \text{ cm}$ and $75 \times 10^{-4} \text{ cm}$ represented by the blue and the green graph which leak the second rising phase. At the first presomatic compartment the increasing strength and velocity with increasing length is noticeable whereas at the soma all the succeeding graphs show nearly the same maximum values for the potential V_m .

The red graph representing a presomatic compartment length of $80 \times 10^{-4} \text{ cm}$, which is the first leading to an ongoing AP throughout the whole neuron, shows a small delay compared to the longer compartments.

4.2.4 $d(1)$

To observe the differences for varying diameter of the peripheral process $d(1)$ five cases are shown in Fig. 4.5. The simulation starts with a thinner peripheral process with a diameter of $0.2 \times 10^{-4} \text{ cm}$ which is also assumed to be the stepsize leading to five different cases up to the standard value for $d(1)$ of $1 \times 10^{-4} \text{ cm}$.

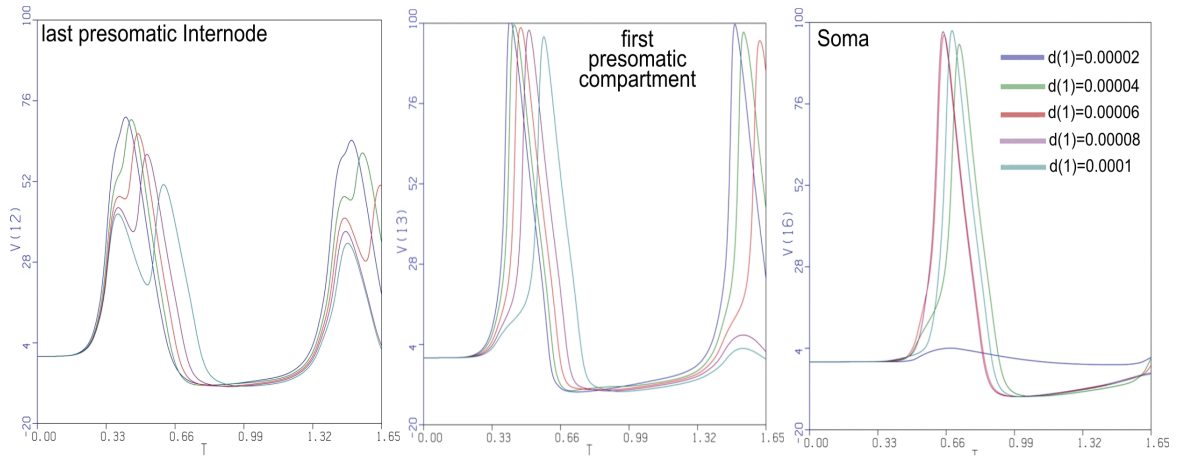


Figure 4.5: The neuronal signal at the soma region with varying $d(1)$, from 0.00002 to 0.0001 cm .

At the last presomatic internode it is obvious that the blue graph, representing the thinnest diameter, is the fastest and also the strongest but leaks the second rising phase after a short fall of V_m . Although it seems that at the first presomatic soma compartment all cases lead to an ongoing propagation of the AP, the thinnest diameter fails to excite the soma as can be seen in Fig. 4.5.

Even if it looks like the velocity and strength of propagation increases from thinnest to thickest diameter as detected at the first presomatic compartment it turns out that the strongest excitation is provided by the teal graph, which represents the thickest diameter and therefore the standard case for $d(1)$ of $1 \times 10^{-4} \text{ cm}$ as can be observed at

the soma. Nevertheless two cases have increased velocity compared to the standard case value.

4.2.5 $li(6)$

The standard value for the length of the last peripheral internode $li(6)$ is $360 \times 10^{-4} \text{ cm}$ and for increasing length the AP fails to overcome the soma region which was also observed by [Rattay et al. \(2001a\)](#). Therefore the simulation for the variation of $li(6)$ showing six different cases starts at a length of $370 \times 10^{-4} \text{ cm}$ and proceeds with a stepsize of $10 \times 10^{-4} \text{ cm}$ up to a length of $420 \times 10^{-4} \text{ cm}$. The results are presented in Fig. 4.6.

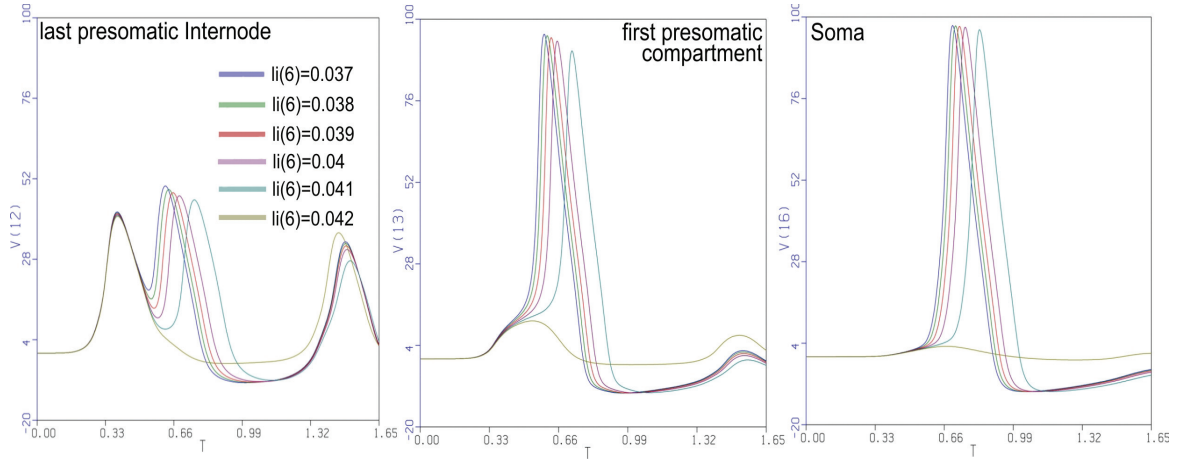


Figure 4.6: The neuronal signal at the soma region with varying $li(6)$, from 0.037 to 0.042 cm .

At the last presomatic internode it is obvious that the peasoup colored graph which represents the longest internode fails to propagate the AP. Also the increasing strength and velocity with decreasing length of the internode can be observed from the beginning. Already at the first presomatic compartment the peasoup graph fails to rise the potential V_m to the threshold and therefore the AP for the longest internode also breaks down at the soma.

It can also be observed that the shortest internodal length represented by the blue graph leads to the strongest excitation at the first presomatic compartment and adapts at the soma to the other successful parameter values. Nevertheless the blue graph is the fastest and a slightly but increasing delay with increasing length of the internode can be observed.

4.3 Cluster - First Results and Consequences

This chapter investigates the electrical properties of a cluster by comparing the membrane potential of one single neuron in the absence and presence of a cluster surrounding the soma region of the neuron. Moreover it is clarified whether the cluster supports the neuron in its spiking behavior and velocity or if the neuron is somehow hindered by its cluster or even limited in its performance and enactment under special circumstances.

The derivation of the equation for the potential of the cluster V^{Cl} , with respect to the predicted properties of the cluster and the believed interaction with the neuronal soma region, is provided in Section 4.3.1. In Section 4.3.2 the geometry of the neuron cluster and the first results of the influence of a cluster obtained by computer simulation are presented.

4.3.1 Mathematical Model

To derive a mathematical model for the potential of a cluster and subsequent adaption of the equation for the potential of an enclosed neuron, some assumptions about the electrical and geometrical properties of a cluster have to be done. This is a rather difficult task because less is known about these properties of neuronal cluster at present time. Due to the still missing investigations, much more experiments and, e.g., TEM studies need to be performed to get a better understanding of the complex interaction.

The passive cluster membrane surrounding several soma regions is assumed to start at the first presomatic compartment and lasts till the postsomatic region and thus the cluster encloses the whole nonmyelinated region around human perikarya.

The electrical properties which are pretended to be similar to those of the passive parts of a cochlear neuron are given in Table 4.4.

Electrical Parameter		
Resistivity	intracellular	$0.05 \text{ k}\Omega \text{ cm}$
	extracellular	$0.3 \text{ k}\Omega \text{ cm}$
Capacitance of cell membrane	$1 \mu\text{F cm}^{-2}$	(for one myelin sheet)
Conductance	$G_{Cluster} = 1 \text{ mS cm}^{-2}$	

Table 4.4: Electrical properties of the cluster surrounding the soma region used for the model of this thesis.

The geometrical properties vary a lot depending of course on the number of neurons ensheathed by the same cluster, e.g., the cluster needs to have a larger diameter for four neurons than for the theoretical case of a single one. In this thesis the cluster consists also of compartments which have the same length as the corresponding compartments of the neuron. In general the cluster therefore consists of five com-

4.3 Cluster - First Results and Consequences

partments accounting for the three presomatic compartments, the soma and the postsomatic compartment. All these cluster compartments especially also the soma are cylindrically approximated to obtain the first results. The geometry is discussed and illustrated in Sections 4.3.2 and 4.4.

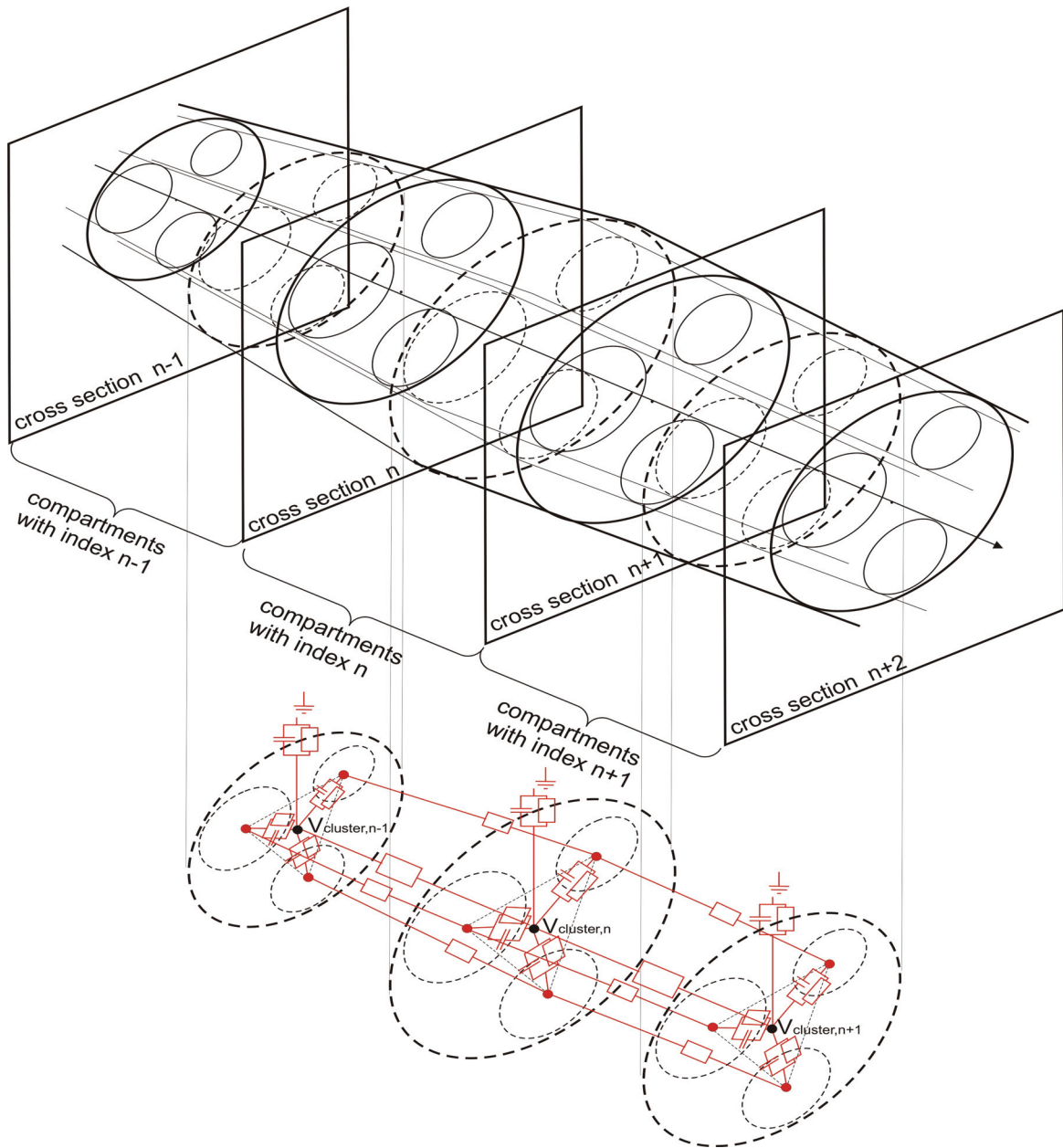


Figure 4.7: Schematic drawing of the equivalent circuit model around the soma region with a supporting cluster.

The predicted electrical circuit is presented in Fig. 4.7. This model expands ideas obtained by Jönsson et al. (2008) and resembles enhanced models like the double cable model of McIntyre et al. (2002) and also a model enriched with an additional current pathway introduced by Ritchie (1995).

Since electrical currents are involved Kirchhoff's law is applied to the central point of the n-th compartment of the cluster. Therefore all involved currents of the n-th compartment are taken into account consisting of the capacitive current of the cluster $I_{capacitive,n}^{Cl}$, the ohmic currents of the cluster to its neighboring compartments $I_{ohm,n}^{Cl}$, the ionic current of the cluster $I_{ion,n}^{Cl}$ and also the transmembrane currents of the j enclosed neurons which involves the ionic and capacitive current of the n-th compartment of these neurons. Therefore $I_{m,n}^k = I_{ion,n}^k + I_{capacitive,n}^k$ denotes the transmembrane current of the n-th compartment of the k-th neuron.

According to Kirchhoff's law the sum of these currents equals zero, e.g. it holds

$$I_{capacitive,n}^{Cl} + I_{ohm,n}^{Cl} + I_{ion,n}^{Cl} + \sum_{k=1}^j I_{m,n}^k = 0. \quad (4.10)$$

The ohmic current of the cluster between compartments is calculated similarly to those of the neuron for computational reasons although this results in a significant limitation of the model discussed in detail in Section 5. For that reason the axial resistance for the n-th compartment of the cluster R_n^{Cl} needs to be evaluated which satisfies the same equation as the cylindrically approximated compartments of the neuron.

The equation for the capacitive current of the n-th compartment of the cluster remains the same with the corresponding parameters for the cluster, namely the capacitance of the n-th compartment of the cluster c_n^{Cl} (Table 4.4) and the number of myelin layers ensheathing the cluster at the n-th compartment nm_n^{Cl} which vary according to the simulation.

The ionic current across the membrane of the n-th compartment of the cluster is of the passive type as concluded previously. Therefore

$$I_{ion,n}^{Cl} = G_{cluster} V_n^{Cl} A_n^{Cl} / nm_n^{Cl} \quad (4.11)$$

holds with the conductance of the cluster $G_{cluster}$ (Table 4.4) and the cylindrically calculated surface of the n-th compartment.

Summing up these results, the differential equation for the reduced potential of the n-th compartment of the cluster V_n^{Cl} can be derived by concluding that the extracellular potential of the cluster $V_{e,n}^{Cl}$ equals zero and therefore the equation can be written as

$$\frac{c_n^{Cl}}{nm_n^{Cl}} \frac{dV_n^{Cl}}{dt} + I_{ion,n}^{Cl} + \sum_{k=1}^j [I_{ion,n}^k + I_{cap,n}^k] + \frac{V_n^{Cl} - V_{n-1}^{Cl}}{R_n^{Cl}/2 + R_{n-1}^{Cl}/2} + \frac{V_n^{Cl} - V_{n+1}^{Cl}}{R_n^{Cl}/2 + R_{n+1}^{Cl}/2} = 0, \quad (4.12)$$

where j denotes the number of neurons enclosed in the cluster, which typically is a value between one and four.

If a surrounding cluster is added the equation for the transmembrane potential of the k -th enclosed neuron V_n^k of course certainly changes and equation 4.8 needs to be adapted for those compartments which are affected by the cluster, i.e., the three presomatic compartments, the soma and the postsomatic region. For all other compartments the equation remains the same. Because the cluster encloses the neurons the potential of the cluster V_n^{Cl} acts as the extracellular potential $V_{e,n}$. Therefore it is concluded that $V_n^{Cl} = V_{e,n}$ holds and the new equation for the potential of ensheathed compartments can be written as

$$\frac{dV_n^k}{dt} = \left[-I_{ion,n}^k + \frac{V_{n+1}^k - V_n^k}{R_{n+1}^k/2 + R_n^k/2} + \frac{V_{n-1}^k - V_n^k}{R_{n-1}^k/2 + R_n^k/2} + \frac{V_{n+1}^{Cl} - V_n^{Cl}}{R_{n+1}^k/2 + R_n^k/2} + \frac{V_{n-1}^{Cl} - V_n^{Cl}}{R_{n-1}^k/2 + R_n^k/2} \right] / C_n^k. \quad (4.13)$$

4.3.2 Single Neuron Cluster

As mentioned before there exist five cylindrical cluster compartments around the soma region which are colored red and illustrated at the top in Fig. 4.8. The cross sections for all compartments are similar except for the diameters of the surrounded neurons and the cluster's diameter depending on the amount of enclosed neurons. The multiple neuron clusters are discussed in Section 4.4. The theoretical case of a single neuron cluster is shown at the left bottom which is the topic of the simulations in this Section to obtain the first results of the influence on the neurons spiking behavior.

The first important difference in the spiking behavior of a single neuron with a soma-ensheathing cluster concerns the sensitive parameters around the soma region responsible for the propagation of an AP throughout the whole neuron.

The simulations for the chosen diameters of 0.0002 cm for the peripheral compartments of the cluster, 0.0004 cm for the postsomatic compartment and 0.004 cm for the soma compartment of the cluster with one layer of myelin surrounding the whole cluster, revealed that the parameter of most importance is the length of the last peripheral internode $li(6)$. Although the standard case parameters for the cochlear neuron were used according to Table 4.5 it turned out that the propagation of the AP fails at the soma compartment if $li(6) \leq 0.031 \text{ cm}$. Therefore the standard value for $li(6)$ of 0.036 cm can not be used for the simulation of the excitation of a cochlear neuron with a cluster.

Whereas without a cluster and with the predicted standard values for the sensitive parameters the intracellular resistivity ρ_i leads to a succeeding AP for values smaller than $0.08 \text{ k}\Omega \text{ cm}$, $\rho_i \leq 0.06 \text{ k}\Omega \text{ cm}$ needs to hold for a neuron with a cluster and a last peripheral internodal length of 0.031 cm . Surprisingly if $li(6)$ is changed to $0.03 \text{ k}\Omega \text{ cm}$

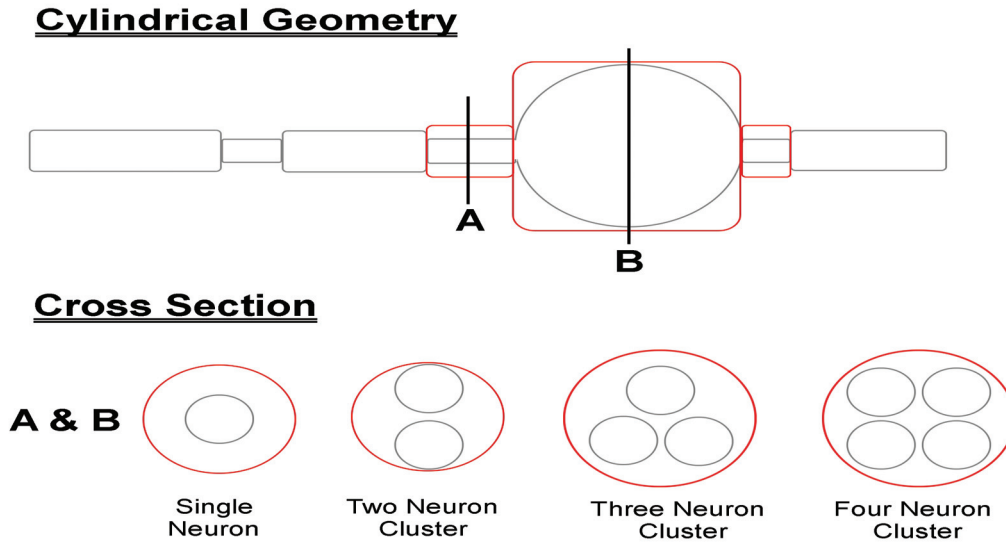


Figure 4.8: Cylindrical compartments of the cluster around the soma region of enclosed neurons are shown in red at the top. The cross section for a single neuron and multiple neurons clusters are presented at the bottom. (A) and (B) are similar but have different diameters.

the AP is able to overcome the soma region with an intracellular resistivity of even $0.08 \text{ k}\Omega \text{ cm}$ and more.

Observing the numbers of myelin layers more severe constraints are examined. Whether the length of the last internode is predicted to be 0.03 or 0.031 cm only three layers of myelin are able to trigger the AP over the soma region. Only if a length of 0.029 cm is assumed two layers reach the threshold for a successful propagation. For the excitation with only one layer of myelin the length needs to be less than 0.027 cm .

The affect of a deviation from the standard value of the length of the presomatic compartment $l_{\text{soma.p}}$ shows a similar behavior. If an internodal length of 0.031 cm is chosen even $l_{\text{soma.p}} \geq 0.0099 \text{ cm}$ needs to hold to assure the propagation of an AP. For $l_i(6) = 0.03 \text{ cm}$ only a small improvement can be observed, i.e., $l_{\text{soma.p}} \geq 0.0095 \text{ cm}$ keeps the AP traveling. To reach the threshold of $l_{\text{soma.p}} = 0.008 \text{ cm}$ which holds for the neuron without a cluster the last internodal length needs to be very small, i.e., $l_i(6) = 0.025 \text{ cm}$.

The determined threshold for the diameter of the peripheral process $d(1)$ of $0.4 \times 10^{-4} \text{ cm}$ in the absence of a cluster is also only reached if $l_i(6) = 0.025 \text{ cm}$ holds. If the length is assumed to be 0.03 the diameter $d(1)$ needs to be larger than $0.77 \times 10^{-4} \text{ cm}$ and only $d(1) \geq 0.93 \times 10^{-4} \text{ cm}$ assures the propagation for a length of 0.031 cm .

Although these first results may indicate that a cluster around the soma of a cochlear neuron only hinders the excitation behavior by decreasing the safety factor it

4.3 Cluster - First Results and Consequences

is shown in the following that under some circumstances the spiking behavior changes in a positive way.

To account for these results the length of the last peripheral internode is changed to 0.03 cm for the following simulation where a cluster is applied even if $li(6) = 0.031\text{ cm}$ would have also been possible but this value is certainly more sensitive to changes in other parameters.

For analyzing the differences in the spiking behavior of a cochlear neuron in the presence and absence of a cluster a program has been implemented in ACSL with a logical switch named `nocluster` to provide direct comparison between the two cases for `nocluster` equals `false` or `true`.

Many simulations have been done with varying numbers of myelin sheets and increasing size of the cluster which revealed surprising results presented subsequently. For a certain number of myelin layers for the soma of the neuron and the cluster itself, six different simulations for altering sizes of the cluster have been performed.

Geometry - varying diameters						
enlargement	$d(1)$	$d^{Cl}(1)$	$d(2)$	$d^{Cl}(2)$	$d(soma)$	$d^{Cl}(soma)$
0%	0.0001	0.0001	0.0002	0.0002	0.003	0.003
1%	0.0001	0.000101	0.0002	0.000202	0.003	0.00303
10%	0.0001	0.00011	0.0002	0.00022	0.003	0.0033
25%	0.0001	0.000125	0.0002	0.00025	0.003	0.00375
50%	0.0001	0.00015	0.0002	0.0003	0.003	0.0045
100%	0.0001	0.0002	0.0002	0.0004	0.003	0.006

Table 4.5: Diameters of the cochlear neuron and its surrounding cluster with increasing size of the cluster used for the following simulation to examine the influence of the cluster according to the spiking behavior of the ensheathed nerve cell (values in cm).

These experiments start with a cluster of the same size as the nerve cell although one should keep in mind that the cluster is approximated cylindrically for all compartments, thus the soma compartment of the cluster has a larger surface than the sphere of the perikaryon of the neuron compartment. To examine the differences in the spiking behavior of the neuron the cluster has been enlarged initially with 1% of the diameter from the corresponding neuron compartments followed by an enlargement of 10%, 25%, 50% and finally 100%, i.e., the cluster has the doubled size of the enclosed neuron. The values of the diameters of the neuron and the cluster compartments are listed in Table 4.5, where $d^{Cl}(1)$ denotes the diameter of the peripheral compartments of the cluster and $d^{Cl}(2)$ that of the central compartment. $d^{Cl}(soma)$ defines the diameter of the soma compartment of the cluster respectively.

The first simulation has been done for the case of one myelin layer at the cluster and one sheet surrounding the neuron compartments. Note that for that case the AP

4.3 Cluster - First Results and Consequences

is nonpropagating if the standard values are applied as examined before.

In the presence of a cluster the AP also fails whether the cluster is of the same size as the neuron or of doubled size. Nevertheless certain differences in the peak of the membrane potential can be observed at the soma compartment as shown in Fig. 4.9.

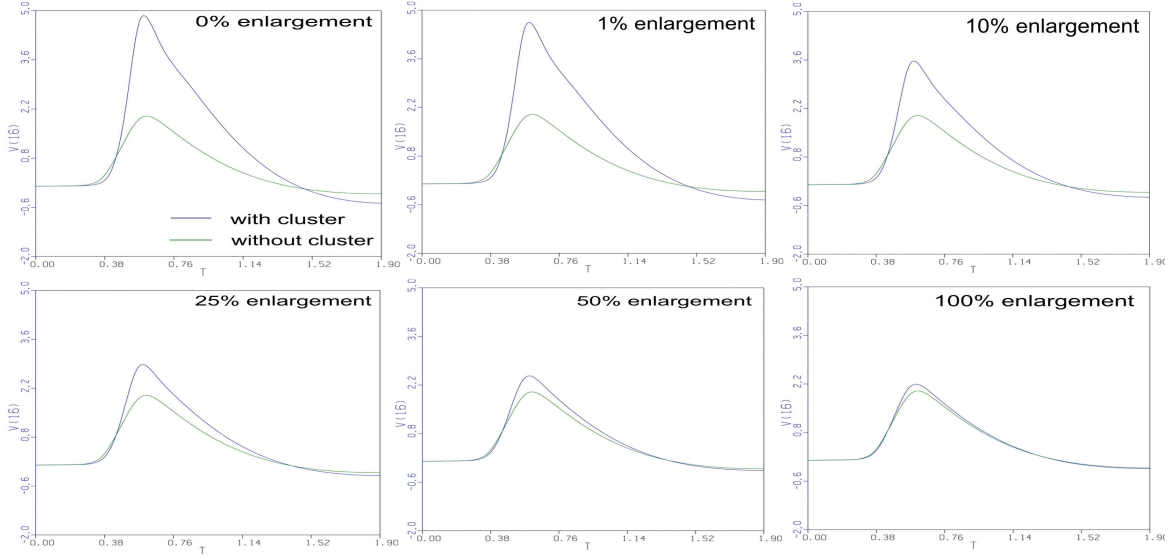


Figure 4.9: Membrane potential at the soma for $nm^{Cl}=1$ (number of myelin sheets surrounding the cluster) and $nm_{soma}=1$ (number of myelin layers supporting the neuron). The green graph states the transmembrane voltage of the neuron and the blue one that with an ensheathing cluster for different sizes of the cluster.

The membrane potential V_m at the soma compartment is presented in Fig. 4.9 where the blue graph states the presence of a cluster surrounding the neuron and the green one describes the case without a cluster.

It is obvious that the peak of the green graph is larger than that of the blue one with its maximum value of 1.9997 mV in all six cases. For a cluster of the same size the maximum value is 4.8578 mV which is an approximately 2.5 fold increase in strength. The maximum value is more than doubled for an enlargement of the cluster of 1% of the neuron size as well.

Nevertheless these maximum values of the blue graphs decreases with increasing cluster size, e.g., when the cluster has the doubled size of the neuron the peak of V_m is 2.1962 mV which resembles only a slightly increase of about 9.8%.

The velocity of the excitation at the soma compartment is not improved for any size of the cluster what might be because the AP is nonpropagating.

The second simulation has been done for two layers of myelin surrounding the

4.3 Cluster - First Results and Consequences

cochlear neuron and still one layer for the cluster. In this case the AP overcomes the soma region and therefore successfully excites the whole neuron.

The results are shown in Fig. 4.10 which represents again the membrane potential V_m of the soma compartment as a function of time for the two cases to compare the absence and presence of the cluster and therefore to investigate its influence on the spiking behavior of the enclosed neuron.

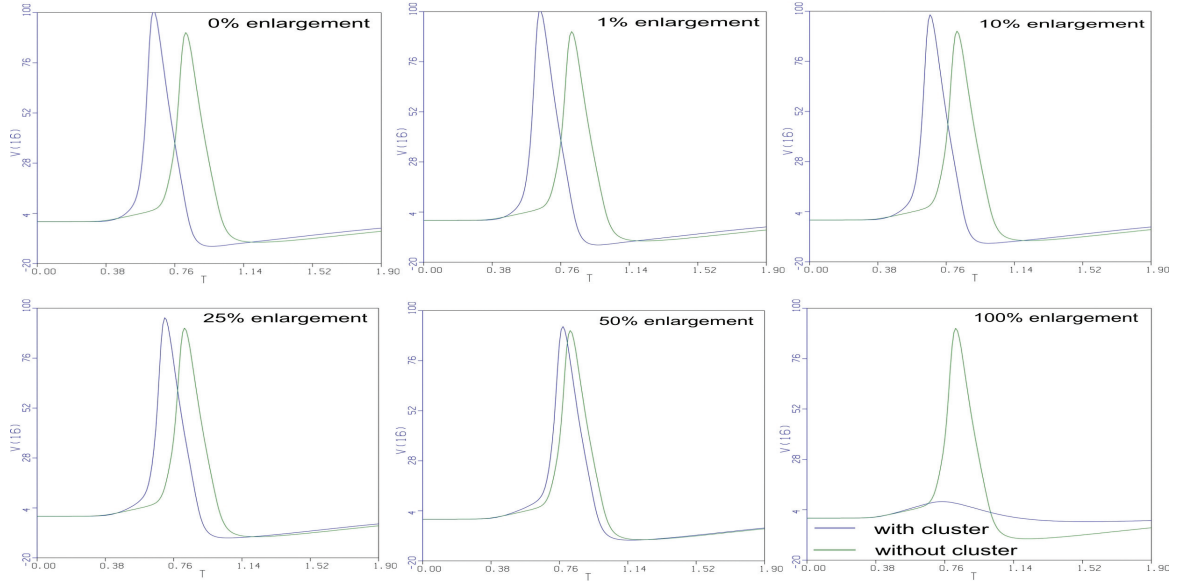


Figure 4.10: Membrane potential at the soma for $nm^{Cl}=1$ and $nm_{soma}=2$. The green graph states the transmembrane voltage of the neuron and the blue one that with a ensheathing cluster for different sizes of the cluster.

In this simulation two surprising results occur. On the one hand not only the strength of the AP is increased also the excitation process gathers velocity, e.g., the peak of the membrane potential occurs about 0.19ms earlier for the cluster of the same size as the neuron compared to the peak of the single neuron. It is observed that this increase in velocity decreases with ongoing enlargement of the cluster.

Although the first effect resembles a positive influence the second result of this simulation on the other hand is that if the cluster is of the doubled size the cluster fails to excite the soma region which remains to be investigated. Nevertheless it should be mentioned that the blue graphs for the compartments which precede the normally nonmyelinated soma region excite the neuron similarly to the green one with a small increase in strength but not in velocity, i.e., the excitation with an enlargement of 100% fails not before the soma region.

The maximum value of V_m for the green graph, i.e., in the absence of a cluster is 90.478mV . Similar to the first simulation the cluster increases the strength of the

4.3 Cluster - First Results and Consequences

AP, e.g., for 0% and 1% enlargement of the cluster the peaks reach values of about approximately 100 mV . Even for a 50% enlargement the AP is marginally faster and the maximum value is 92.414 mV resembling a slightly increase of about 2 mV .

The third simulation has been done for a single layer of myelin remaining for the cluster and three sheets of myelin for the cochlear neuron. Due to the increase of the myelin layers at the neuron the excitation is successful as well similarly to the second simulation with an increased peak of the AP.

Fig. 4.11 provides the results for this simulation with an enlarged grid to account for the increased maximum values compared to the previous simulation.

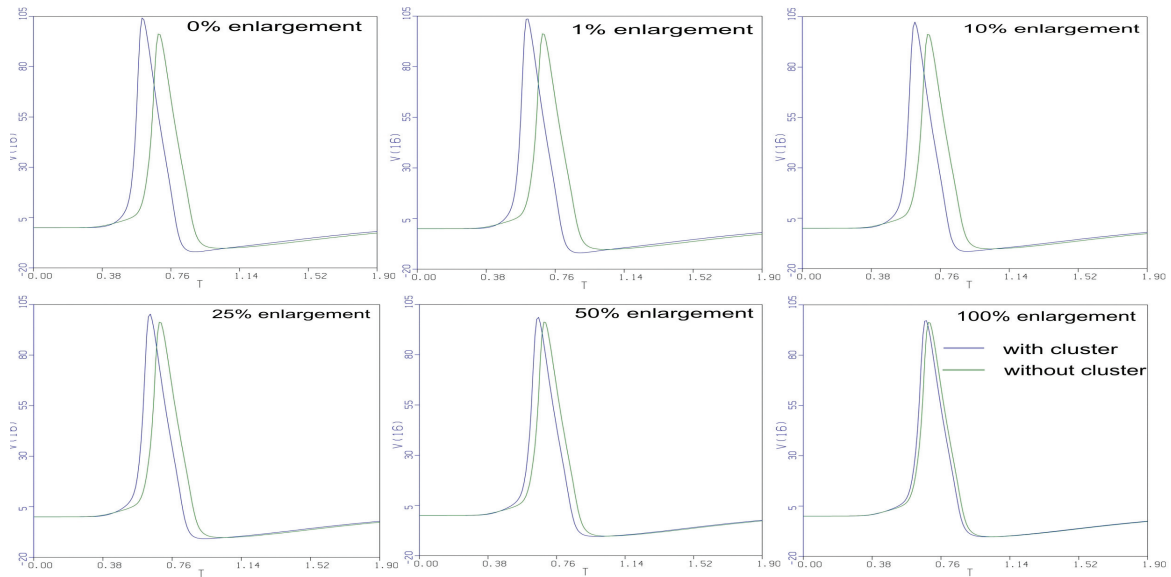


Figure 4.11: Membrane potential at the soma for $nm^{Cl}=1$ and $nm_{soma}=3$. The green graph states the transmembrane voltage of the neuron and the blue one that with a ensheathing cluster for different sizes of the cluster.

The maximum value of the membrane potential V_m of the soma compartment for the absence of a cluster is 96.253 mV and therefore an increase of about 6 mV compared to the peak of V_m with only two layers of myelin. An increase in velocity and strength is now observed for all sizes of the cluster.

For example, for a cluster of the same size as the neuron the peak is reached about 0.1 ms earlier and its corresponding maximum value is 7.9225 mV larger which is an increase in strength of about 8.23% . Note that for only two layers of myelin and a corresponding size of the cluster the velocity is more increased, also the strength undergoes a higher growth of 11.68% . Therefore it is believed that with an increasing safety factor of the neuron itself, e.g., more layers of myelin, the cluster becomes

4.3 Cluster - First Results and Consequences

less important, i.e., the influence and resulting improvement of the spiking behavior decrease.

In this simulation the velocity and strength of the cluster also decreases with increasing size, but the excitation does not fail for the double sized cluster. The maximum value for a 100% enlargement is 97.158 mV and therefore represents also a slightly growth in strength although the influence is very small which can as well be observed in the nearly simultaneous peaks of the green and the blue graphs.

The following simulation has been performed for two layers of myelin for the cluster and only one sheet enclosing the neuron's soma region. In this case the AP still fails to overcome the normally nonmyelinated soma region as in the first simulation. The increase of the safety factor of the cluster therefore does not lead to a predicted positive influence of the spiking behavior of the neuron. Moreover it turns out that with an altering amount of myelin layers for the cluster with only one sheet at the neuron the excitation is increasingly hindered as will be revealed in the following.

The results of the simulation for two layers of the cluster and one for the neuron are presented in Fig. 4.12.

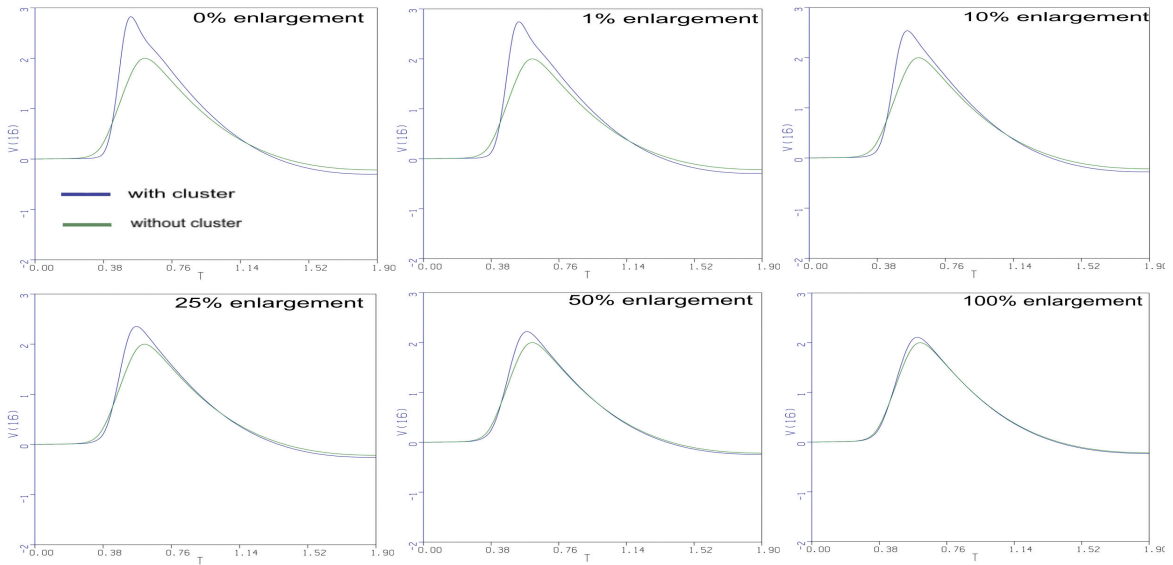


Figure 4.12: Membrane potential at the soma for $nm^{Cl}=2$ and $nm_{soma}=1$. The green graph states the transmembrane voltage of the neuron and the blue one that with an ensheathing cluster for different sizes of the cluster.

The maximum value of V_m without a cluster naturally remains the same, i.e., 1.9997 mV for the soma compartment, but the peak of the unaltered cluster is decreased compared to the case with only one sheet of myelin with a maximum value of

4.3 Cluster - First Results and Consequences

2.8261 mV . This means a much lower increase of strength of only 42.32% of the AP without a cluster.

Still the decrease of the influence of the cluster with increasing size can be observed. If the cluster has the doubled diameters there is only a small difference in the peaks of the membrane potential concerning the amount of myelin layers around the cluster, i.e., the maximum value for two layers is slightly decreased to 2.108 mV .

In this nonpropagating case no markable increase in velocity is present no matter of the size of the cluster.

The next simulation has been done for three layers of myelin around the cluster and still one remaining for the neuron. As mentioned before the excitation process fails at the soma region and in this case the positive influence of the cluster even more decreases compared to two layers of myelin.

The results for the membrane potential at the soma are presented in Fig. 4.13. These results reveal the decreasing maximum values compared to the previous simulation. Although the strength is still stronger for the unaltered cluster and decreases with increasing size, the differences are rather insignificant.

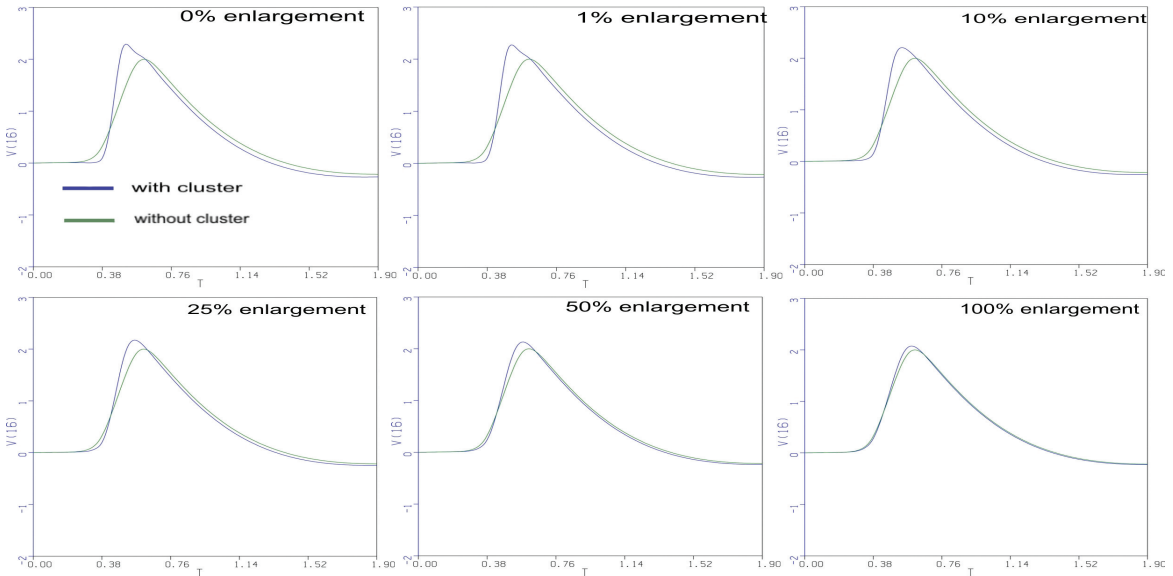


Figure 4.13: Membrane potential at the soma for $nm^{Cl}=3$ and $nm_{soma}=1$. The green graph states the transmembrane voltage of the neuron and the blue one that with an ensheathing cluster for different sizes of the cluster.

For example, the maximum value for 0% enlargement of the cluster is 2.2911 mV which represents only a 14.57% increase of the standard maximum value of 1.9997 mV for the excitation at the soma without a cluster and one layer of myelin.

4.3 Cluster - First Results and Consequences

The difference in the peak for the double sized cluster concerning the number of myelin layers remains insignificant, with a value of 2.0756 mV which is only a slightly decrease compared to those for one or two layers.

The velocity pattern stays the same for varying amount of myelin sheets, i.e., the membrane potential is only slightly faster with an unaltered cluster and nearly simultaneously for a double sized one.

The most surprising results were obtained by the subsequent simulation performed for two layers of myelin for the cluster and the neuron itself. In this case the AP succeeds to overcome the soma region in the absence of the cluster but fails in its presence no matter of the size of the cluster.

Until the first compartment of the cluster the excitation pattern is quite similar for the cluster and the single neuron and this pattern also rather depends on the size of the cluster. Therefore the membrane potential as a function of time is shown for the last peripheral internode and the soma compartment for the 1% and the 50% enlarged clusters in Fig. 4.14.

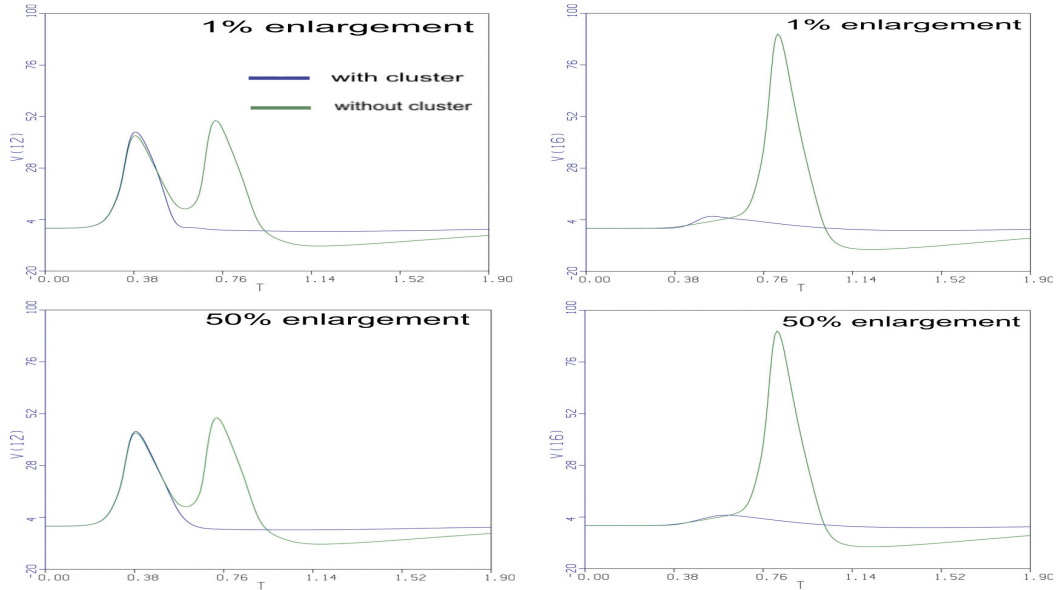


Figure 4.14: Membrane potential at the soma for $nm^{Cl}=2$ and $nm_{soma}=2$. The green graph states the transmembrane voltage of the neuron and the blue one that with an ensheathing cluster for different sizes of the cluster.

Although the first peak of the 1% enlarged cluster is slightly larger at the last internode than that of the single neuron the AP fails to overcome the soma region. The maximum value at the soma for the cluster is only 5.6637 mV whereas without the cluster this value is 90.478 mV as already determined.

4.3 Cluster - First Results and Consequences

The strength even continues to decrease for increasing size of the cluster, e.g., the maximum value of V_m at the soma for the 50% enlarged cluster is only 4.8724 mV. At the last internode the first rising and falling phase of the AP from the cluster is in this case nearly identical to those of the single neuron.

This behavior might be explained by the decrease of the safety factor when the number of myelin layers of the cluster is increased as mentioned before but nevertheless remains to be investigated in further experiments.

To sum up these results it is observed that the presence of a cluster supports the spiking behavior in most cases with an increased velocity and especially strength of the AP. This positive development decreases with an increased size of the cluster which certainly results from the reduced influence of the cluster when it is moved away from the neuron.

Although it seems that the safety factor of the whole excitation process is decreased with the presence of a cluster, only in the case of two myelin sheets for the cluster and the neuron the presence of a cluster totally breaks down the excitation of the neuron which remains to be investigated precisely.

The maximum values, i.e., the peaks of the membrane potential V_m at the soma compartment are listed in Table 4.6.

enlargement	V_{max} at the soma					
	$nm^{Cl} = 1$	$nm^{Cl} = 1$	$nm^{Cl} = 1$	$nm^{Cl} = 2$	$nm^{Cl} = 3$	$nm^{Cl} = 2$
	$nm_s = 1$	$nm_s = 2$	$nm_s = 3$	$nm_s = 1$	$nm_s = 1$	$nm_s = 2$
0%	4.85783	101.05	104.175	2.8261	2.29119	5.66366
1%	4.6496	100.451	103.597	2.73986	2.27211	5.59723
10%	3.57185	98.3215	102.385	2.53823	2.20579	5.20668
25%	2.88411	95.4284	100.325	2.35378	2.174	4.97635
50%	2.46074	92.4139	98.6265	2.22013	2.13139	4.87243
100%	2.19621	7.86326	97.158	2.10807	2.07559	4.92068
nocluster	1.99973	90.4777	96.2525	1.99973	1.99973	90.4777

Table 4.6: Maximum values of the membrane potential V_{max} at the soma for different grades of myelination of the neuron and the cluster. nm_s abbreviates nm_{soma} . Peaks are shown for increasing size of the cluster and also for the theoretical case of a single neuron (values in mV).

The actual appearance and the peaks of the simulated membrane potential of the cluster V^{Cl} certainly change in different cases depending on the geometrical and electrical parameters, especially the numbers of myelin layers, and as well on the number of neurons involved. However to give a first impression some results are shown in Fig. 4.15 which displays the membrane potential for four of five cluster compartments with altering size of the cluster. One sheet of myelin surrounds the

4.3 Cluster - First Results and Consequences

cluster and three layers support the theoretical case of a single neuron. For the stimulus strength the standard value of $0.0005 \mu A$ is chosen.

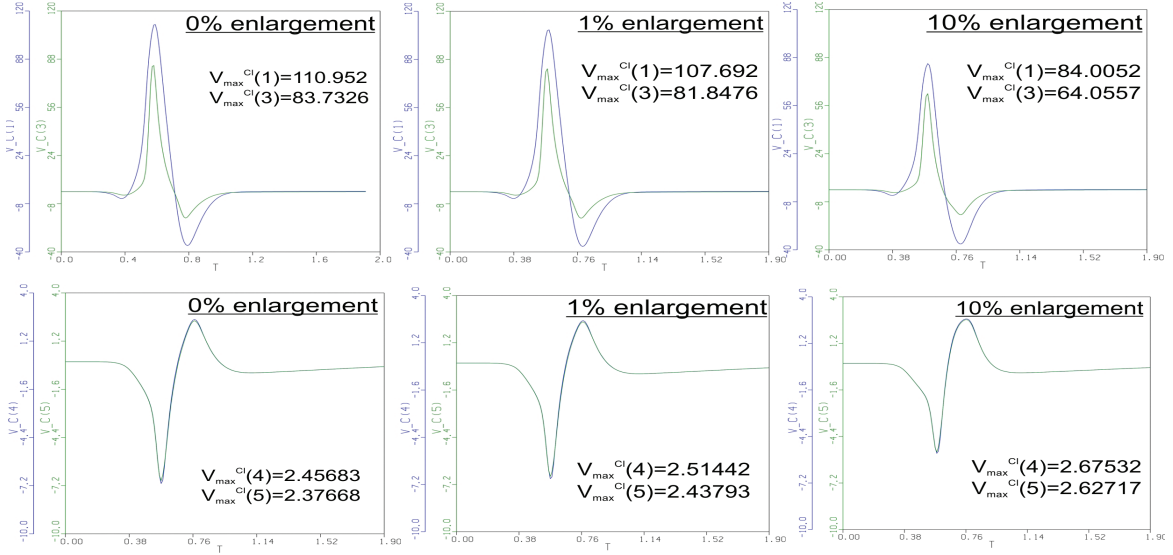


Figure 4.15: Membrane potentials of the single neuron cluster at the first and third presomatic compartment at the top and those of the soma and the presomatic region at the bottom which appear to be nearly identical. Three different sizes of the cluster are tested and the corresponding maximum values are also provided (values in mV).

It is obvious that the potential of the presomatic compartments $V^{Cl}(1)$ and $V^{Cl}(3)$ resemble that of the neuron itself especially for the unaltered cluster. With increasing size of the cluster the peaks decrease which might be a result of the shrinking influence of the neuron. The maximum values for the six cases of enlargement are summarized in Table 4.7.

The membrane potentials of the cluster at the soma compartment and afterwards, i.e., $V^{Cl}(4)$ and $V^{Cl}(5)$ certainly change which can be observed at the bottom of Fig. 4.15. This special appearance of the potential resembles somehow the form of extracellular potential which were studied and simulated by Gold et al. (2006) for different sites along neurons. Moreover the ranges and the form of the potential of the cluster appears to be similar to the findings of FitzGerald et al. (2008) for the extracellular voltage.

Although this surprising behavior remains to be investigated in detail and many questions persist, the maximum values for this special case are summarized in the following table to give an impression of the significant changes in those peaks.

V_{max}^{Cl} for $nm^{Cl} = 1$ and $nm_{soma} = 3$					
enlargement	$V_{max}^{Cl}(1)$	$V_{max}^{Cl}(2)$	$V_{max}^{Cl}(3)$	$V_{max}^{Cl}(4)$	$V_{max}^{Cl}(5)$
0%	110.952	109.799	83.7326	2.45683	2.37668
1%	107.692	106.505	81.8476	2.51442	2.43793
10%	84.0052	83.2799	64.0557	2.67532	2.62717
25%	59.7953	59.247	64.0557	2.55106	2.51155
50%	38.5341	38.1377	29.3677	2.19931	2.16761
100%	20.6748	20.3526	15.2505	1.58513	1.56827

Table 4.7: Maximum values of the membrane potential V_{max}^{Cl} for all compartments with different sizes of the cluster (values in mV). Note that the values for the presomatic compartments decrease whereas the values for the soma and the postsomatic compartment initially increase until the cluster gets to big and the influence of the neuron vanishes.

4.4 Multiple Neuron Cluster - New Approach

In this section the first results of the predicted mathematical model concerning the interaction between neurons within one cluster are presented. These investigations should give a first insight to the ability of humans when it comes to complex coding of hearing perception. It should be clarified whether the cochlear neurons of the same cluster have a strong influence on each other or if this surrounding sheet does not lead to the expected communication of these nerve cells.

The investigations for two neurons and a comparison to a single neuron with a soma ensheathing cluster are given in Section 4.4.1. The results for three neurons are provided in Section 4.4.2. Due to the findings of *Tylstedt et al. (1997)* who reported up to four neurons sharing one cluster the results for this amount of nerve cells is represented in Section 4.4.3.

4.4.1 2 Neuron Cluster

As mentioned previously the cluster is as well cylindrically approximated in the case of two nerve cells sharing the same sheet of the surrounding cluster. The two enclosed neurons are predicted to have the same size and shape, i.e., the nerve cells have similar geometrical and electrical properties. Spatially one neuron lies on top of the other one with a certain distance at the soma which was chosen $5\mu m$ (Fig. 4.16). Therefore all compartments of the two nerve cells show the same spatial positions.

The cluster is chosen to directly face the cell bodies and peripheral and central processes in the subsequent simulations leading to the diameters which are presented in Table 4.8, i.e., no additional enlargement of the cluster is predicted.

Note that for the whole section and all subsequent simulations one layer of myelin is chosen for the cluster and three sheets for every neuron.

4.4 Multiple Neuron Cluster - New Approach

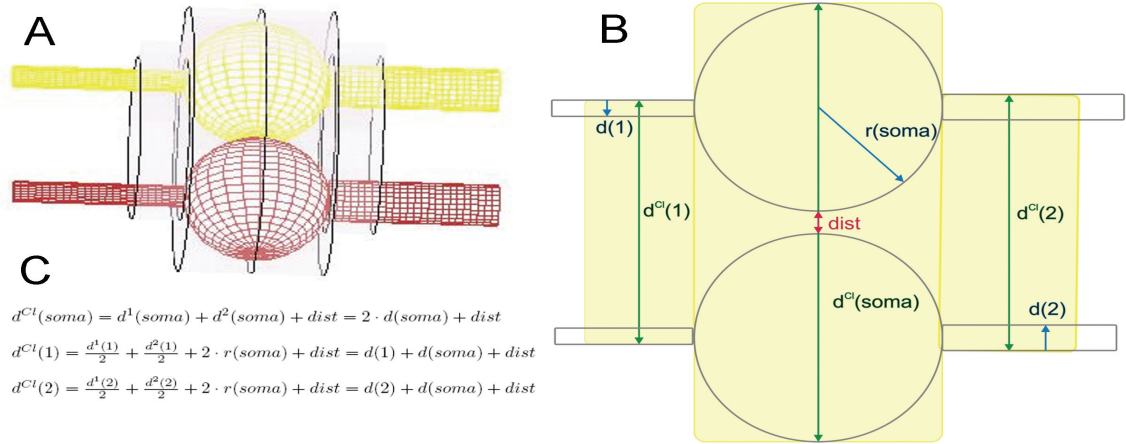


Figure 4.16: (A) Spatial arrangement of the neurons sharing one cluster (grey). (B) Assumed distance and absence of additional enlargement of the cluster at the soma region. (C) Equations for the resulting diameters of the cluster compartments (values in Table 4.8).

Diameters for the two neuron cluster			
	peripheral	soma	central
neurons	0.0001	0.003	0.0002
cluster	0.0036	0.0065	0.0037

Table 4.8: Table of the geometry of the human cluster for two cochlear neurons according to Fig. 4.16 (values in *cm*).

The first simulations have been performed to investigate the differences in the spiking behavior of the two neurons in contrast to one single neuron with a cluster ensheathing the soma region. Moreover it should be clarified if the second neuron could be triggered to produce an AP under subthreshold conditions when it is supported by the properly stimulated other neuron. Therefore simulations have to be performed for varying stimuli strengths and onsets.

To investigate these varying cases a program has been implemented in ACSL with separately controllable stimuli for the two neurons and also for three and four nerve cells in the following.

First of all, differences concerning the spiking behavior of two neurons which are stimulated by the same impulse, i.e., the same strength and onset, as one single cluster-ensheathed neuron were observed. It turned out that the AP of the single neuron at the soma compartment shows a higher peak than the membrane potential at the perikaryon of one of the two identically excited neurons. For example, when stimulated with an impulse with the standard value of $0.0005 \mu A$ the single neuron

4.4 Multiple Neuron Cluster - New Approach

with a unaltered cluster has a maximum value of 104.175 mV at the soma whereas the corresponding value for the two neurons is 96.187 mV . Even if the cluster is enlarged, meaning a reduced strength of the AP as mentioned previously, the peak of the membrane potential V_m is higher, e.g., 98.627 mV for a 50% enlargement of the cluster.

Varying strength of the stimuli showed the same trends, i.e., the single neuron is stronger stimulated than two neurons. This can also be observed for three or four neurons sharing the same cluster. The results are summarized in Table 4.11 at the end of this section. Note that these simulations for varying impulse strengths show that the standard value for the stimulus does not lead to the strongest excitation, but the differences occur to be small.

To give a first impression of the results obtained by these ACSL simulations for multiple neuronclusters Fig. 4.17 shows the membrane potentials V_m^1 of the first neuron at the soma represented by the blue graph and V_m^2 , that of the second one, characterized by the green graph.

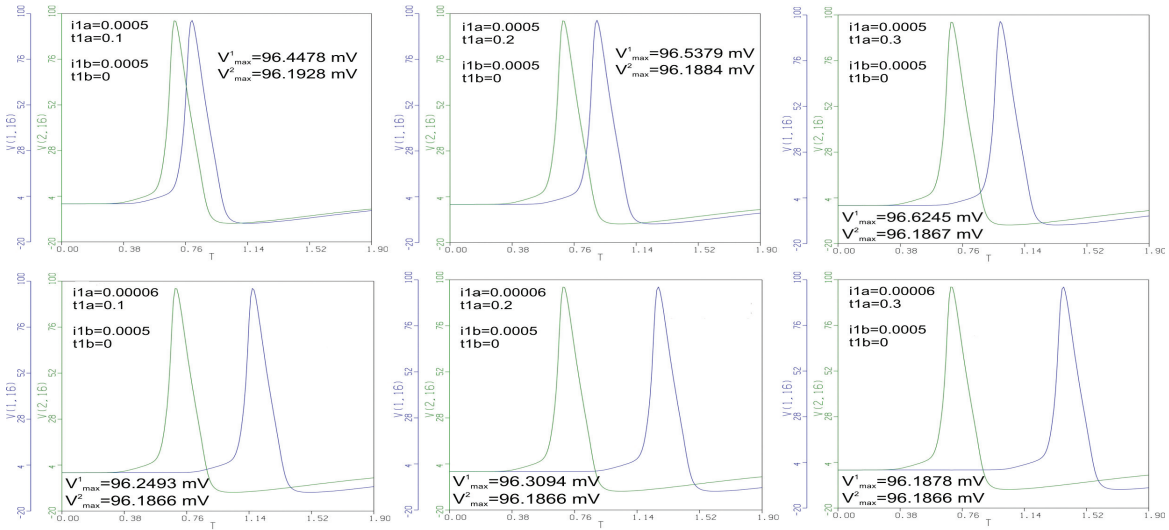


Figure 4.17: Membrane potentials of two neurons cluster with varying stimuli onsets and strengths at the soma compartment. The blue graph represents the first neuron, the green one the second. The varying onsets, $t1a$ and $t1b$ (in ms), and strength, $i1a$ and $i1b$ (in μA), of the stimuli are listed in the subframes. Maximum values are denoted by V_{max}^1 and V_{max}^2 .

The small changes in the maximum values show that first of all the reduction of the stimulus strength not only makes the excitation weaker it also causes a delay

which can be observed at the blue graph by direct comparison of the subframes which lie on top of each other.

With these results an interaction between the two neurons can also be expected since the maximum values of the second neuron also slightly change although its stimulus parameters, i.e., the onset time and the strength, remain the same. This can as well be observed by the maximum values of the first neuron which differ when the onset is changed what might be a result of the influence of the companion second neuron.

The maximum values under subthreshold conditions, i.e., when the stimulus is less than $0.00006 \mu A$ and the propagation of the AP fails, are slightly higher for the multiple neuron cluster than those of the single enclosed neuron, in contrast to the mentioned results for a stronger transthreshold impulse. For example, the maximum value for the single neuron with an unaltered cluster for a $0.00005 \mu A$ stimulus is $0.034681 mV$ whereas that of one of the two neurons is $0.036233 mV$.

Moreover it occurs at a stimulus strength of $0.00005 \mu A$ that the differences between a single neuron and a multiple neuron cluster and also the influence of the neurons on each other are best examined. Therefore a simulation has been done for one neuron stimulated under these subthreshold conditions and its properly excited companion one. The results for the membrane potential at the soma are shown in Fig. 4.18.

With these results it is obvious that the neurons which share the same myelin layer at their soma regions definitely interact with each other, because the second rising phase is only present for the two neuron cluster.

Of course the influence of the first neuron which is properly excited is increased for the same onset of the two stimuli. Therefore the peak of the membrane potential of the second neuron is highest for the case in the top right.

Nevertheless it is obvious that the firing first neuron is not able to trigger the AP of the second neuron under subthreshold condition to overcome the soma region.

4.4.2 3 Neuron Cluster

For the following simulations the geometry of the cluster for three enclosed cochlear neurons is predicted to be resemblant to that of two nerve cells, i.e., an additional enlargement of the cluster is avoided and the three neurons are similar spatially arranged. The calculation of the diameters is the same as for the four neuron cluster and therefore presented in Section 4.4.3. Note that slightly smaller diameters could have been possible if the third neuron is shifted to the middle.

As well as for two neurons a certain distance between the perikarya is predicted. The diameters which result from the neuronal arrangement are given in Table 4.9.

As mentioned before the peaks for the multiple neuron clusters are smaller than for the single enclosed neuron with identical transthreshold stimuli. For example, for the three neuron cluster the maximum value for a simultaneous stimulation of all three neurons at the standard strength of the stimuli of $0.0005 \mu A$ is $96.198 mV$ which is

4.4 Multiple Neuron Cluster - New Approach

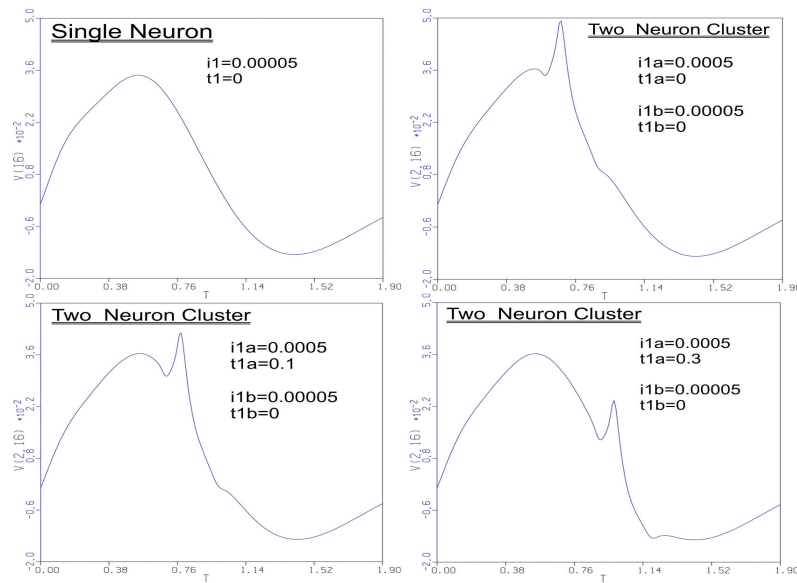


Figure 4.18: Membrane potentials under subthreshold condition for a single neuron at the soma compartment at the top left. Results for the second neuron of a two neuron cluster with varying onset of the stimulus of the first neuron are also provided. The varying onsets, t_1 for the single neuron, t_{1a} and t_{1b} for the two neuron cluster (in ms), and strength, i_1 , i_{1a} and i_{1b} (in μA), of the stimuli are listed in the subframes.

Diameters for the three neuron cluster			
	peripheral	soma	central
neurons	0.0001	0.003	0.0002
cluster	0.00505	0.00795	0.00515

Table 4.9: Table of the geometry of the human cluster for three cochlear neurons (values in cm).

only marginally higher than that of the two neuron cluster.

In comparison with the results in Fig. 4.17, a similar simulation has been done for the three neuron cluster. Fig. 4.19 shows the outcome of this simulation for the membrane potential at the soma compartment. Only two graphs are seen because the stimuli of the second and third neuron are chosen identically and therefore the third red graph domineers the green one of the second neuron.

These results correspond with those of the two neuron cluster. All maximum values of the second and third neurons are higher than those of the corresponding second neuron in the previous section which reflects their positive influence on each other.

4.4 Multiple Neuron Cluster - New Approach

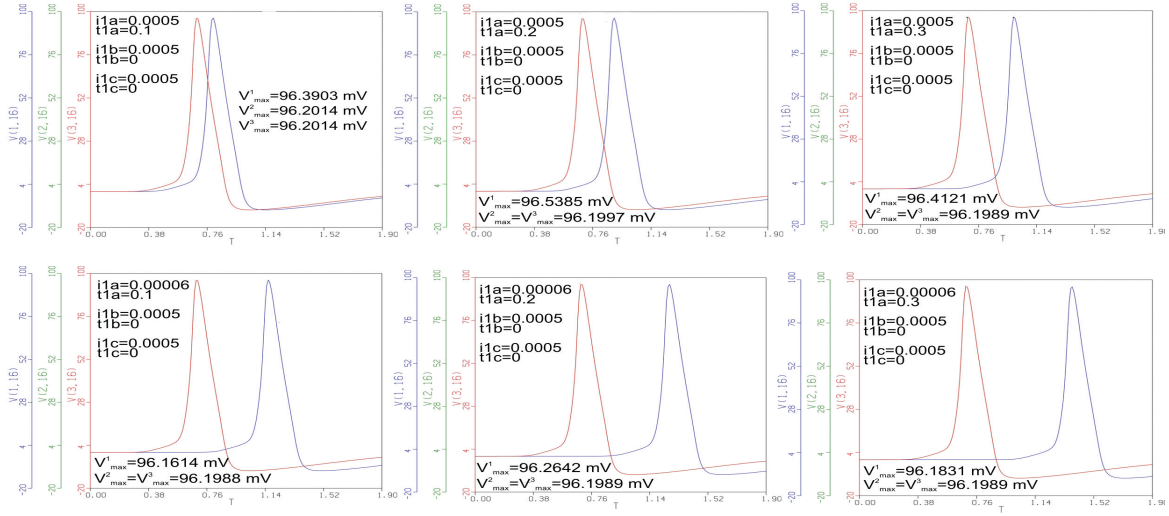


Figure 4.19: Membrane potentials in a three neuron cluster with varying stimuli onsets and strengths at the soma compartments. The blue graph represents the first neuron, the red one the third which dominates the green graph of the second neuron since their stimuli are identical. The varying onsets, t_{1a} , t_{1b} and t_{1c} (in ms), and strength, i_{1a} , i_{1b} and i_{1c} (in μA), of the stimuli are listed in the subframes. Maximum values are denoted by V_{max}^1 , V_{max}^2 and V_{max}^3 .

However, the peaks of excitation of the first neuron are decreased, e.g., the maximum value of 96.412 mV for the top right picture and the corresponding value of 96.625 mV in the Fig. 4.17. It can be expected that the positive influence of the second neuron on the third might probably decrease the effect on the first.

The maximum values under subthreshold conditions increase negligibly in comparison with the two neuron cluster and therefore they are also higher than those of the single nerve cell with a supporting cluster. Nevertheless the influence of two neurons which are properly excited on a third one, which fails to produce an AP at the soma, is increased as presented in Fig. 4.20.

Clearly the positive effect of the two excited neurons is not able to trigger the third one to fire under subthreshold conditions. The three subframes on the bottom demonstrate that the onsets of the stimuli play an important role when it comes to excitation. Even if two neurons are simultaneously stimulated the onset of the weak third impulse significantly needs to be close.

Nevertheless there might be evidence of complex coding in the human cochlea underlined by the following simulations. These investigations are shown in Fig. 4.21 where different onsets and strengths of the three stimuli are tested.

4.4 Multiple Neuron Cluster - New Approach

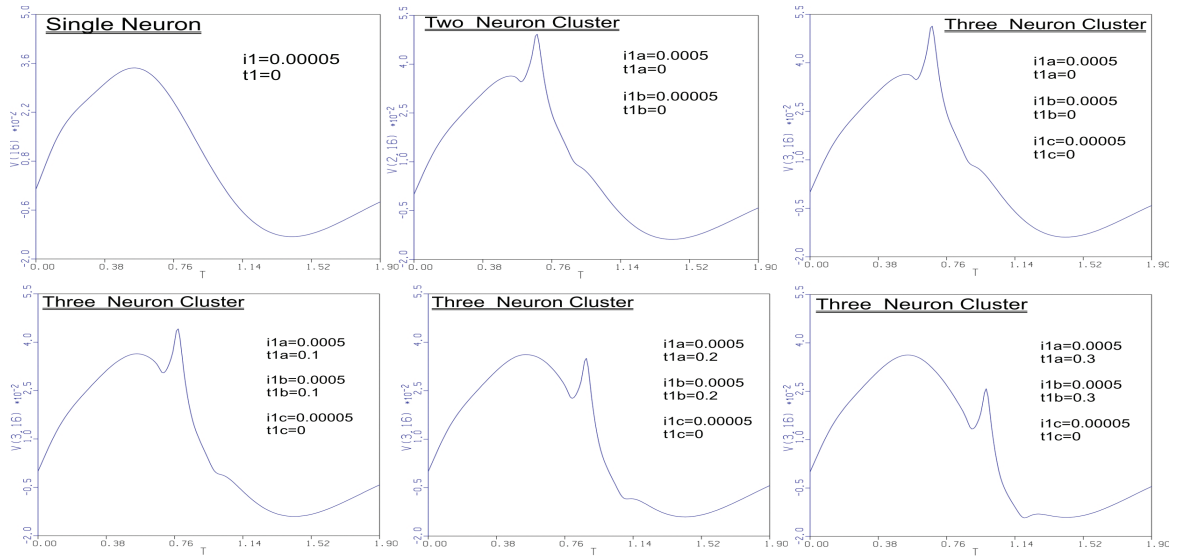


Figure 4.20: Membrane potentials under subthreshold condition for a single neuron at the soma compartment at the top left and for the two neuron cluster at the top middle. Results for the third neuron of a three neuron cluster with varying onset of the identical stimulus of the first and second neuron are also provided.

The interaction of neurons which share the same cluster is evidently displayed. In the left upper subframe (Fig. 4.21) the maximum value of the third neuron is the highest which might be a result of the positive effect of the first two. Note the different ranges for the other subframes where the third neuron fails to propagate the AP over the soma region. Nevertheless the varying influence of the other two neurons is obvious when the stimuli onsets are changed. The highest maximum voltage for the third neuron of 0.041612 mV occurs when its own stimulus onset is at $t1c = 0$ which is a result of the more steeply first rising phase of its membrane potential V_m^3 and the following effect of the first and second neuron.

4.4.3 4 Neuron Cluster

The geometry of the four neuron cluster also follows the same pattern as those of the other multiple neuron clusters. The four neurons are spatially arranged in the same way so that the corresponding compartments of two neurons are next to each other and the other two lie on top of them (Fig. 4.22).

The topology of this four neuron cluster is illustrated in Fig. 4.22 and the calculation of the diameters of the cluster with identical diameters of all compartments of the neurons is obvious. The chosen distance between the neurons is $5\mu\text{m}$ according to that of the two neuron cluster and therefore the values for the diameters can be

4.4 Multiple Neuron Cluster - New Approach

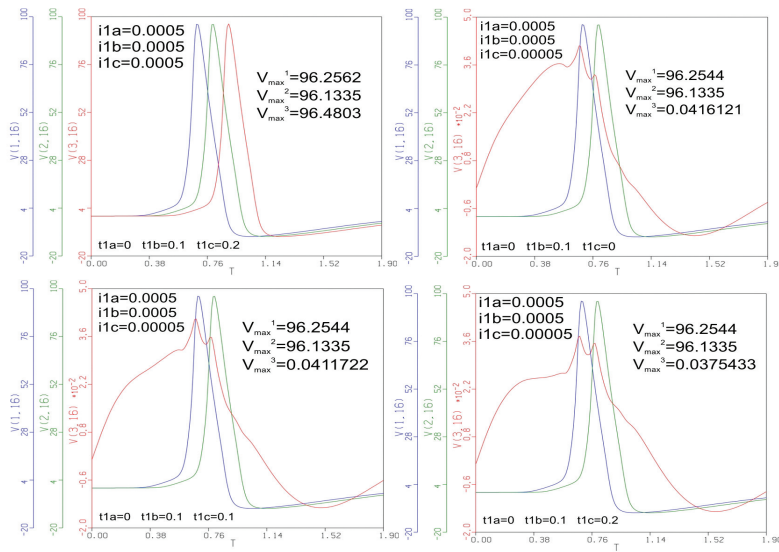


Figure 4.21: Membrane potentials of a three neurons cluster with varying stimuli onsets and strengths at the soma compartment. The blue graph represents the first neuron, the green graph demonstrates the second neuron and the red one the third.

found in Table 4.10 which are the same as for the three neuron cluster.

Diameters for the four neuron cluster			
	peripheral	soma	central
neurons	0.0001	0.003	0.0002
cluster	0.00505	0.00795	0.00515

Table 4.10: Table of the geometry of the human cluster for four cochlear neurons (values in cm).

If all four neurons are stimulated simultaneously with a strength of $0.0005 \mu A$ at P0 the maximum value for the membrane potentials at the perikarya is $96.179 mV$ what resembles a small decrease compared to the three and two neuron cluster.

The maximum values under simultaneous subthreshold conditions for all four neurons does not increase any longer compared to the three neuron cluster. The maximum values for different strengths of stimuli and the same onsets are now summarized for the single and multiple neuron cluster and represented in Table 4.11.

At this point it should be reminded that the maximum values for the membrane potentials at the soma compartment are not the highest for the standard value of impulse strength of $0.0005 \mu A$.

4.4 Multiple Neuron Cluster - New Approach

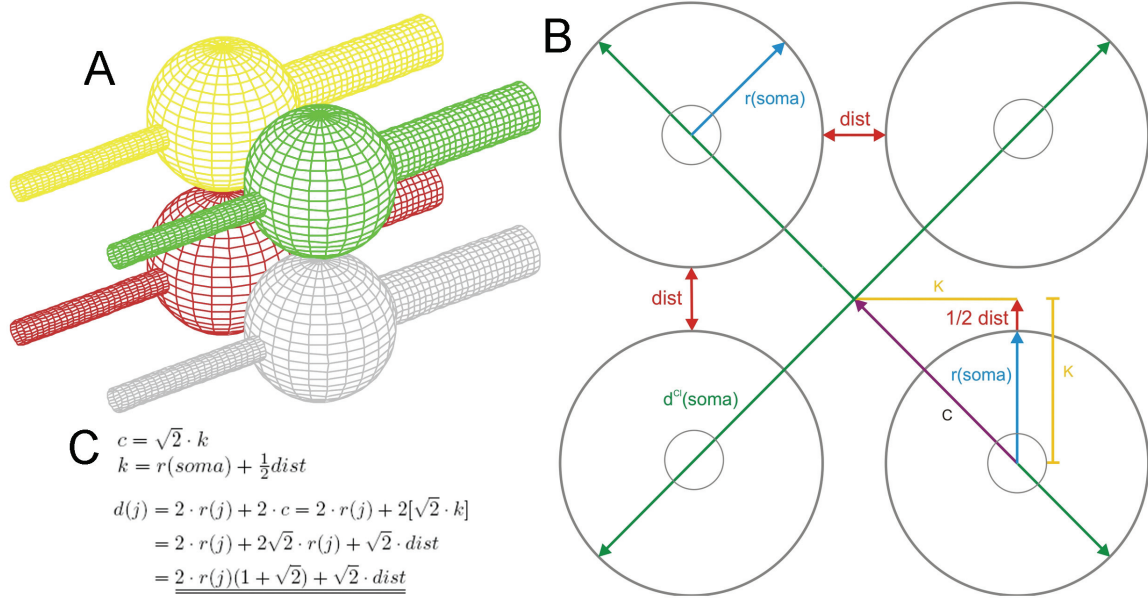


Figure 4.22: (A) Spatial arrangement of the neurons sharing one cluster. (B) Assumed distance and absence of additional enlargement of the cluster at the soma region. (C) Equations for the resulting diameters of the cluster compartments (Table 4.10).

In order to directly compare the results for the multiple neuron clusters Fig. 4.23 provides the equivalent to Fig. 4.17 and 4.19, i.e., the membrane potentials at the soma compartment, with still only two graphs because the fourth neuron illustrated as purple has the identical impulse as the second and third.

The behavior of this experiment is alternating since the maximum values for the fourth to second neuron now are smaller than those of the second and third of the three neuron cluster with no exception no matter of the different stimuli parameters. These exclusive results for the maximum values for the four neuron cluster diverges from those of the three neuron cluster since some outliers in the values are present.

Furthermore the maximum value at the top left of 96.183 mV is even smaller than the corresponding value for the two neuron cluster of 96.193 mV .

On the other hand the maximum values for the first neuron definitely increase in most cases compared to the other multiple neuron clusters which also resembles the alternating behavior. For example, at the left bottom the maximum value for the first neuron in the two neuron cluster is 96.249 mV then the corresponding value for the three neuron cluster decreases to 98.161 mV and finally is the highest for the four neuron cluster with a value of 96.4482 mV . This is not very surprising because in this case even three other simultaneously stimulated neurons support only one.

If only one neuron receives a subthreshold stimulus and the other three are properly excited the maximum value of the fourth increases compared to the experiments for

4.4 Multiple Neuron Cluster - New Approach

V_{max} at the soma with $nm^{Cl}=1$, $nm_{soma}=3$						
i1=i1a	0.0005	0.0003	0.00025	0.0002	0.00006	0.00005
1.1	104.175	104.46	104.393	104.446	103.961	0.0346813
1.2	103.597	104.059	104.219	104.194	103.955	0.0347148
1.3	102.385	102.102	101.892	101.824	101.789	0.0349715
1.4	98.6265	98.4431	98.8047	98.6895	98.178	0.0355763
2.1.1	96.2541	96.5857	96.6435	96.6421	95.9207	0.0362329
2.1.2	0.0337463	0.032743	0.0327049	0.0321304	0.0249924	0.0249924
2.2.1-	96.187	96.5541	96.6403	96.6272	95.896	0.036233
2.2.2						
3.1.1-	96.2515	96.5849	96.6442	96.6422	95.9829	0.036234
3.1.2						
3.1.3	0.0358989	0.0349247	0.0349091	0.0343284	0.0249921	0.0249921
3.2.1-	96.1981	96.5587	97.8775	96.6291	95.954	0.036234
3.2.3						
4.1.1-	96.251	96.5862	96.6468	96.6443	96.9794	0.0362344
4.1.3						
4.1.4	0.0454739	0.0442165	0.0444087	0.043751	0.0309498	0.0249924
4.2.1 -	96.1791	96.551	96.6401	96.6255	95.8753	0.0362342
4.2.4						

Legends	
1.1: 1 neuron, 0%enlargement	2.1.1: 1st of 2 neurons, ilb=0
1.2: 1 neuron, 1%enlargement	2.1.2: 2nd of 2 neurons, ilb=0
1.3: 1 neuron, 10%enlargement	2.2.1: 1st of 2 neurons, ilb=i1a
1.4: 1 neuron, 50%enlargement	2.2.2: 2nd of 2 neurons, ilb=i1a
3.1.1: 1st of 3 neurons, ilc=0,ilb=i1a	4.1.1: 1st of 4 neurons, ild=0,ilc=ilb=i1a
3.1.2: 2nd of 3 neurons, ilc=0,ilb=i1a	4.1.2: 2nd of 4 neurons, ild=0,ilc=ilb=i1a
3.1.3: 3rd of 3 neurons, ilc=0,ilb=i1a	4.1.3: 3rd of 4 neurons, ild=0,ilc=ilb=i1a
3.2.1: 1st of 3 neurons, ilc=ilb=i1a	4.1.4: 4th of 4 neurons, ild=0,ilc=ilb=i1a
3.2.2: 2nd of 3 neurons, ilc=ilb=i1a	4.2.1: 1st of 4 neurons, ild=ilc=ilb=i1a
3.2.3: 3rd of 3 neurons, ilc=ilb=i1a	4.2.2: 2nd of 4 neurons, ild=ilc=ilb=i1a
	4.2.3: 3rd of 4 neurons, ild=ilc=ilb=i1a
	4.2.4: 4th of 4 neurons, ild=ilc=ilb=i1a

Table 4.11: Maximum values of the membrane potential V_{max} at the soma for different stimulus strengths i1 for the single neuron and i1a, i1b, i1c and i1d (in μA) for multiple neuron cluster. Maximum values in mV .

the single enclosed neuron and the other multiple neuron clusters. Nevertheless three firing neurons are still not able to trigger the fourth AP to overcome the soma region.

The results for the membrane potential at the soma compartment for the neuron under subthreshold conditions while the other are simultaneously stimulated with the

4.4 Multiple Neuron Cluster - New Approach

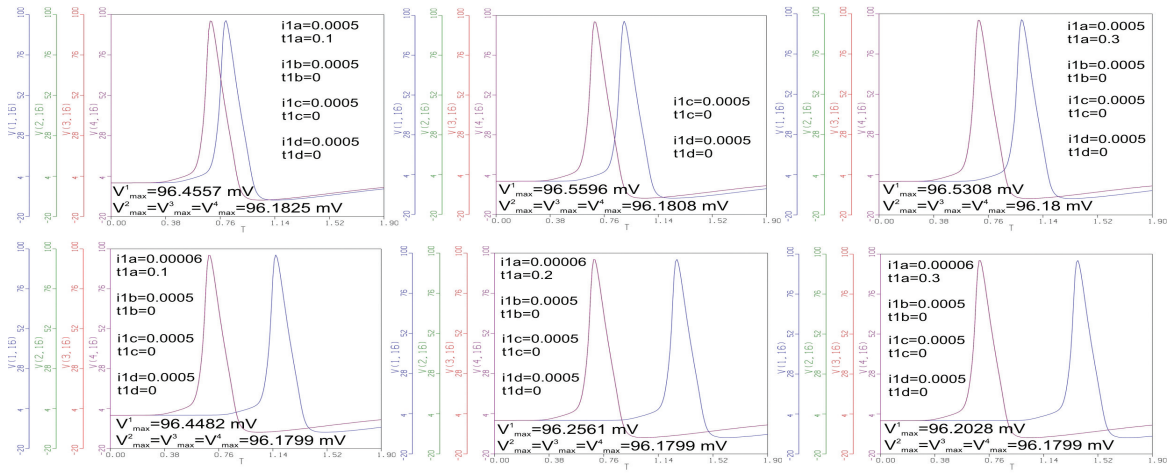


Figure 4.23: Membrane potentials of a four neuron cluster with varying stimuli onsets and strengths at the soma compartment. The blue graph represents the first neuron, the purple one the fourth which dominates the red and green graph of the third and second neuron since their stimuli are identical. The varying onsets, $t1a$, $t1b$, $t1c$ and $t1d$ (in ms), and strength, $i1a$, $i1b$, $i1c$ and $i1d$ (in μA), of the stimuli are listed in the subframes. Maximum values are denoted by V_{max}^1 , V_{max}^2 , V_{max}^3 and V_{max}^4 .

same strength are illustrated in Fig. 4.24. For direct comparison between the multiple neuron clusters all three results are drawn with the same grid.

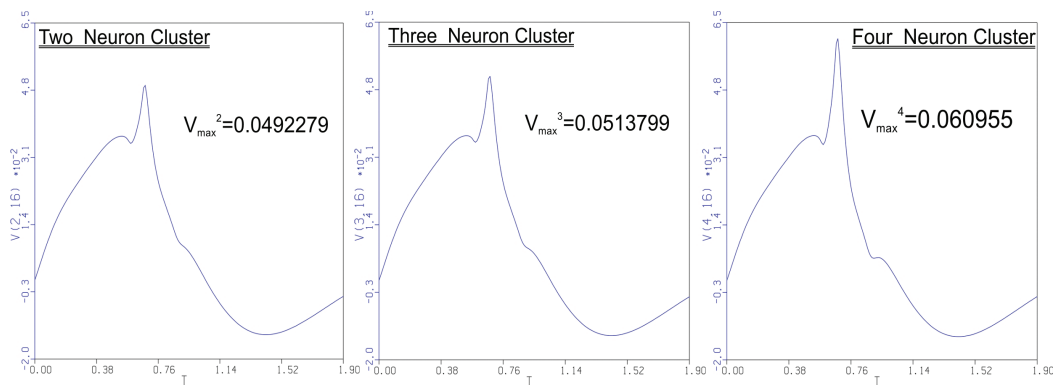


Figure 4.24: Membrane potentials under subthreshold condition for a two neuron cluster at the left and for the three neuron cluster in the middle. The result of the four neuron cluster is shown at the right.

4.4 Multiple Neuron Cluster - New Approach

The maximum value for the neuron which is not properly stimulated definitely increase which is not surprising since the number of positively effective neurons increases.

A better insight of the influence of the neurons on each other which are ensheathed by the same cluster is provided by Fig. 4.25 where the results for the membrane potential of all four neurons with varying onsets and strength of the stimuli are presented.

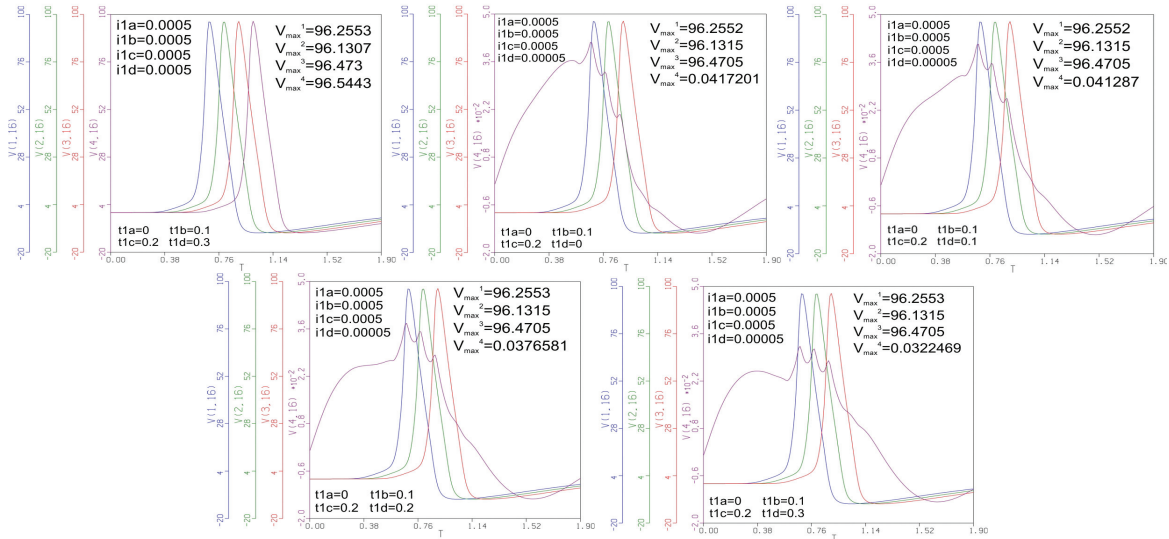


Figure 4.25: Membrane potentials of a four neuroncluster with varying stimuli onsets and strengths at the soma compartment. The blue graph represents the first neuron, the green graph demonstrates the second neuron and the red one the third. The fourth neuron correspond to the purple graph.

In the first subframe where all neurons are stimulated with the same impulse strength the second neuron shows the lowest peak which is similar to the three neuron cluster. The first one is slightly supported by the others while the third and especially the fourth are profiting from the excitation of the others.

Observing the other subframes with varying onset of the fourth neuron, which is now only stimulated with a subthreshold impulse of $0.00005 \mu A$, the different influences can be observed. The highest maximum value of $0.04072 mV$ of the fourth neuron appears at an initial onset which is represented on the top middle subframe. This is similar to the three neuron cluster and can be explained by the prominent first rising phase.

The maximum values decrease with increasing onset times. Nevertheless the influence of the other neurons is obvious.

4.4 Multiple Neuron Cluster - New Approach

To sum up these results of the first simulations with multiple neuron clusters one could expect that these neurons definitely effect each other, but a group of excited neurons are not able to produce an AP at an adjutant neuron under subthreshold conditions.

It should be noted that not all possible variations of electrical parameters, e.g., the number of myelin sheets, as well as geometrical parameters, especially the size of the cluster and the spatial position of the neurons, had been taken into account. Moreover further combination of stimuli parameters would have been possible.

These simulations therefore underlie certain limitations and it should be kept in mind that the obtained results were developed with an opening approach to the topic of complex coding in the human cochlea concerning the present neuron clusters especially in the apical regions of the cochlea. Therefore a conclusion of the restrictions of the mathematical model and the critical results is provided in the next section.

Chapter 5

Conclusion and Further Work

The results presented in the previous section obtained by computer simulation should be analyzed from a critical point of view since the mathematical model used in this thesis underlies some limitations. These restrictions and the chosen parameters of the model which only represent some special circumstances should be kept in mind while discussing the investigations.

Therefore this section should summarize the findings and point out the arising questions which remain to be answered in the future by examination of further tests, possible changes in the mathematical model and also comparison of results obtained by other authors.

With respect to the simulation work for the sensitive parameters of the nonmyelinated soma region it can be concluded that this human specialty plays an important role in the excitation behavior in the cochlea and is somewhat different from other mammals, e.g., like the cat in particular. Therefore special interest should be paid on this topic when it comes to cochlear implants which are designed for humans and can not be based on findings of animals since the geometrical and electrical parameters certainly change.

Moreover it should be noted that the difficulties for an AP to overcome the unmyelinated soma region results primary from the classification of the cochlear neurons which are typically bipolar neurons and therefore the propagating AP needs to travel along the whole neuron across the current consuming perikaryon. This might also indicate evidence of the human hearing organ to be capable of more complex coding through evolutionary development since the cochlear neurons are not, e.g., pseudounipolar (Section 2.2) where these problems would disappear.

First of all it should be reminded that all used models refer to a simplified geometry of cochlear neurons obtained by cylindrical and spherical compartments. Only one particular type of neuron concerning, e.g., the number of peripheral internodes and their lengths, was used. Consequently further tests with a different structure of neurons might as well be examined in the future.

Additionally further combinations of the variation of the distinct parameters could have been possible and, e.g., the diameter of the soma was not tested at all. Also the electrical parameters play an important role and have not been considered. Generally should be mentioned that, e.g., [McIntyre et al. \(2002\)](#) among other authors introduced a detailed axonal model and proposed a reduced myelin capacitance and decreased nodal and internodal resistance. Maybe subsequent ultrastructure studies of this special region of the cochlear neurons could result in a deeper insight and give rise to following experiments.

It should also be mentioned that only the HH model was used. Although the accelerated, warmed HH model was used for all compartments, further models should be investigated in the future like, e.g., the Sweeney model for the nodes used by [FitzGerald et al. \(2008\)](#) or the FH model as alternative to the HH model applied by [Cartee \(2006\)](#). [Smit et al.](#) also proposed adaptations to the HH equations to describe APs generated in the Ranvier node of a human sensory nerve fibre by, e.g., the introduction of temperature dependent resting potentials, resistances and capacitances.

Concluding the results for the human neuron cluster around the nonmyelinated soma region, it should be again pointed out that the knowledge about the physiology and electrical properties and therefore the influence of neuronal clusters is undesirable up to present time.

Many ideas for further experiments which occurred during the work of this thesis remain to be executed. The two main problems are on the one hand the decision on applicable parameters, i.e., the geometrical as well as electrical properties of the cluster as already mentioned above. On the other hand the description of the physical interaction between the cluster and the included neurons predicted by the mathematical model might be modulated for further tests. Nevertheless the results in this thesis demonstrated a strong interaction between neurons bounded together through a cluster.

Furthermore it should be mentioned that current fluctuations represented by the term I_{noise} were omitted for the simulations in this thesis. This certainly needs to be adapted for future simulations since single fiber recordings show variations in the firing latencies even when stimulated with constant intensity. Some fibers have a larger spread in the latencies than others. With the current fluctuations term (4.1) these revealed differences in the spiking behavior can be explained as described in more detail in [Rattay et al. \(2001a\)](#).

One of the most important restrictions of the model, concerning the electrical parameters of the cluster, is the axial resistance. In this thesis the resistance of the n-th cluster compartment R_n^{Cl} to its neighbours is calculated similarly to those of the cylindrical compartments of the neuron, i.e., $\frac{R_n^{Cl}}{2} = \frac{2\rho_i l_n^{Cl}}{(d_n^{Cl})^2 \pi}$ holds. This assumption is highly hypothetical since it is unclear which specific resistivity is present inside

the cluster which might as well be the extracellular resistivity of $\rho_e = 0.3 \text{ k}\Omega \text{ cm}$. Thus the simulations for the theoretical case of one single neuron cluster concerning the sensitive parameters around the soma region have been repeated for the following calculation of the resistance of the cluster

$$\frac{R_n^{Cl}}{2} = \frac{2\rho_e l_n^{Cl}}{(d_n^{Cl})^2 \pi}. \quad (5.1)$$

The results were quite similar to those obtained with the intracellular resistivity ρ_i . Nevertheless the sensitive parameters showed small variations compared to the calculation used in this thesis, e.g., the propagation at the soma was possible for a length of the last peripheral internode up to $li(6) = 0.036 \text{ cm}$ for a double sized cluster. Although this value is similar to that in the absence of a cluster, all the other parameter ranges necessary for a proper excitation are decreased. Nevertheless some parameter ranges increased, e.g., the variation of the intracellular resistivity ρ_i . Considering that this different resistivity did not show significant changes and even restricted the simulations concerning the size of the cluster, this assumption for the resistance of the cluster can be abolished.

A further supposition could be that one needs to subtract the resistance of the internal neurons. These idea leads to the following equation for the theoretical case of one single neuron enclosed by a cluster.

$$\frac{R_n^{Cl}}{2} = \frac{2\rho_e l_n^{Cl}}{(d_n^{Cl})^2 \pi} - \frac{R_n}{2} \quad (5.2)$$

where $\frac{R_n}{2}$ denotes the resistance of the corresponding n-th compartment of the neuron. Although the new assumption seems the most realistic, the ranges for the sensitive parameters deteriorate compared to the previous calculation and are nearly the same as for the original equation used in this thesis. Some ranges improved, e.g., that of the amount of myelin layers surrounding the soma of the neuron whereas other decreased like the range of the possible values of the intracellular resistivity.

However some simulations for the theoretical case of a single neuron and the new calculation have been repeated to compare the results. The spiking behavior of a cluster supported neuron generally remained the same, i.e., the propagation of an AP is faster and also stronger. The difference occurred in the maximum values where the new calculation offered slightly higher peaks compared to the original values.

Additionally the most important change can be observed in the surprising case of two layers of myelin for the cluster and the neuron itself (Fig. 4.14). As reported in Section 4.3.2 this is the only case where the cluster fails and the neuron itself is properly excited. With the new calculation this exceptional case vanishes and the performance of the cluster remains the same, i.e., an accelerated and strengthened AP at the soma compartment.

Therefore this new calculation of the axial resistance seems to describe the influence of a soma ensheathing cluster in a desirable way and should be used for further

simulations. More detailed SEM and TEM studies are expected to enlighten this topic and clarify the possibilities to model the electrical parameters, especially this resistance.

The whole cluster was cylindrically approximated and therefore also the spherical soma compartment. It also ensheathes the whole soma region, i.e., from pre- to post-somatic compartments, and therefore surrounds the whole unmyelinated region. Not only different positions of the cluster should be therefore tested to obtain more results and to compare these investigations, but also variations of electrical and geometrical parameters.

The neurons in the same cluster have the same geometrical parameters and especially show identical spatial arrangement. Of course the main interests for further investigations should be to examine neurons with different size and shape in one cluster and also the spatial arrangement needs to be investigated in further work since the corresponding compartments of neurons sharing a cluster definitely do not lie on top of each other, e.g., the perikarya are displaced to save space.

Furthermore the appearance of the membrane potential of the cluster V^{Cl} needs to be examined in more detail. Perhaps comprehensive comparison with results of the extracellular potential obtained by other authors (e.g., [Gold et al. 2006](#)) could give rise to further adjustments of parameters which might be changed in the mathematical model.

It should be pointed out that generally no spontaneous activity, i.e., no noise term was used in the models of this thesis as mentioned above. This fact may be very important since neurons in a cluster, which appear mostly at the apical region may be highly spontaneous and show a different excitation behavior. Further experiments will clarify this question.

Additionally these first results obtained in this thesis for the human neuron cluster should be compared to examinations of mammals since they do not have this certain feature.

Also a comparison with degenerated nerve fibers ([Briaire and Frijns 2006](#)) could be of special interest since the cluster is believed to play an important role in the slow retrograde degeneration in men as mentioned before.

To sum up these conclusions it should be indicated that these results obtained by this first approach only provide a basis for further investigations which play an important role for understanding the human ability of sound perception and thus also for designing cochlear implants since the special human morphology remains unique.

Appendix A

ACSL Code

This appendix contains two example codes implemented in ACSL which have been used to perform the simulations in this thesis. The first one concerns a single neuron without a surrounding cluster and the second one is presented as an example for the simulation of the multiple neuron cluster. Note that the Runtime commands, which can be implemented in a separate .cmd file and are also needed for the experimental investigation of the mathematical model, are not provided in this thesis.

A.1 Soma Code

The following code, i.e., the ACSL program file, was used to calculate the influence of the variation of the sensitive parameters at the soma region. This special code concerns the alteration of the number of myelin layers (Section 4.2.2).

Program soma

INITIAL

!geometrical parameters

```
ARRAY li(010),a(090),d(090),dx(090),typ(090),nm(090)
INTEGER i,j,jj,j_soma,dim1,dim11,dim,dim2,dimm, &
        nintern1,nintern2,ninternp,ninternc, &
        nodetyp1,nodetyp2,nodetyp0,nodetypc,nodetypp,somatyp,nm_soma
CONSTANT dim1=6,dim2=5,nintern1=1,nintern2=1,ninternp=3,ninternc=1
dim=1+dim1*(nintern1+1)+dim2*(nintern2+1)+ninternp+ninternc;dimm=dim-1
CONSTANT d0=0.0001,d1=0.0001,dsoma=0.0030,d2=0.0002
CONSTANT li=0.021,0.039,0.044,0.035,0.043,0.036,.05,.05,.05,.05,li_ax=.05
CONSTANT l0=.001,lnode1=.00025,lnode2=.00025,lsoma_p=.01,lsoma_c=.0005
CONSTANT nm1=40,nm2=80,nodetyp1=3,nodetyp2=3,nodetyp0=3,&
        mtyp=1,somatyp=2,nodetypp=3,nodetypc=3
```

A.1 Soma Code

```
!-----
CONSTANT nm_somamn=1,nm_somamx=5,nm_somadl=1
nm_soma=nm_somamn
loop: CONTINUE
CALL INITD
!-----

!electrical parameters

CONSTANT i0=0.0005,I1=0,GLINTER=1
CONSTANT VMAX=200,VMIN=-200
CONSTANT GNA=120.,GK=36.,GL=.3,V01=0, &
      VNA=115.,VK=-12.,VL=10.6,VLOW=10.6
CONSTANT M01=.0529,N01=.317,H01=.596
CONSTANT ii_LOW=1,gl_LOW=.3,K_LOW=12,ii_HI=10,gl_HI=.3,K_HI=12
CONSTANT C0=1,C1=1,C_node=1,C_soma=1,C2=1
ARRAY M0(090),H0(090),N0(090),V0(090),C(090),R(090)
ARRAY V(090),M(090),H(090),N(090),&
      VD(090),MD(090),HD(090),ND(090),II(090),VXX(090)
CONSTANT T1=.0,T2=1.,T3=.1,TEND=0.79,TX=100
rsoma=dsoma/2.;PI=3.141592;PF2=2.*PI/TE2
CONSTANT RHOI=0.05, RHOE=.3

!Calculation of the geometrical parameters

DO MINI1 j=1,090
  d(j)=d1;dx(j)=lnode1;typ(j)=1;nm(j)=1;f(j)=0
  VD(j)=0;MD(j)=0;ND(j)=0;HD(j)=0
  V0(j)=V01;M0(j)=M01;N0(j)=N01;H0(j)=H01
MINI1..CONTINUE

j=1;d(j)=d0;dx(j)=l0;typ(j)=nodetyp0; C(j)=c0

DO MINI4 i=1,dim1
  length=li_ax/nintern1; if(i.le.010) length=li(i)/nintern1
  DO MINI3 jj=1,nintern1
    j=j+1;dx(j)=length;typ(j)=mtyp;nm(j)=nm1;c(j)=c1/nm1
  MINI3..CONTINUE
  j=j+1;dx(j)=lnode1;typ(j)=nodetyp1;c(j)=c_node
MINI4..CONTINUE

DO MINI3a jj=1,ninternp
```

A.1 Soma Code

```
    typ(j)=nodetyp;nm(j)=1;c(j)=c1
    dx(j)=lsoma_p/float(ninternp);j=j+1
MINI3a..CONTINUE

j_soma=j;typ(j)=somatyp;dx(j)=dsoma;nm(j)=nm_soma

DO MINI3b jj=1,ninternc
    j=j+1;dx(j)=lsoma_c/float(ninternc)
    typ(j)=nodetypc;nm(j)=1;c(j)=c1;d(j)=d2
MINI3b..CONTINUE

dim11=dim1+1

DO MINI6 i=dim11,dim11+dim2
    length=li_ax/nintern2; if(i.le.010) length=li(i)/nintern2
    DO MINI5 jj=1,nintern2
        j=j+1;d(j)=d2;dx(j)=length;typ(j)=1;nm(j)=nm2;c(j)=c1/nm2
    MINI5..CONTINUE
    j=j+1;d(j)=d2;dx(j)=lnode2;typ(j)=nodetyp2;c(j)=c_node
MINI6..CONTINUE

DO MINI7 j=1,dim
    A(j)=PI*d(j)*dx(j)
    C(j)=C(j)*A(j)
    R(j)=2.*RHOI*dx(j)/(d(j)*d(j)*PI)
MINI7..CONTINUE

dmittel=(d1+d2)/2.;zsoma=sqrt(rsoma*rsoma-(dmittel**2)/4.)
A(j_soma)=PI*(DSOMA*DSOMA-DSOMA*(RSOMA-ZSOMA)*2.);
C(j_soma)=C_soma*A(j_soma)/nm_soma
R(j_soma)=(RHOI/(DSOMA*PI))*LOG((RSOMA+ZSOMA)/(RSOMA-ZSOMA))

END    !of inital

DYNAMIC

    CINTERVAL CINT=.0025
    NSTEPS NSTP=10

DERIVATIVE

PULS=PULSE(T1,T2,T3);S0=I0*PULS;S1=I1*PULS
```

A.1 Soma Code

```
V=INTVC(VD,V0);M=INTVC(MD,MO);H=INTVC(HD,HO);N=INTVC(ND,NO)
```

```
PROCEDURAL
```

```
DO MARK2 j=1,dim
```

```
IF (V(j).GT.VMAX) V(j)=VMAX;IF (V(j).LT.VMIN) V(j)=VMIN
```

```
IF (M(j).GT.1.) M(j)=1.; IF (M(j).LT.0.) M(j)=0.
```

```
IF (H(j).GT.1.) H(j)=1.; IF (H(j).LT.0.) H(j)=0.
```

```
IF(typ(j).EQ.1) II(j)=GLINTER*V(j)*A(j)/nm(j)
```

```
IF(typ(j).EQ.2) THEN
```

```
INA=GNA*M(j)*M(j)*M(j)*H(j)*(V(j)-VNA)
```

```
IK=GK*(N(j)**4.)*(V(j)-VK)
```

```
IL=GL_LOW*(V(j)-VLow)
```

```
II(j)=(INA+IK+IL)*II_LOW*A(j)+Inoise(j)
```

```
ZM=.1*(25.-V(j)); AM=ZM/(EXP(ZM)-1.); BM=4.*EXP(-V(j)/18.)
```

```
ZN=.1*(10.-V(j)); AN=.1*ZN/(EXP(ZN)-1.); BN=.125*EXP(-V(j)/80.)
```

```
AH=.07*EXP(-V(j)/20.); BH=1./(EXP(.1*(29.99-V(j))))+1.)
```

```
MD(j)=K_LOW*(AM-M(j))*(AM+BM)
```

```
ND(j)=K_LOW*(AN-N(j))*(AN+BN)
```

```
HD(j)=K_LOW*(AH-H(j))*(AH+BH)
```

```
ENDIF
```

```
IF(typ(j).EQ.3) THEN
```

```
INA=GNA*M(j)*M(j)*M(j)*H(j)*(V(j)-VNA)
```

```
IK=GK*(N(j)**4.)*(V(j)-VK)
```

```
IL=GL_HI*(V(j)-VL)
```

```
II(j)=(INA+IK+IL)*II_HI*A(j)+Inoise(j)
```

```
ZM=.1*(25.-V(j)); AM=ZM/(EXP(ZM)-1.); BM=4.*EXP(-V(j)/18.)
```

```
ZN=.1*(10.-V(j)); AN=.1*ZN/(EXP(ZN)-1.); BN=.125*EXP(-V(j)/80.)
```

```
AH=.07*EXP(-V(j)/20.); BH=1./(EXP(.1*(29.99-V(j))))+1.)
```

```
MD(j)=K_HI*(AM-M(j))*(AM+BM)
```

```
ND(j)=K_HI*(AN-N(j))*(AN+BN)
```

```
HD(j)=K_HI*(AH-H(j))*(AH+BH)
```

```
ENDIF
```

```
IF(typ(j).EQ.4) THEN
```

```
INA=GNAs*M(j)*M(j)*H(j)*(V(j)-VNAs); IL=GLs*(V(j)-VLs)
```

```
II(j)=(INA+IL)*A(j)+Inoise(j)
```

```
AM=(126.+363*(V(j)-80.))/(1.+EXP((-V(j)+31.)/53.))
```

```
BM=AM/EXP((V(j)-23.8)/4.17)
```

```

    BH=15.6/(1.+EXP((-V(j)+24.)/10.)); AH=BH/EXP((V(j)-5.5)/5.)
    MD(j)=AM-M(j)*(AM+BM)
    HD(j)=AH-H(j)*(AH+BH)
    ND(j)=0.
ENDIF

    IF(j.eq.1) II(j)=II(j)-S0
    IF(j.eq.j_soma) II(j)=II(j)-S1
MARK2..CONTINUE

VXX(1)=(V(2)-V(1))/(R(2)+R(1))

DO MARK5 j=2,dim
    VXX(j)=(V(j-1)-V(j))/(R(j-1)+R(j))+V(j+1)-V(j))/(R(j+1)+R(j))
MARK5..CONTINUE

VXX(dim)=(V(dim)-V(dim))/(R(dim)+R(dim))

END !of procedural

END !of derivative

TERMT(T.GT.TEND)

END !of dynamic

TERMINAL

CALL LOGD(.TRUE.)
nm_soma = nm_soma + nm_somadl
IF(nm_soma .LE. nm_somamx) GO TO loop

END !of terminal

END !of program

```

A.2 Cluster Code

The program files for the multiple neuron cluster resemble each other and thus the next code is printed as an example which was used to simulate the excitation of neurons in a three neuron cluster (Section 4.4.2).

A.2 Cluster Code

Program cluster2

INITIAL

!geometrical parameters

!Neurons_____

```
ARRAY A(030),D(030),DX(030),typ(030),nm(030),li(10)
INTEGER i,j,jj,j_soma,kk,&
    dim1,dim11,dim,dim2,dimm, &
    nintern1,nintern2,ninternp,ninternc, &
    nodetyp1,nodetyp2,nodetyp0,nodetypc,nodetyp
CONSTANT dim1=6,dim2=5,nintern1=1,nintern2=1,ninternp=3,ninternc=1
dim=1+dim1*(nintern1+1)+dim2*(nintern2+1)+ninternp+ninternc;dimm=dim-1
CONSTANT li=0.021,0.039,0.044,0.035,0.043,0.03,.05,.05,.05,.05,li_ax=.05
CONSTANT l0=.001,lnode1=.00025,lnode2=.00025,lsoma_p=.01,lsoma_c=.0005
CONSTANT dsoma=0.0030,d0=0.0001,d1=0.0001,d2=0.0002
rsoma=dsoma/2.
PI=3.141592
CONSTANT somatyp=2,nodetyp1=3,nodetyp2=3,nodetyp0=3,&
    mtyp=1,nodetyp=3,nodetypc=3
CONSTANT nmsoma=3,nm1=40,nm2=80
```

!Cluster_____

```
ARRAY A_C(05),D_C(05),DX_C(05),nm_C(05)
INTEGER j_soma_cl,dim_cl,dimm_cl
CONSTANT dim1_cl=3,dim2_cl=1,nmc=1
dim_cl=dim1_cl+dim2_cl+1;dimm_cl=dim_cl-1
INTEGER k1,k2,k3,k4,j_soma_pr,j_soma_po
CONSTANT d1_c=0.00505,dsoma_c=0.00795,d2_c=0.00515
```

!electrical parameters

!Neuronen_____

```
CONSTANT VMAX=200;VMIN=-200
CONSTANT i0=0,i1a=0.0005,i1b=0.0005,i1c=0.0005
CONSTANT GNA=120.,GK=36.,GL=.3,Gmembran=1, &
    VNA=115.,VK=-12.,VL=10.6,VLOW=10.6
CONSTANT M01=.0529,N01=.317,H01=.596,V01=0
CONSTANT ii_LOW=1,ii_HI=10,g1_LOW=0.3,g1_HI=.3,K_LOW=12,K_HI=12
CONSTANT C0=1,C1=1,C_node=1,C_soma=1,C2=1
ARRAY C(030),R(030),II(030),VXX(030),VYY(030)
```

A.2 Cluster Code

```
ARRAY MO(3,030),HO(3,030),NO(3,030),VO(3,030), &
      VD(3,030),MD(3,030),HD(3,030),ND(3,030), &
      V(3,030),M(3,030),H(3,030),N(3,030)
CONSTANT T1a=.0,T2a=2.,T3a=.1,T1b=.0,T2b=2.,T3b=.1,T1c=.0,T2c=2.,T3c=.1
CONSTANT RHOI=0.05, RHOE=.3

!Cluster-----
CONSTANT Cc=1,Gmembran_c=1
ARRAY C_c(05),R_C(05),&
      II_C(05),VXX_C(05),VYY_C(05),&
      V_C(05),VO_C(05),VD_C(05)

! Calculation of the geometrical parameters of the neurons

DO MINI1 j=1,030
  D(j)=d1;DX(j)=lnode1;typ(j)=1;nm(j)=1
  DO MINI1a kk=1,3
    VD(kk,j)=0;MD(kk,j)=0;ND(kk,j)=0;HD(kk,j)=0
    VO(kk,j)=V01;MO(kk,j)=M01;NO(kk,j)=N01;HO(kk,j)=H01
  MINI1a..CONTINUE
MINI1..CONTINUE

j=1;D(j)=d0;DX(j)=l0;typ(j)=nodetyp0;C(j)=C0

DO MINI2 i=1,dim1
  length=li_ax/nintern1
  if(i.le.010) length=li(i)/nintern1
  DO MINI2a jj=1,nintern1
    j=j+1
    DX(j)=length;typ(j)=mtyp;nm(j)=nm1
    C(j)=C1/nm1
  MINI2a..CONTINUE
  j=j+1
  DX(j)=lnode1;typ(j)=nodetyp1
  C(j)=C_node
MINI2..CONTINUE

DO MINI3a jj=1,ninternp
  j=j+1
  DX(j)=lsoma_p/float(ninternp)
  typ(j)=nodetyp;nm(j)=1;C(j)=C1
MINI3a..CONTINUE
```

A.2 Cluster Code

```
j_soma=j;
D(j)=dsoma;DX(j)=dsoma;typ(j)=somatyp;nm(j)=nmsoma

DO MINI3b jj=1,ninternc
  j=j+1
  D(j)=d2;DX(j)=lsoma_c/float(ninternc)
  typ(j)=nodetypc;nm(j)=1;C(j)=C2
MINI3b..CONTINUE

dim11=dim1+1

DO MINI4 i=dim11,dim11+dim2
  length=li_ax/nintern2
  if(i.le.010) length=li(i)/nintern2
  DO MINI4a jj=1,nintern2
    j=j+1
    D(j)=d2;DX(j)=length;typ(j)=1;nm(j)=nm2
    C(j)=C2/nm2
  MINI4a..CONTINUE
  j=j+1
  D(j)=d2;DX(j)=lnode2;typ(j)=nodetyp2
  C(j)=C_node
MINI4..CONTINUE

DO MINI5 j=1,dim
  A(j)=PI*D(j)*DX(j)
  C(j)=C(j)*A(j)
  R(j)=2.*RHOI*DX(j)/(D(j)*D(j)*PI)
MINI5..CONTINUE

dmittel=(d1+d2)/2.;zsoma=sqrt(rsoma*rsoma-(dmittel**2)/4.)
A(j_soma)=PI*(DSOMA*DSOMA-DSOMA*(RSOMA-ZSOMA)*2.);
C(j_soma)=C_soma*A(j_soma)/nmsoma
R(j_soma)=(RHOI/(DSOMA*PI))*LOG((RSOMA+ZSOMA)/(RSOMA-ZSOMA))

! Calculation of the geometrical parameters of the cluster

DO MINI6 j=1,05
  VO_C(j)=0;VD_C(j)=0
MINI6..CONTINUE
```

A.2 Cluster Code

```
j=j_soma-dim1_cl
j_soma_pr=j;

j=j_soma+dim2_cl
j_soma_po=j;

k1=j_soma_pr
DO MINI7 j=1,dim1_cl
  D_C(j)=d1_c;DX_C(j)=DX(k1);nm_C(j)=nmc;C_C(j)=CC
  k1=k1+1
MINI7..CONTINUE

j=dim1_cl+1
j_soma_cl=j
D_C(j)=dsoma_c;DX_C(j)=dsoma;nm_C(j)=nmc;C_C(j)=CC

k2=j_soma+1
DO MINI8 j=dim1_cl+2,dim_cl
  D_C(j)=d2_c;DX_C(j)=DX(k2);nm_C(j)=nmc;C_C(j)=CC
  k2=k2+1
MINI8..CONTINUE

DO MINI9 j=1,dim_cl
  A_C(j)=PI*D_c(j)*dx_c(j)
  C_C(j)=C_C(j)*A_C(j)
  R_C(j)=2.*RHOI*DX_C(j)/(D_C(j)*D_C(j)*PI)
MINI9..CONTINUE

END  !of initial

DYNAMIC

      NSTEPS    NSTP = 300
      CINTERVAL CINT = 0.01

DERIVATIVE

PULSa=PULSE(T1a,T2a,T3a)
PULSb=PULSE(T1b,T2b,T3b)
PULSc=PULSE(T1c,T2c,T3c)

V=INTVC(VD,V0);M=INTVC(MD,MO);H=INTVC(HD,HO);N=INTVC(ND,NO)
```

A.2 Cluster Code

```
V_C=INTVC(VD_C,V0_C)
```

```
PROCEDURAL
```

```
DO MARK20 kk=1,3
```

```
IF (kk.EQ.1) S1=I1a*PULSa
```

```
IF (kk.EQ.2) S1=I1b*PULSb
```

```
IF (kk.EQ.3) S1=I1c*PULSc
```

```
!-----  
DO MARK2 j=1,dim
```

```
  IF (V(kk,j).GT.VMAX) V(kk,j)=VMAX; IF (V(kk,j).LT.VMIN) V(kk,j)=VMIN
```

```
  IF (M(kk,j).GT.1.) M(kk,j)=1.; IF (M(kk,j).LT.0.) M(kk,j)=0.
```

```
  IF (H(kk,j).GT.1.) H(kk,j)=1.; IF (H(kk,j).LT.0.) H(kk,j)=0.
```

```
IF(typ(j).EQ.1) II(j)=Gmembran*V(kk,j)*A(j)/nm(j)
```

```
IF(typ(j).EQ.2) THEN
```

```
  INA=GNA*M(kk,j)*M(kk,j)*M(kk,j)*H(kk,j)*(V(kk,j)-VNA)
```

```
  IK=GK*(N(kk,j)**4.)*(V(kk,j)-VK)
```

```
  IL=GL_LOW*(V(kk,j)-VL)
```

```
  II(j)=(INA+IK+IL)*II_LOW*A(j)
```

```
  ZM=.1*(25.-V(kk,j)); AM=ZM/(EXP(ZM)-1.); BM=4.*EXP(-V(kk,j)/18.)
```

```
  ZN=.1*(10.-V(kk,j)); AN=.1*ZN/(EXP(ZN)-1.); BN=.125*EXP(-V(kk,j)/80.)
```

```
  AH=.07*EXP(-V(kk,j)/20.); BH=1./(EXP(.1*(29.99-V(kk,j)))+1.)
```

```
  MD(kk,j)=K_LOW*(AM-M(kk,j))*(AM+BM)
```

```
  ND(kk,j)=K_LOW*(AN-N(kk,j))*(AN+BN)
```

```
  HD(kk,j)=K_LOW*(AH-H(kk,j))*(AH+BH)
```

```
ENDIF
```

```
IF(typ(j).EQ.3) THEN
```

```
  INA=GNA*M(kk,j)*M(kk,j)*M(kk,j)*H(kk,j)*(V(kk,j)-VNA)
```

```
  IK=GK*(N(kk,j)**4.)*(V(kk,j)-VK)
```

```
  IL=GL_HI*(V(kk,j)-VL)
```

```
  II(j)=(INA+IK+IL)*II_HI*A(j)
```

```
  ZM=.1*(25.-V(kk,j)); AM=ZM/(EXP(ZM)-1.); BM=4.*EXP(-V(kk,j)/18.)
```

```
  ZN=.1*(10.-V(kk,j)); AN=.1*ZN/(EXP(ZN)-1.); BN=.125*EXP(-V(kk,j)/80.)
```

```
  AH=.07*EXP(-V(kk,j)/20.); BH=1./(EXP(.1*(29.99-V(kk,j)))+1.)
```

```
  MD(kk,j)=K_HI*(AM-M(kk,j))*(AM+BM)
```

```
  ND(kk,j)=K_HI*(AN-N(kk,j))*(AN+BN)
```

```
  HD(kk,j)=K_HI*(AH-H(kk,j))*(AH+BH)
```

A.2 Cluster Code

```
ENDIF

IF(j.eq.1) II(j)=II(j)-S1;

MARK2..CONTINUE

DO MARK3 j=1,dim_cl
  II_C(j)=Gmembran_C*V_C(j)*A_C(j)/nm_C(j)
MARK3..CONTINUE
!-----
!-----
VXX(1)=(V(kk,2)-V(kk,1))/(R(2)+R(1))

DO MARK4 j=2,dimm
  VXX(j)=(V(kk,j-1)-V(kk,j))/(R(j-1)+R(j))+V(kk,j+1)-V(kk,j))/(R(j+1)+R(j))
MARK4..CONTINUE

VXX(dim)=(V(kk,dimm)-V(kk,dim))/(R(dimm)+R(dim))

VXX_C(1)=(V_C(2)-V_C(1))/(R_C(2)+R_C(1))

DO MARK5 j=2,dimm_cl
  VXX_C(j)=(V_C(j-1)-V_C(j))/(R_C(j-1)+R_C(j))+V_C(j+1)-V_C(j))/(R_C(j+1)+R_C(j))
MARK5..CONTINUE

VXX_C(dim_cl)=(V_C(dimm_cl)-V_C(dim_cl))/(R_C(dimm_cl)+R_C(dim_cl))
!-----
!-----
DO MARK6 j=1,j_soma_pr-1
  VYY(j)=0
MARK6..CONTINUE

VYY(j_soma_pr)=(V_C(2)-V_C(1))/(R(j_soma_pr+1)+R(j_soma_pr))

k3=2
DO MARK7 j=j_soma_pr+1,j_soma_po-1 !=j_soma
  VYY(j)=(V_C(k3-1)-V_C(k3))/(R(j-1)+R(j))+V_C(k3+1)-V_C(k3))/(R(j+1)+R(j))
  k3=k3+1
MARK7..CONTINUE

VYY(j_soma_po)=(V_C(dimm_cl)-V_C(dim_cl))/(R(j_soma_po-1)+R(j_soma_po))
```

A.2 Cluster Code

```
DO MARK8 j=j_soma_po+1,dim
  VYY(j)=0
MARK8..CONTINUE

k4=j_soma_pr
DO MARK9 j=1,dim_cl
  VYY_C(j)=3.*II(k4)+VD(1,k4)*C(k4)+VD(2,k4)*C(k4)+VD(3,k4)*C(k4)
  k4=k4+1
MARK9..CONTINUE
!-----
!-----

DO MARK10 j=1,dim
  VD(kk,j)=(VXX(j)+VYY(j)-II(j))/C(j)
MARK10..CONTINUE

DO MARK11 j=1,dim_cl
  VD_C(j)=(VXX_C(j)-VYY_C(j)-II_C(j))/C_C(j)
MARK11..CONTINUE

MARK20..CONTINUE

END  ! of procedural
END  ! of derivative

  CONSTANT TEND=1.9
  TERMT(T.GT.TEND)

END  ! of dynamic

END  ! of program
```

Bibliography

- J.J. Briare and J.H.M. Frijns. The consequences of neural degeneration regarding optimal cochlear implant position in scala tympani: A model approach. *Hearing Research*, 214:17–27, 2006. 5
- Encyclopedia Britannica. External ear. <http://www.britannica.com/EBchecked/topic/198951/external-ear>, August 2008. 3.1
- J.F. Brugge, D.J. Anderson, J.E. Hind, and J.E. Rose. Time structure of discharges in single auditory nerve fibers of the squirrel monkey in response to complex periodic sounds. *Journal of Neurophysiology*, 32(3):386–401, 1969. 1
- L.A. Cartee. Spiral ganglion cell site of excitation ii: Numerical model analysis. *Hearing Research*, 215:22–30, 2006. 5
- S.Y. Chiu, J.M. Ritchie, R.B. Rogart, and D. Stagg. A quantitative description of membrane currents in rabbit myelinated nerve. *The Journal of Physiology*, 292:149–166, 1979. 2.4.2
- L.T. Cohen, E. Saunders, and L.M. Richardson. Spatial spread of neural excitation: comparison of compound action potential and forward-masking data in cochlear implant recipients. *International Journal of Audiology*, 43:346–355, 2004. 1
- K.S. Cole. Dynamic electrical characteristics of squid axon membrane. *Archives des sciences physiologiques*, 3:253–280, 1949. 2.4.2
- P. Dallos, X. Wu, M.A. Cheatham, J. Gao, J. Zheng, C.T. Anderson, S. Jia, X. Wang, W.H.Y. Cheng, S. Sengupta, He D.Z., and J. Zuo. Prestin-based outer hair cell motility is necessary for mammalian cochlear amplification. *Neuron*, 58:333–9, 2008. 3.1.3
- N. Dillier, W.K. Lai, B. Almqvist, C. Frohne, J. Müller-Deile, M. Stecker, and E. von Wallenberg. Measurement of the electrically evoked compound action potential via a neural response telemetry system. *The Annals of Otolaryngology, Rhinology and Laryngology*, 111:407–414, 2002. 1

BIBLIOGRAPHY

- E. Felder, G. Kanonier, A. Scholtz, H. Rask-Andersen, and A. Schrott-Fischer. Quantitative evaluation of cochlear neurons and computer-aided three-dimensional reconstruction of spiral ganglion cells in humans with a peripheral loss of nerve fibres. *Hearing Research*, 105:183–190, 1997. 3.2.2
- J.J. FitzGerald, S.P. Lacour, S.B. McMahon, and J.W. Fawcett. Microchannels as axonal amplifiers. *IEEE Transactions on Biomedical Engineering*, 55(3):1136–1146, March 2008. 4.3.2, 5
- B. Frankenhaeuser and A. F. Huxley. The action potential in the myelinated nerve fibre of xenopus laevis as computed on the basis of voltage clamp data. *The Journal of Physiology*, 171:302–315, 1964. 2.4.2
- Craig Freudenrich, Ph.D. How your brain works. <http://health.howstuffworks.com/brain.htm>, June 2001. HowStuffWorks.com. 2.4
- S. Frings. Mechanorezeption. <http://www.sinnesphysiologie.de/hvsinne/mechano/>, Mai 2003. 3.3
- R. Glueckert, K. Pfaller, A. Kinnefors, H. Rask-Anderson, and A. Schrott-Fischer. Ultrastructure of the normal human organ of corti. new anatomical findings in surgical specimens. *Acta oto-laryngologica*, 125:534–539, 2005a. 3.1.2, 3.1.3
- R. Glueckert, K. Pfaller, A. Kinnefors, H. Rask-Anderson, and A. Schrott-Fischer. The human spiral ganglion: New insights into ultrastructure, survival rate and implications for cochlear implants. *Audio Neurothology*, 10:258–273, 2005b. 3.6, 3.2.1, 3.2.2, 3.7
- R. Glueckert, K. Pfaller, A. Kinnefors, H. Rask-Anderson, and A. Schrott-Fischer. High resolution scanning electron microscopy of the human organ of corti. a study using freshly fixed surgical specimens. *Hearing Research*, 199:40–56, 2005c. 3.2, 3.1.2, 3.1.3
- C. Gold, D.A. Henze, C. Koch, and G. Buzsaki. On the origin of the extracellular action potential waveform: A modeling study. *Journal of Neurophysiology*, 95:3113–3128, 2006. 4.3.2, 5
- M. Hill. Unsw cell biology. <http://cellbiology.med.unsw.edu.au/cellbiology.htm>, April 2008. 2.5
- A.L. Hodgkin and A.F. Huxley. A quantitative description of membrane current and its application to conduction and excitation in nerve. *The Journal of Physiology*, 117:500–544, 1952. 1, 2.4.2
- W.A. Hossain, S.D. Antic, Y. Yang, M.N. Rasband, and D.K. Morest. Where is the spike generator of the cochlear nerve? voltage-gated sodium channels in the mouse cochlea. *The Journal of Neuroscience*, 25(29):6857–6868, July 2005. 3.2.1

BIBLIOGRAPHY

- J. Hummel and E. Taylor. Neural networks lab materials. <http://www.gregalo.com/neuralnets.html>, April 2007. 2.6
- E. Javel. Shapes of cat auditory nerve fiber tuning curves. *Hearing Research*, 81: 167–88, 1994. 1
- R. Jönsson, T. Hanekom, and JJ Hanekom. Initial results from a model of ephaptic excitation in the electrically excited peripheral auditory nervous system. *Hearing Research*, 237:49–56, 2008. 4.3.1
- N.Y.S. Kiang. Discharge pattern of single fibres in the cats auditory nerve. MIT press, Cambridge, MA, 1966. 1
- R.S. Kimura, C.L. Bongiorno, and N.A. Iverson. Synapses and ephapses in the spiral ganglion. *Acta oto-laryngologica. Supplementum*, 438:1–18, 1987. 1
- M.C. Liberman and M.E. Oliver. Morphometry of intracellularly labeled neurons in the auditory nerve: correlations with functional properties. *The Journal of comparative neurology*, 223:163–176, 1984. 1, 3.2.3
- O. Macherey, R.P. Carlyon, A. van Wieringen, J.M. Deeks, and J. Wouters. Higher sensitivity of human auditory nerve fibers to positive electrical currents. *Journal of the Association for Research in Otolaryngology : JARO*, 9(2):241–251, 2008. 1
- J. Malmivuo and R. Plonsey. *Bioelectromagnetism - Principles and Applications of Bioelectric and Biomagnetic Fields*. Oxford University Press, 1995. 2.1.4, 2.5, 2.6, 2.7, 2.8, 2.9
- G. Marmont. Studies on the axon membrane; a new method. *Journal of cellular physiology*, 34:351–382, 1949. 2.4.2
- C.C. McIntyre, A.C. Richardson, and W.M. Grill. Modeling the excitability of mammalian nerve fibers: Influence of the afterpotentials on the recovery cycle. *Journal of Neurophysiology*, 87:995–1006, 2002. 4.3.1, 5
- CRIC/IURC Montpellier. Promenade around the cochlea. <http://www.cochlee.org/>, March 2007. 3, 3.2, 3.4, 3.5
- J.B. Jr. Nadal. Comparative anatomy of the cochlea and auditory nerve in mammals. *Hearing Research*, 34:253–266, 1988. 3.2.2
- C.Y. Ota and R.S. Kimura. Ultrastructural study of the human spiral ganglion. *Acta oto-laryngologica*, 89:53–62, 1980. (document), 1, 3.2.2
- J. Otte, H.F. Schunknecht, and A.G. Kerr. Ganglion cell populations in normal and pathological human cochleae. implications for cochlear implantation. *The Laryngoscope*, 88:1231–1246, 1978. 3.2.1

BIBLIOGRAPHY

- L. Pamulova, B. Linder, and H. Rask-Andersen. Innervation of the apical turn of the human cochlea: a light microscopic and transmission electron microscopic investigation. *Otology & neurotology*, 27:270–5, 2006. 3.2.2
- Helmut Pfützner. *Angewandte Biophysik*. Springer-Verlag Wien New York, 2003. 2.1
- F. Rattay. The basic mechanism for the electrical stimulation of the nervous system. *Neuroscience*, 89(2):335–346, 1999. 1
- F. Rattay and P. Lutter. Speech sound representation in the auditory nerve: computer simulation studies on inner ear mechanisms. *Zeitschrift fr angewandte Mathematik und Mechanik*, 77:935–943, 1997. 1
- F. Rattay, A. Mladenka, and J. Pontes Pinto. Classifying auditory nerve patterns with neural nets: a modeling study with low level signals. *Simulation Practice and Theory*, 6:493–503, 1998. 1
- F. Rattay, P. Lutter, and H. Felix. A model of the electrically excited human cochlear neuron. i. contribution of neural substructures to the generation and propagation of spikes. *Hearing Research*, 153:43–63, 2001a. 1, 3.2.2, 3.8, 3.2.3, 4.1, 4.1, 4.2.5, 5
- F. Rattay, R. Naves Leao, and H. Felix. A model of the electrically excited human cochlear neuron. ii. influence of the three-dimensional cochlear structure on neural excitability. *Hearing Research*, 153:64–79, 2001b. 1
- F. Rattay, R.J. Greenberg, and S. Resatz. *Handbook of Neuroprosthetic Methods*, chapter Neuron modeling, pages 39–74. CRC Press LLC, 2003. 4.1, 4.1
- Universe Review. A review of the universe - structures, evolutions, observations, and theories. <http://universe-review.ca/R10-16-ANS.htm>, March 2008. 2.3, 3.2
- J.M. Ritchie. *The Axon - Structure, Function and Pathophysiology*, chapter Physiology of axons, pages 68–96. Oxford University Press, 1995. 2.1.4, 2.3.3, 4.3.1
- M.B. Sachs and P.J. Abbas. Rate versus level functions for auditory-nerve fibers in cats: tone-burst stimuli. *The Journal of the Acoustical Society of America*, 56(6): 1835–47, 1974. 1
- J.R. Schwarz and G. Eikhof. Na currents and action potentials in rat myelinated nerve fibres at 20 and 37°C. *Pflügers Archiv European Journal of Physiology*, 409: 569–577, 1987. 2.4.2
- J.R. Schwarz, G. Reid, and H. Bostock. Action potentials and membrane currents in the human node of ranvier. *Pflügers Archiv European Journal of Physiology*, 430: 283–292, 1995. 2.4.2
- LLC Seed Media Group. Scienceblogs. <http://scienceblogs.com/>, 2008. 2.1

BIBLIOGRAPHY

- S.A. Shamma. Speech processing in the auditory system. i: The representation of speech sounds in the responses of the auditory nerve. *The Journal of the Acoustical Society of America*, 78(5):1612–21, 1985. 1
- J.E. Smit, T. Hanekom, and J.J. Hanekom. Predicting human auditory action potential characteristics through adaptations of the hodgkin-huxley equations. 5
- H. Spoendlin. Degeneration behaviour of the cochlear nerve. *Archiv für klinische und experimentelle Ohren- Nasen- und Kehlkopfheilkunde*, 200:275–291, 1971. (document), 1
- H. Spoendlin and A. Schrott. Analysis of the human auditory nerve. *Hearing Research*, 43:25–38, 1989. 1, 3.1.3, 3.2.1, 3.2.3
- W.A. Svrcek-Seiler, I.C. Gebeshuber, F. Rattay, T.S. Biro, and H. Markum. Micromechanical models for brownian motion of hair cell stereocilia. *Journal of Theoretical Biology*, 193:623–630, 1998. 1
- J.D. Sweeney, J.T. Mortimer, and D. Durand. Modeling of mammalian myelinated nerve for functional neuromuscular electrostimulation. In *9th Annual Conference of the IEEE Engineering in Medicine and Biology Society, Boston*, 1987. 2.4.2
- S. Tylstedt and H. Rask-Andersen. A 3-d model of membrane specializations between human auditory spiral ganglion cells. *Journal of Neurocytology*, 30:465–473, 2001. (document), 1, 3.2.2, 3.2.2, 4.2
- S. Tylstedt, A. Kinnefors, and H. Rask-Anderson. Neural interaction in the human spiral ganglion: A tem study. *Acta oto-laryngologica*, 117:505–512, 1997. (document), 1, 3.2.2, 3.2.2, 4.4
- J. Zheng, W. Shen, D.Z.Z. He, K.B. Long, L.D. Madison, and P. Dallos. Prestin is the motor protein of cochlear outer hair cells. *Nature*, 405:149–155, 2000. 3.1.3